
# Image Reconstruction for Spinal Cord PET/MRI

**Eve Lennie**

A thesis submitted in partial fulfillment of the requirements for the degree of Doctor of Philosophy

University of Sheffield
Faculty of Health
Division of Clinical Medicine

June 2025

# Acknowledgements

I would first like to thank my supervisors Prof. Steven Sourbron, Prof. Charalampos Tsoumpas and Prof. Nigel Hoggard for their continued advice, support and encouragement over the past 4 years. It has been a privilege to work together and I have particularly appreciated the honest discussions we have been able to have. I would also like to thank Dr Thomas Jenkins for his role in leading the clinical study under which data for this project was acquired, and the valuable clinical understanding he was able to impart to me before his journey to Australia.

Secondly, I'd like to acknowledge the MRC DiMeN DTP for funding my iCASE studentship and the additional training opportunities being part of the DTP has afforded me during my studies. I would also like to thank the industrial partner, GE Healthcare, with particular acknowledgement to Matthew Spangler-Bickell and Floris Jansen for their pertinent advice and fruitful discussions spanning many time zones.

Thank you to POLARIS for being my professional home during my PhD, and to everyone in the group for providing the much-needed practical and social support throughout my time in academia.

I also want to thank the community at Structure Sport and Fitness and my trainer, Paul. I'm not sure why I chose my PhD to start getting into weightlifting, but having a welcoming gym community and the motivation to get stronger helped to keep me going when everything else felt overwhelming.

To my friends, I am eternally grateful for the time and emotional energy you have given to help me make it through to the end of my thesis. A special thanks is extended to Rory, who tried to warn me off doing a PhD, but has stood by me anyway and only once said they "told me so" when my stress has run too high. And to Katie, for the many hours playing Animal Crossing and watching Come Dine with Me to cheer me up. To my family, thank you for always being there for me. Anything I have ever wanted to do or achieve has been met with support and encouragement. I feel extremely privileged to have such a reliable and loving family behind me.

Finally, I would like to thank my husband, Mark, for picking up on so many chores whilst I have been dedicated to working on conference abstracts and thesis writing. More importantly, thank you for believing in me when I had so many doubts that I would succeed, and being ready with messages to "believe in the me that believes in you". I'm so grateful for every bit of love and care you have shown me.

# Abstract

Despite some neurological conditions also affecting the spinal cord, research using PET/MRI has focussed on brain imaging. Spinal cord MRI is common due to its high resolution and soft tissue contrast. PET, however, presents challenges due to its low resolution relative to the spinal cord's diameter. In PET/MR, spinal cord PET may also be affected by incorrect attenuation correction due to a lack of vertebral bone in MR-derived attenuation maps.

The impact of these effects and possible solutions were determined through a series of studies. A literature review established whether currently available physical phantoms were suitable for assessing the performance of PET/MR scanners. It was found that replicating tissue properties for both modalities within the same phantom was challenging, so typically one modality is prioritised.

Phantom experiments were performed using a PET performance phantom and an anatomical 'head and neck' phantom to assess the performance of the SIGNA PET/MR Scanner. It was found that for features less than 20mm, the size and tracer uptake in these regions was underestimated in PET images.

A simulation study is presented exploring the impact of MR-derived attenuation maps and PET detector resolution on measured tracer uptake in the spinal cord. This was compared to patient data. The results indicate that whilst tracer uptake is underestimated when vertebral bone is not accounted for in attenuation maps, partial volume effects due to PET detector resolution have the greatest impact.

MR-guided reconstruction of PET data was investigated as a solution to resolving partial volume effects during PET image reconstruction, using MR images simultaneously acquired with PET data. Images reconstructed with MR-guided algorithms showed an increase in measured tracer uptake in the spinal cord compared to existing reconstruction algorithms. This suggests that MR-guided reconstruction of PET data can contribute to resolving partial volume effects.

# Contents

# List of Figures

# List of Tables

# Declaration

I, the author, confirm that the Thesis is my own work. I am aware of the University's Guidance on the Use of Unfair Means. This work has not been previously been presented for an award at this, or any other, university.

## Publications Arising from this Thesis

Work from the following jointly authored paper is included within this thesis.

### Journal Articles

E. Lennie, C. Tsoumpas and S. Sourbron. Multimodal Phantoms for Clinical PET/MRI. EJNMMI Physics. 2021 Aug 26;8(1):62.

***Contribution:*** *Eve Lennie performed the investigation and composed the review article. Co-authors advised the study and edited the article.* This work is included as chapter 3.

E. Lennie, S. Sourbron, N. Hoggard, T.Jenkins and C. Tsoumpas. Quantification of [18F]FDG in Spinal Cord PET/MRI. Approved by co-authors for submission to EJNMMI Research.

***Contribution:*** *Eve Lennie performed the investigation and analysis, and composed the article. T.Jenkins and N.Hoggard were PIs for the clinical study from which data was provided. S.Sourbron and C.Tsoumpas advised the study and edited the article.* This work is included as part of chapter 5.

E. Lennie, S. Sourbron, N. Hoggard and C. Tsoumpas. MR Guided PET Reconstruction for Spinal Cord PET/MRI. Submission planned January 2025 to Medical Physics.

***Contribution:*** *Eve Lennie performed the investigation and analysis, and composed the article. N.Hoggard was PI for the clinical study from which data was provided. S.Sourbron and C.Tsoumpas advised the study and edited the article.* This work is included as chapter 6.

### Conference Abstracts

All associated conference abstracts are listed here. Eve Lennie was the presenting author in all cases.

E. Lennie, S. Sourbron, N. Hoggard and C. Tsoumpas. The effect of vertebral bone attenuation on measured spinal cord activity in PET/MRI. (2023) IEEE Nuclear Science Symposium - Medical Imaging Conference, Vancouver, Canada. Poster presentation.

E. Lennie, S. Sourbron, N. Hoggard and C. Tsoumpas. Hybrid Kernelised Expectation Maximisation for image reconstruction of the spinal cord in PET/MRI. (2024) Conference on PET, SPECT and MR, Isola d'Elba, Italy. Oral presentation.

## Funding Awards Associated with this Thesis

PET/MRI scanning of the Head and Neck phantom in Chapter 3 was funded by the Collaborative Computational Project in Synergistic Reconstruction for Biomedical Imaging (CCP Synerbi, EPSRC grant EP/T026693/1).

# Chapter 1

# Introduction

## 1.1 Context and Motivation

Medical Imaging serves as an important tool in the research, diagnosis and monitoring of diseases by providing minimally invasive mechanisms for visualising anatomical and physiopathological biomarkers.

PET/MRI is a combined imaging modality introduced to the clinical market in 2010, allowing for the simultaneous acquisition of Positron Emission Tomography (PET) and Magnetic Resonance Imaging (MRI) images using the same scanner in a single imaging session. Both modalities have been used extensively for neuroimaging in research, with the field benefiting from simultaneous acquisition and the development of specific PET tracers for neuroimaging applications. Initially challenges to overcome included compatibility of PET detectors with the large magnetic field required for MRI [18], and then find solutions in image reconstruction for attenuation correction due to having no tissue density information such as with PET/CT[19]. Brain imaging has been a large area of focus in the optimisation and development of PET/MRI and the associated image reconstruction software performance. This has led to significant improvements in the correction of PET data for attenuation in the skull [20], motion correction for bulk head motion [21], and in the localisation of radiotracer distribution in the brain with respect to MRI defined anatomy [22].

The promising results from clinical research using brain PET/MRI and preclinical studies have revealed new imaging opportunities, and spinal cord imaging offers further insights into the function of the central nervous system (CNS). Despite many diseases of the central nervous system also impacting the spinal cord and previous research into these diseases using PET and MRI as separate modalities, there has been very little focus on the development of optimised PET/MRI

acquisition and image reconstruction for spinal cord imaging.

There are still some technical barriers to accurate quantification of PET tracer uptake in the spinal cord for PET/MRI. The spinal cord is surrounded by vertebral bone, which attenuates the gamma rays detected in PET, and corrections applied in PET/CT for this aren't possible as cortical bone doesn't generate a signal for imaging with MRI. Additionally, the spinal cord's small diameter makes it susceptible to partial volume effects at the detector resolution available in clinical PET.

Accurate quantitative spinal cord PET/MRI would benefit translational neuroscience research by providing simultaneously acquired complimentary functional information. The benefit of acquiring PET and MRI simultaneously is in improved registration to identify and correlate features from both modalities, for a small diameter structure such as the spinal cord [23]. A single scan session is also more tolerable for patients with CNS disorders who may find multiple long imaging sessions difficult [24]. This could improve the understanding of disease mechanisms and assess therapeutic efficacy of treatments in clinical trials through monitoring of receptor activity and neuronal structure in the spinal cord [25]. This thesis focuses on investigating the necessary PET data corrections and the optimisation of image reconstruction to facilitate more accurate quantification of spinal cord PET in PET/MRI systems.

## 1.2 Thesis Aims

The focus of this thesis was to establish the impact of attenuation correction and detector resolution on spinal cord imaging for PET/MR. Then to determine the corrections required such that the quantification of PET uptake in the spinal cord is increased in accuracy, and its visualisation in PET images is improved. This was achieved by addressing 3 questions throughout this thesis:

**Aim 1: Do phantoms exist that are capable of replicating tissue properties and anatomical geometry of the spine and spinal cord for the performance assessment or PET/MR scanners?**

Imaging the spinal cord has not been a widespread application in PET previously, with the review by Kiamanesh et al. identifying only 6 adult studies previously reporting baseline values for [$^{18}$F]FDG uptake [26], and one study in PET/MR [5]. As such, the first aim of this thesis was to determine the current state of the field, and whether there exists physical phantoms that can the mimic tissue proprieties and anatomical proportions of the spine to allow establish baseline performance in house. The literature review presented in this thesis details

research into tissue mimicking phantoms and the use of phantoms in assessing the performance of PET/MR scanners.

**Aim 2: To what extent are attenuation correction and partial volume effect sources of error in PET images for spinal cord PET/MR?**

It was necessary to establish a baseline for the capability of the GE SIGNA PET/MR in imaging the spinal cord, as this hasn't previously been reported. The performance of a current, commercially available scanner and associated software in the GE PET Toolbox (GE Healthcare) was assessed through a series of phantom experiments and clinical acquisitions. The open source software packages STIR (Software for Tomographic Image Reconstruction) [27] and SIRF (Synergisitic Image Reconstruction Framework) [28] was also used to perform simulation studies modeling the GE SIGNA PET/MR scanner properties, allowing access to additional image reconstruction algorithms used by the PET/MR research community. This allowed for the investigation of the impact of two known sources of error in PET/MR that affect PET images of the spinal cord: attenuation correction of cortical bone in the spine [5], and partial volume effects due to the spinal cord's small diameter [26]. This is also the first investigation to quantify these effects in spinal cord PET/MR.

**Aim 3: Can MR guided PET image reconstruction reduce the impact of partial volume effects in spinal cord PET/MR?**

The third aim of this thesis was to compare MR guided reconstruction algorithms to the commercially available and widely used algorithms, and determine whether they provide any improvement in PET quantification or the visualisation of spinal cord anatomy in PET images. The spinal cord can be difficult to visualise in [$^{18}$F]FDG PET due to it's relatively low tracer uptake compared to nearby organs, as demonstrated in figure 1.1.

From the GE PET Toolbox, MR guided Q.Clear was compared to Q.Clear and TOFOSEM-PSF (Time of Flight Ordered Subset Expectation Maximisation with Point Spread Function modelling). From the open source packages, HKEM (Hybrid Kernel Expectation Maximisation) [29] was compared to OSEM (Ordered Subset Expectation Maximisation). Both MR guided algorithms utilize anatomical MR acquired simultaneously to PET data in the PET image reconstruction process, and were expected to reduce the impact of partial volume effects on the spinal cord, improve contrast of spinal cord uptake to background activity, as well as reduce noise in PET images [30]. This requires images from both modalities that are highly co-registered to avoid introducing additional errors during image reconstruction [19].

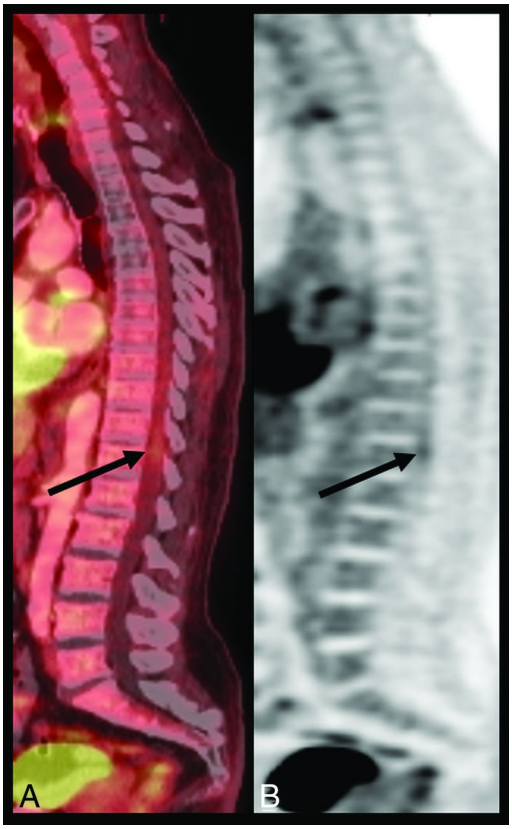


**Figure 1.1**: Image taken from [1] demonstrating the expected normal physiological uptake in the spinal cord for [$^{18}$F]FDG PET/CT. The arrow indicates a known region of increased uptake in the thoracic spinal cord.

## 1.3 Thesis Organisation

The organisation of the thesis chapters is as follows:

Chapter 2 summarises relevant information on clinical imaging of the spinal cord, and technical information on PET/MR scanners and different PET reconstruction algorithms. This acts as the background required for full understanding of the work presented in this thesis.

Chapter 3 is a literature review of physical phantoms and test objects for assessing performance in PET/MRI scanning and image reconstruction. This was published in EJNMMI physics as a review article under the title "Multimodal Phantoms for Clinical PET/MRI" [31]. This literature review explores options for physical phantoms that can be used in assessing PET/MR scanner performance for different applications and the challenges involved in creating tissue equivalent phantoms for multi-modality systems.

In chapters 4 and 5, the second aim of the thesis is addressed. First, the perfor-

mance of the GE SIGNA PET/MR scanner was assessed in imaging small diameter features on the scale of the spinal cord through a set of preliminary experiments using physical phantoms. The results presented indicate the causes of error for investigation in further experiments.

In chapter 5, a simulation study was performed using an anthropomorphic computational phantom and clinically acquired data to assess the impact of attenuation correction and partial volume effects of the quantification of activity in the spinal cord. The performance of existing algorithms available on the GE Healthcare SIGNA PET/MR scanner are also benchmarked for quantification of activity in the spinal cord. This chapter represents the first study to quantify errors in the quantification of PET data in the spinal cord through simulation.

Chapter 6 presents the results of applying state of the art MR guided PET reconstruction algorithms to spinal cord imaging. This has not been demonstrated previously, and the work in this chapter illustrates the benefits these algorithms provide to quantification of PET data in the spinal cord.

Finally, in chapter 7 the work presented in this thesis is summarised and overall conclusions drawn from it. Future work building on the results of this thesis is suggested and the thesis finishes with an outlook for spinal cord imaging in PET/MR and the role MR guided image reconstruction could play in this going forward.

# Chapter 2

# Background

## 2.1 Spinal Cord Involvement in Neurodegenerative Diseases

Neurodegenerative diseases are a wide range of disorders that affect the central nervous system through the degradation of neurons in the brain and spinal cord. This can lead to symptoms of cognitive impairment and difficulties with movement. Multiple sclerosis (MS), amyotrophic lateral sclerosis (ALS) and the other motor neurone diseases (MND) are all types of neurodegenerative disease which are caused by demyelination and degradation of neurons in the brain and spinal cord. They include symptoms such as muscles weakness, cramps, twitches, muscle atrophy and slurred speech [32]. The rapid progression of MND's also leads to patient death as breathing and swallowing become more difficult.

The spinal cord is a length of grey and white matter that runs down the spinal canal and is surrounded by cerebral spinal fluid (CSF). Within the cord, grey matter forms in the centre of the spinal cord in a "H" shaped column, shown in figure 2.1, and predominantly consists of neuron cell bodies and neuroglia. These process sensory input, motor commands for skeletal muscle and direct impulses to the appropriate tracts [33]. White matter is formed around the grey matter in columns of ascending and descending myelinated axonal tracts. The amount of white matter decreases along the length of the spinal cord, however the spinal cord diameter bulges in the lower cervical spine and in the lumbar spine just before the end of the spinal cord. These are known as the cervical and lumbar enlargements and are the nexuses for spinal roots joining the cord from the upper and lower limbs.

Each vertebra of the spine has a gap called the vertebral foramen, where the spinal canal sits. In most vertebra, this is behind the main body of the vertebra and surrounded by the articular processes laterally, and spinous process anteri-

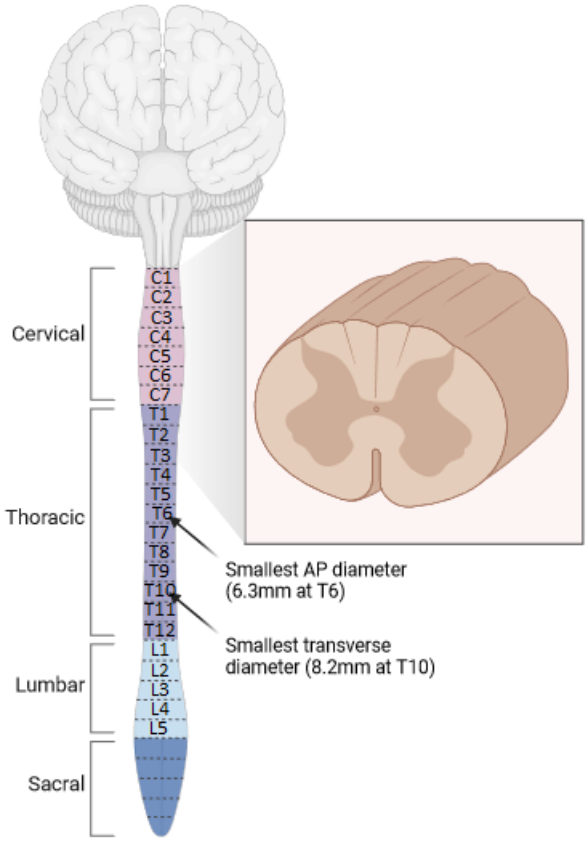


**Figure 2.1**: A representation of the spinal cord and sections as well as a depiction of the cross section of the spinal cord. The cross section depicts the grey matter "horns", showing how grey and white matter are arranged within the cord. Graphic created in BioRender.

orly. The spinal cord begins at the medulla oblongata in the brain stem and extends to the upper sections of the lumber spine with the conus medullaris, around the L2 vertebra. The transverse diameter of the spinal cord is on average largest around the C4 vertebra at $13.3 \pm 2.2$mm [34] and smallest at T10 ($8.2 \pm 2.1$mm). The anterior-posterior diameter is overall smaller and starts at $8.3 \pm 1.6$mm at C1, decreasing to $6.3 \pm 2.0$mm at T6 [34]. It has three meninges to provide stability and a protective layer: the pia mater, arachnoid mater and spinal dura mater.

When the axonal tracts in the brain and spinal cord undergo demyelination in neurodegenerative disease, there is a breakdown in nerve signalling that leads to disordered movement and affects organ function. It would be beneficial for understanding treatment mechanisms and as part of clinical trials to image this process. However, there are no reliable imaging biomarkers for ALS and the other MND's in the spinal cord [35].

## 2.2 Imaging Modalities

### 2.2.1 Magnetic Resonance Imaging

Magnetic Resonance Imaging (MRI) examination of the spine is a well established clinical pathway in many areas of medicine owing to the good contrast and visibility of the soft tissue structures in the spine such as disks, spinal cord, CSF and bone marrow. It can be used to identify inflammation, necrosis and lesions within the spinal cord, with more advanced techniques such as diffusion tensor imaging (DTI) and myelin water fraction imaging providing insights into structural and functional changes in the microstructures of the spinal cord [36].

MRI uses a strong magnetic field to align the protons with the hydrogen atoms of water molecules in the human body into the same orientation. A spatially varying magnetic field is then applied to create a different field strength at different positions in the body to adjust the proton alignment to provide spatial encoding. Radiofrequency (RF) waves are then applied to the protons to disrupt their alignment with the magnetic field. As the protons realign they emit a RF signal which is detected by a receiver coil placed externally near the area of interest on the body, with different tissues displaying different signal intensity due to their proton density and tissue structure. Broadly, this leads to images that display fluids, water-based tissues and fat-based tissues tissues with different intensities. Pulse sequences comprising of RF pulses and gradient pulses are used to acquire images and can be manipulated to change how tissues are displayed by changing the contrast mechanism.

Tissue contrast is controlled by the tissues spin-lattice relaxation time (T1) and spin-spin relaxation time (T2). The relaxation time is how long protons in the tissue take to return to an equilibrium state after being disrupted by an RF pulse. T1 is the relaxation time for protons to realign along the primary magnetic field, and T2 is the relaxation time for proton spins to de-phase after an RF pulse causes them to spin in phase [37]. In T1-weighted images, fluids have low signal intensity, water-based tissues have a mid-range signal intensity and fat tissues have the highest signal intensity. Whereas in T2-weighted images, fluids have the highest signal intensity whilst other tissues exhibit a range of intermediate signal intensities. Pulse sequences can be manipulated to keep these contrast weightings whilst suppressing fluid or fat signals. Advanced methods such as diffusion MRI exploit the dependence of relaxation times on mechanisms such as water diffusion or tissue geometry, and apply techniques to detect this from the MR signal.

Specialised techniques can be employed to visualise desired tissues. One example is the Dixon sequence for creating images of fat and water in the body [38].

To do this, a gradient echo sequence is used to acquire an "in-phase" image, where readout occurs at the moment fat and water excitations are in phase, and an "out of phase" image when the fat and water molecule excitation is exactly 180° out of phase. By adding these two images together, only the water signal remains, and by subtracting the two images only the fat signal remains [37]. This is known as a spectroscopic imaging technique.

Another example is UTE (ultrashort echo time) and ZTE (Zero Echo time) imaging, which allows cortical bone to be imaged despite its low MR signal. This became possible with the development of radial sampling, where projections are acquired at different angles through the object. By sampling in this non-cartesian way, a phase encoding gradient is no longer required [37]. This allows images to be acquired at the lowest TE possible by the system so the tissues with very short T2 can be visualised. Often for post processing, an additional image is acquired at a later TE to subtract from the UTE image, so that the short T2 features appear bright against a dark background [37].

MR acquisitions are susceptible to artefacts. As they rely on magnetic field gradients, artefacts can appear where these are disrupted by the presence of implants or non-magnetic metals due to their vastly differing properties to human tissue [37]. Metals will also respond to the field gradients and RF pulses through the creation of eddy currents and may heat up. Gibbs artifacts can also occur at tissue boundaries where there is a sudden change in relaxation properties when the MR acquisition is under-sampled and appears as a ringing artifact.

Some MR sequences can take a long time to acquire, and patients must remain still throughout the exam to avoid motion artifacts. Physiological motion cause also cause motion artifacts, particularly in the abdomen where breathing motion causes organs to shift. Blood and CSF flow can also create artifacts, as the disrupted protons have already moved on before their relaxation signal can be detected, creating an empty space where this relaxation signal is lost.

### 2.2.2 Positron Emission Tomography

Positron Emission Tomography (PET) is performed by administering patients with a molecule labelled with a radioactive $\beta^+$ (positron) emitting element, commonly called the radiopharmaceutical or radiotracer, so as to detect the gamma photons generated when the positron undergoes annihilation with an electron within the patients body. The annihilation event creates two 511keV gamma photons travelling in opposing directions and are detected within the PET scanner by a ring of scintillation detectors around the patient. A coincidence window applied to detected photons allows a line of response (LOR) to be generated between two de-

tectors, indicating that the annihilation event occurred between these two detector positions. Scanners utilising scintillation crystals with a very short decay time and high light yield, such as Lutetium Oxyorthosilicate or Lutetium-Yttrium Oxyorthosilicate based crystals, backed by silicon photomultiplier demonstrate and much shorter coincidence timing resolution (CTR) [39] compared to the previous generation of PET detectors and are able to provide time of flight (TOF) information. TOF is where the difference in arrival time between photons is measured to determine the region of the line of response that the photon annihilation event is more likely to have occurred, rather than assigning all positions along the LOR with equal probability.

A radiotracer, which is a pharmaceutical or physiological molecule labelled with a radioactive nuclide, is injected into patients prior to PET imaging. The tracer is then taken up by tissue or organs in the body and the radiation emitted by the radionuclide is detected during scanning. Fluorodeoxyglucose ([$^{18}$F]FDG), a sugar molecule labelled with a fluorine radio-isotope, is the most commonly used PET tracer. PET imaging identifies areas of increased radiotracer uptake, indicating areas of inflammation or increased metabolic activity, which in the CNS can suggest increased axonal connectivity, when [$^{18}$F]FDG is used as a tracer. More specialised tracers are able to provide information on the activity of specific neurotransmitters within the spinal cord [36, 40]. Uptake can be quantified through the calculation of values such as the Standardised Uptake Value (SUV).

There are also challenges with imaging artefacts in PET. Commonly, PET is paired with computed tomography (CT) in a combined PET/CT scanner, an x ray imaging modality to provide radiation attenuation information for tissues to attenuation correct PET data prior to image reconstruction. This is because the human body and hospital equipment attenuates the radiation emitted by the radiotracer. This reduces the activity detected, with attenuation having a greater impact on resulting images the deeper the decay event occurs within the body. Incorrect attenuation correction can lead to activity being under or over corrected, and not appearing with the correct signal intensity in the resulting PET images.

PET images can take a long time to acquire, with a whole body PET scan taking around 10 - 15 minutes. This is particularly the case for dynamic scans, where imaging begins at tracer administration to observe the uptake of tracer in the organ of interest over time periods such as 90 - 120 minutes. This can lead to motion artifacts if patients are unable to remain static for the full scan time, although a number of methods for motion correction are available to resolve this [21, 41]. PET scans may also be sped up by administering high activities, to allow for a higher photon yield in a short time frame and decreasing overlap between

bed positions - although this risks losing sensitivity at the edges of the FOV. Long axial field of view (LAFOV) scanners [42] are now available which are able to perform whole body imaging in more shorter timeframes.

Partial volume effect in PET describes two processes [43]. The first is common across many imaging modalities including CT and MRI, and is due to the finite size of the voxel grid that images are sampled over. This is where multiple tissues are present within a single voxel at tissue boundaries, and find their signal averaged over that voxel [44], as demonstrated in figure 2.2. Resolution in PET images is lower than that of CT or MRI, at around 4-6mm, which can lead to the partial volume effect at tissue boundaries. Unlike other modalities, PET also experiences a contribution to the partial volume effect from its finite detector resolution. For smaller structures less than 3 times the scanner resolution at full width half maximum (FWHM), this generally means a loss of signal to the neighbouring tissue [45]. This is due to signal "spilling" outside of the true source boundaries, reducing the signal intensity of small features, blurring the edges and reducing their quantitative value [43].

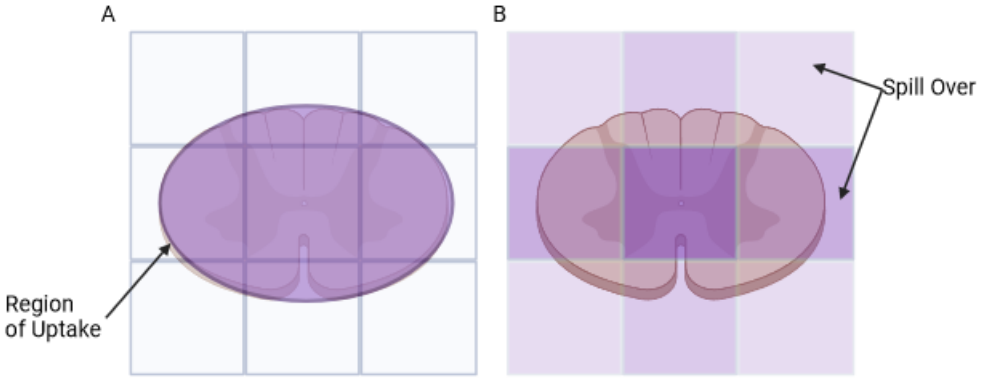


**Figure 2.2**: A representation of the spinal cord cross section imaged over a voxel gird. Part A shows the target region of uptake to be imaged, while part B shows how this may be represented in the voxel grid due to the region only partially occupying some voxels, leading to spill over of the activity into neighbouring regions. Graphic created in BioRender.

Partial volume correction (PVC) is an active area of research in PET imaging [44–46]. Many post-reconstruction PVC methods also use anatomical information such as MRI or CT. Early methods such as the Geometric Transfer Matrix (GTM) [47] , Region-based voxel-wise correction (RBV) [48] and iterative yang (IY) [46] require anatomical images to be segmented into regions to resolve partial volume effect between each region, but these assume uniform activity within regions [45] and rely on accurate segmentation and registration of the anatomical images

[49]. Later, deconvolution techniques combined with anatomical imaging such as presented in [49] were introduced that reduce blurring without requiring prior segmentation of MR regions, and are also able to apply PVC within tissue regions. However, these techniques lead to increased noise in resulting images [45] unless regularised [49], which then introduces a trade off between feature visibility and noise suppression.

Resolution recovery can be applied during image reconstruction through modelling the scanner point spread function (PSF), the degree to which signal is blurred by the detector. This is often modelled as a Gaussian function [45], although detector performance varies across the scanner field of view (FOV). PSF correction can be applied during the image reconstruction process.

### 2.2.3 PET/MRI

Combined PET/MRI scanners allow for the simultaneous acquisition of PET and MRI data. Clinical PET/MRI scanners currently on the market (GE Healthcare, Siemens Healthcare and United Imaging) are built with the PET detector ring fitted within the main body of the MRI scanner by using radio frequency shielded solid state detectors. A diagram representing the layout of hardware in clinical PET/MR systems is shown in figure 2.3.

PET/MRI was developed from a desire to combine high resolution anatomical imaging with functional imaging [18]. This modalities have been correlated previously from separate acquisitions, however different positioning and scan geometry make registration between modalities challenging, particularly when trying to few small structures.

The benefits of PET/MRI are improved image registration compared to offline registration of images acquired on the individual modalities. Additionally, active lesion identified in quantitative MRI and PET imaging provides opportunity to correlate functional information from each modality both spatially and temporally, as has been demonstrated for epileptic foci and in Alzheimer's research in the brain [50].

There are also increased opportunities available to explore in image reconstruction, largely to the benefit of PET image reconstruction. As the data can be acquired simultaneously, fast MRI sequences may be used to motion correct the longer acquired PET data [51]. Furthermore, quantification metrics in PET can be improved through the application of partial volume correction (PVC) and have already been applied to PET/MRI of the brain in multiple sclerosis (MS) patients [52]. These methods use the higher resolution anatomical T1 and T2-weighted MRI to recover PET image resolution and define tissue boundaries [44]

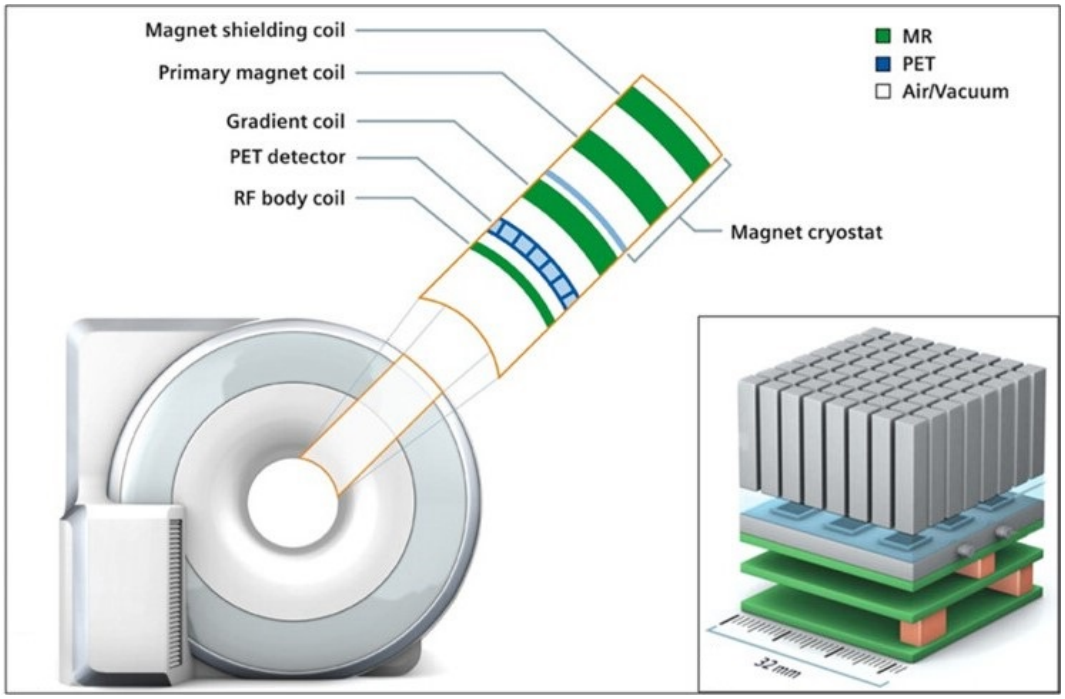


**Figure 2.3**: A diagram illustrating the arrangement of instrumentation within the main body of a clinical PET/MR scanner and a schematic of PET detectors used in the PET/MR system. Adapted from [2] with permission.

Simultaneous PET/MRI acquisition does present some challenges. Initially, difficulty in constructing a functional combined scanner with PET detectors able to withstand the high magnetic fields of MRI was a significant barrier to overcome [18]. Additionally, the detectors should not disrupt the magnetic field homogeneity for MRI [53]. Solid state detectors in PET made this possible and are stable in the presence of fluctuating magnetic and rf fields used in MRI [54].

Attenuation correction of PET data in the absence of CT still presents barriers in many imaging applications due to the effect these corrections have on quantitative PET [5]. Photons from PET tracer decay primarily undergo Compton interactions in soft tissues, which is directly related to the electron density of the material the photons are interacting with. Photon attenuation along a line of response is described by the formula

$$I = I_0 e^{\int_{LOR} -\mu(x)dx} \tag{2.1}$$

where $I_0$ and $I$ represent the tracer emitted photon fluence and the transmitted or detected photon fluence respectively. $\mu$ is the linear attenuation coefficient, which describes the probability that a photon will undergo an interaction within the tissue, and $L$ is tissue (or other material) thickness.

Attenuation is important to correct for in PET imaging as the effect is substan-

tial, leading to a heavily reduced activity concentration inside attenuating tissues in PET images. This renders quantitation impossible unless attenuation correction is applied [55]. Incorrect attenuation correction in PET will lead to lesions deep in tissue appearing to produce less signal that superficial lesions, and can lead to an overestimate in signal in low attenuation tissues such as the lungs [56].

In PET/CT, pixel values in CT images are directly related to the linear attenuation coefficient as calculated for the energy of the X-Ray photon beam used to acquire the CT data [55]. This allows for a bilinear model to convert CT numbers acquired at a specific energy (usually in the range of 100 - 140 kVp), to linear attenuation coefficients for PET photons at 511keV.

In PET/MRI, this is not the case, as MR signal is related to proton density rather than electron density. Current approaches to deriving MRI based attenuation maps use Dixon MRI sequences for the patient legs and abdomen to acquire images of the fat and water distribution of tissues, and an additional Zero Echo Time (ZTE) sequence in the head to acquire a relaxation signal from the bone of the skull [57]. Images acquired from the Dixon sequence are used to create a map of the patients body with 4 tissue classes - muscle, fat, lung and air. These are then assigned appropriate attenuation coefficients for each tissue type to generate the attenuation map used for attenuation correction. The ZTE sequence allows for the addition of a bone tissue class. This can fail to take into account varying tissue density and is prone to errors in tissues such as the lung and bone features [58].

Many highly attenuating tissues and structures, such as bone, hair, headphones and MRI coils are not traditionally visible in MRI and must still be corrected for [59]. For fixed position coils, vendors can provide an attenuation data to be incorporated into MRI derived attenuation maps, however a fixed map is unable to account for anatomical variations [60]. Another aspect to consider is the truncation of the arms and shoulders in MRI acquisitions and the need to ensure the full extent of the patient is included in the attenuation map [61]. Additionally, scatter correction is also affected by the attenuation values calculated, as typical approaches incorporate both the attenuation coefficient directly as well as the corrected emission map, which will be underestimated if applied attenuation correction is too low.

Attenuation correction in PET/MRI will benefit from the continued development of ultra-short echo time (UTE) and zero echo time (ZTE) MRI sequences, which allows for the imaging of tissues with short-T2 relaxation times such as cortical bone. ZTE has been shown to successfully image bone fractures [62] and to generate pseudo-CT's [63], an approach already used in brain PET/MRI to correct for skull attenuation [64].

## 2.3 PET Image Reconstruction Algorithms

To best understand how MR anatomical information can be incorporated into PET reconstruction algorithms, it is necessary to understand the methods and algorithms that have come before. This section explores how algorithms have developed from initial analytical reconstruction algorithms, to more recent model based methods that have become available as computational power has increased. It is these iterative model-based reconstruction algorithms that provide the mathematical foundation to enable MR anatomical information to be utilised during image reconstruction.

### 2.3.1 Analytical Reconstruction Algorithms

Detections in PET are typically stored as a sinogram. This is a data representation that categorises coincidence events by plotting each line of response as a function of its angular orientation and its displacement from the PET detector ring isocentre. The mathematical function for this process is known as the Radon transform. A diagram demonstrating this principle is shown in figure 2.4.

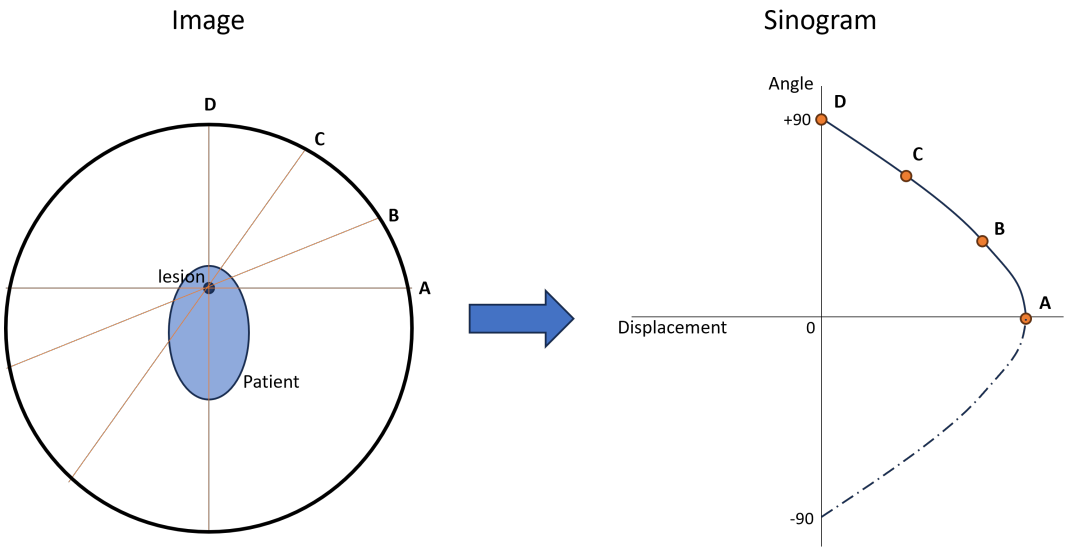


**Figure 2.4**: A 2D representation of how data points detected in a PET scanner can be depicted as a sinogram.

Image reconstruction in PET began as 2-dimensional (2D) reconstructions by a method known as filtered back projection (FBP). In tomographic imaging, this is when values measured are by the detector are projected along every line of response by inverse Radon transform to build up an image as each of these back projections intersects. This is a fast way to reconstruct images, but images need

high count rates and can be very blurred. Filtering the data prior to back projection with a high pass filter improves image quality and reduces blurring. For 3-dimension (3D) PET reconstruction, the 3D dataset is first rebinned into a set of 2D sinograms, which can then be reconstructed by FBP.

These models allow for direct reconstruction, are easy to implement and computationally inexpensive. However they assume noiseless data, requiring the need for noise control through filtering and post-processing, and don't account for many of the physical processes behind photon detection in PET such as, but not limited to, inter-crystal scatter and the stochastic nature of radioactive decay [65].

### 2.3.2 Model Based Reconstruction Algorithms

Model based methods describe the problem of PET reconstruction as a probability of finding image $\lambda$ from the measured sinogram data ($\mathbf{Y}$) using statistical models. This allows for the data acquisition process to be modelled as

$$\mathbf{Y} = \mathbf{A}\boldsymbol{\lambda} + \mathbf{S} + \mathbf{R} \tag{2.2}$$

where A is the system matrix, $\mathbf{S}$ is the scatter contribution and $\mathbf{R}$ is the randoms contribution to the measured data. The system matrix A can then be defined to model the system properties and attenuation effects for the PET data. Modelling these effects is much more computationally expensive than the previous analytical solutions but leads to improved image reconstruction [65].

The most common approach to finding the image solution is to maximise the likelihood of the image estimate using an expectation-maximisation algorithm, known as maximum likelihood expectation maximisation (MLEM). This is an iterative algorithms that produces an updated image estimate with each iteration by forward projecting the existing image estimate to compare to measured data. The ratio between these is back-projected to generate a voxel-by-voxel weighting that is then applied to the existing image to give a new image estimate. The objective function to be solved in these algorithms is described by

$$\hat{\lambda} = \arg\max_{\lambda \geq 0} \sum_{i=1}^{n_d} \{y_i log[a\lambda]_i - [a\lambda]_i\} \tag{2.3}$$

for each element i of the PET sinogram and $n_d$ is the number of projections in the dataset.

MLEM is able to fully converge to an accurate solution, however it requires a high number of iterations to do so, and the resulting images are very noisy due to the ill conditioned nature of the problem. Ordered subset expectation

maximisation (OSEM) overcomes some of these limitations by partitioning data into subsets, applying each of these subsets individually to the image update in turn. This accelerates the convergence of the algorithm, but still requires early stopping to minimise noise introduced into the final images [66], or applying filters post-reconstruction to reduce the appearance of image noise.

### 2.3.3 Bayesian Reconstruction Algorithms

An alternative to the MLEM and OSEM algorithms is to use a Bayesian framework, applying a statistical prior to combat the ill-conditioned nature of the problem. The statistical prior imposes expected properties that the resulting image should adhere to, and acts as an additional parameter to be maximised so that the objective function becomes

$$\hat{\lambda} = \arg\max_{\lambda \geq 0} \sum_{i=1}^{n_d} \{y_i log[a\lambda]_i - [a\lambda]_i - \beta R(\lambda)\} \tag{2.4}$$

where $R(\lambda)$ is the prior and $\beta$ is the weighting applied to the prior.

Typically in image reconstruction, rather than assume all voxels are independent, the Markov Random Field (MRF) is utilized for the prior. This describes the interactions between voxels within a local neighbourhood. The voxel neighbourhood can be defined by the number of nearest neighbours suitable for the application and computational power available, with larger neighbourhoods increasing the complexity of describing the potential functions and the computational cost [30]. The prior takes the form of a Gibbs energy function so that the penalty function for each pair of voxels typically takes the form of a weighted sum of differences for a quadratic prior:

$$R(\lambda) = \sum_{J} \sum_{l \in N_j} \beta_{jl} (\lambda_j - \lambda_l)^2 \tag{2.5}$$

where $\beta_{jl}$ are weighting factors determining how similar voxels $j$ and $l$ within a neighbourhood should be. This is known as the maximum a posterior (MAP) approach to PET image reconstruction [67].

The aim of these methods is to place higher likelihood on images that are locally smooth, but must be careful not to over-smooth across edges with large signal changes such as organ boundaries. Similarly, weighting of the penalty function is optimised to moderate the strength with which they are enforced on the final image [66]. A Bayesian penalised likelihood reconstruction method is implemented by GE Healthcare on the SIGNA PET/MR scanner with the Q.Clear algorithm

[68], which is used for image reconstruction throughout this thesis. Q.Clear uses a relative difference prior given as

$$R(\lambda) = \sum_{J} \sum_{l \in N_j} w_j w_l \frac{(\lambda_j - \lambda_l)^2}{(\lambda_j + \lambda_l) + \gamma|\lambda_j - \lambda_l|} \tag{2.6}$$

to suppress noise whilst preserving edges at tissue boundaries [69].

### 2.3.4 MR Guided PET Image Reconstruction

The principle underlying the desire for anatomically guided PET image reconstruction is that whilst both anatomical and functional imaging are measuring different biological processes, the anatomy and physiological process share mutual spatial information [30]. For example, in most cases it is reasonable to assume that when measuring the physiology of an organ, those processes should be measured within that organ's anatomical boundaries. However, whilst we do not know whether uptake within the organ is homogeneous, we would not expect continuous tracer uptake across organ boundaries. It is this boundary information that anatomically guided reconstruction aims to introduce to PET images. In this way, partial volume correction is integrated into the image reconstruction process.

Both of the model based approaches mentioned in the previous sections lay the foundations for inclusion of anatomical information into the PET image reconstruction process. However, it is perhaps more intuitive to see how this is performed in the case of Bayesian algorithms as follows.

#### Anatomical *A Priori* Reconstruction

Once the mathematical framework was found to include *a priori* information as an additional penalised constraint in PET image reconstruction, the next stage of development was to adapt the method so that anatomical images from other modalities can form these constraints. As discussed in section 2.3.3, implementations of the MRF in MAP reconstruction is at risk of over-smoothing across organ boundaries in an effort to modulate noise in the final PET image. Introducing a way for the prior to enforce edge preservation could present a solution to this pitfall.

This is incorporated into the MRF by using a function for $\beta_{ij}$ in equation 2.5 dependent on the edge strength of the anatomical image, rather than a constant penalty, to become

$$\beta_{ij} = F(g_I, g_j) \tag{2.7}$$

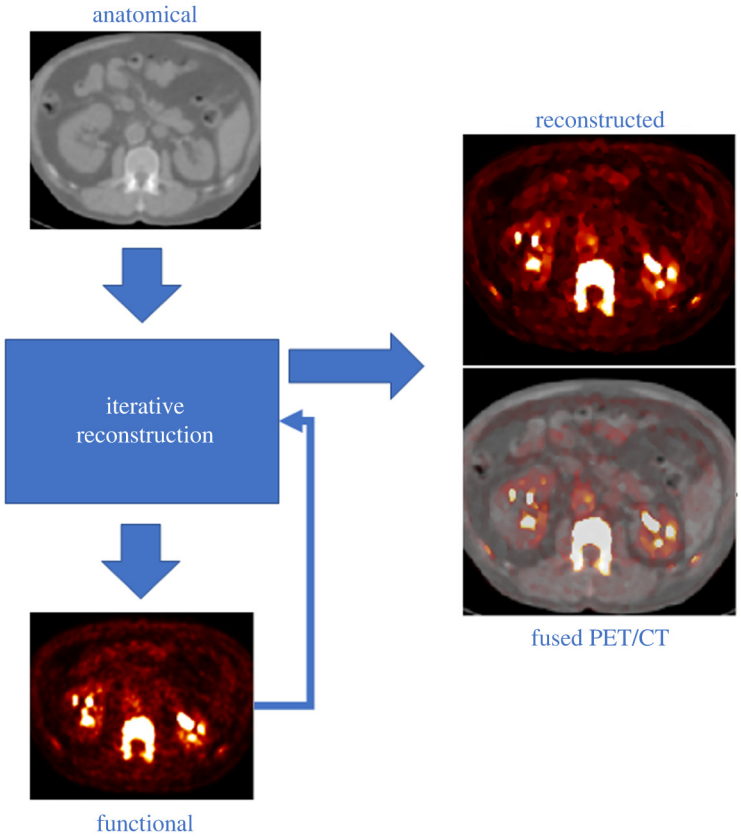


**Figure 2.5**: A schematic of the HKEM reconstruction process, originally published by Deidda et al [3], demonstrating the idea of including anatomical imaging from CT as a prior for PET reconstruction.

where $g_i, g_j$ represent the edge map. Different implementations will change this weighting function and how the edge map is calculated, but all aim to achieve a non-uniform resolution [30] and smoothing of the final image. For a Gaussian guided MR prior, $\beta$ becomes:

$$\beta_{ij} = \exp\left(-\frac{\|x_i - x_j\|}{2\sigma^2_{MR}}\right) \tag{2.8}$$

for PET signal $x$ and $\sigma$ is a scaling factor. Some methods choose to segment organ volumes from anatomical images [70], but these are exposed to segmentation errors and mis-registration between PET and anatomy images. The widely used Bowshers algorithm [71] avoids the requirement for segmented images by only applying a non-zero weighting to voxels with a small difference to their nearest neighbours in the anatomical image. However, this may still be affected by misalignment between imaging modalities. Another pitfall of these approaches is that by only penalising for edges present in the anatomical prior, PET features may be suppressed where their edges aren't present in MRI, for example, lesions in tissue that appears homogeneous in MR [67].

The Anato-functional method [67] extends Bowshers algorithm further to incorporate similarity weights for the PET current image update at each iteration, giving a function for the weighting of:

$$\beta_{ij} = \exp\left(-\frac{\|x_i - x_j\|}{2\sigma^2_{MR}}\right) \exp\left(-\frac{\|\theta_i^{(n)} - \theta_j^{(n)}\|}{2\sigma^2_{PET}}\right) \tag{2.9}$$

for MR signal intensity x and PET signal intensity $\theta$.

This avoids over-smoothing of PET unique features whilst still allowing anatomical boundary definition from the MR prior over a local neighbourhood of voxels. This implementation is the basis of the MR guided reconstruction developed for the GE Healthcare SIGNA PET/MR scanner which used in later chapters of the thesis. When a PET input is not provided, or the weighting for the PET component of the function is zero, the equation reduces back to Bowshers algorithm.

#### Kernel PET Reconstruction Methods

The kernel method is employed in machine learning to allow non-linear problems to be solved by linear estimation [72]. In PET image reconstruction, this allows for anatomical information to be introduced to the model based algorithms described in section 2.3.2. This is achieved by using a kernel, which corresponds to a dot product of feature maps for the data in a higher dimensional feature space so that

expressions formulated using the kernel can be expressed linearly. The kernel acts as a similarity measure so that previously unseen data can be estimated based on a known or training data set. So for data $\mathbf{v_i}, \mathbf{v_j} \in V$, the kernel is described as

$$k(\mathbf{v_i}, \mathbf{v_j}) = \langle \Phi(\mathbf{v_i}), \Phi(\mathbf{v_j}) \rangle \tag{2.10}$$

where $k$ is the kernel and $\Phi$ is it's feature map. As the kernel is always a positive definite kernel in these cases, the feature map is not required to be known and only the kernel need be defined. In medical imaging, this will most commonly take the form of the Gaussian kernel:

$$k(\mathbf{v_i}, \mathbf{v_j}) = \exp\left(-\frac{\|\mathbf{v_i} - \mathbf{v_l}\|^2}{2\sigma^2}\right) \tag{2.11}$$

where sigma controls edge sensitivity. To apply this to PET imaging, as described by Deidda et al. [29], the PET signal intensity at each pixel, $\lambda_j$, can be modelled as a function of a set of features, $\mathbf{f_j}$:

$$\lambda_j = \Gamma(\mathbf{f_j}) \tag{2.12}$$

Which may be any number of complex, high order models.

However, we can then map this to the feature space using

$$\Gamma(\mathbf{f_j}) = \mathbf{w}^T \Phi(\mathbf{f_j}) \tag{2.13}$$

where the weight vector $w$ is described as:

$$\mathbf{w} = \sum_{l=1}^{N} \alpha_l \Phi(\mathbf{f_l}) \tag{2.14}$$

and $\alpha_l$ is the coefficient vector. Substituting this in for the model described in equation 2.12 allows us to then take advantage of the kernel trick:

$$\lambda_j = \sum_{l=1}^{N} \alpha_l \Phi(\mathbf{f_l})^T \Phi(\mathbf{f_j}) = \sum_{l=1}^{N} \alpha_l k(\mathbf{f_j}, \mathbf{f_l}) \tag{2.15}$$

which in it's matrix form is $\mathbf{x} = \mathbf{K}\boldsymbol{\alpha}$. Looking back to equation 2.2, this matrix form can be used to create a kernel based projection model for use in EM approaches to PET image reconstruction as

$$\mathbf{Y} = \mathbf{AK}\boldsymbol{\alpha} + \mathbf{S} + \mathbf{R} \tag{2.16}$$

replacing $\lambda$ with its kernel representation so that the objective function is now

$$\hat{\alpha} = \arg\max_{\alpha \geq 0} \sum_{l=1}^{n_d} \{y_l log[aK\alpha]_l - [aK\alpha]_l\} \tag{2.17}$$

Because the kernel matrix would be too large to compute for the entire image, kernel PET reconstruction also uses a nearest neighbours approach to compute the kernel matrix over smaller voxel neighbourhoods.

Initial methods [73, 74] constructed the kernel matrix from the anatomical image prior before reconstruction and this remained consistent for each iteration, using the Gaussian kernel to compute a similarity coefficient between voxels in the anatomical prior. This allowed for MR guided reconstruction of PET data using kernel expectation maximisation (KEM), which achieved noise suppression but was found to over-smooth PET unique features [67]. Subsequently, KEM was extended to the hybrid kernel expectation maximisation (HKEM) algorithm [29]. In HKEM, the kernel matrix is formed with both a PET and MR component, with the PET component being iteration dependent. The kernel is now defined as:

$$k_{lj}^{(n)} = k_m(\mathbf{v_l}, \mathbf{v_j}) \cdot k_p(\mathbf{z_l}^{(n)}, \mathbf{z_j}^{(n)}) \tag{2.18}$$

with the MR component being:

$$k(\mathbf{v_l}, \mathbf{v_j}) = \exp\left(-\frac{\|\mathbf{v_l} - \mathbf{v_j}\|^2}{2\sigma_m^2}\right) \exp\left(-\frac{\|\mathbf{x_l} - \mathbf{x_j}\|^2}{2\sigma_{dm}^2}\right) \tag{2.19}$$

and the PET component:

$$k(\mathbf{z_l}^{(n)}, \mathbf{z_j}^{(n)}) = \exp\left(-\frac{\|\mathbf{z_l}^{(n)} - \mathbf{z_j}^{(n)}\|^2}{2\sigma_p^2}\right) \exp\left(-\frac{\|\mathbf{x_l} - \mathbf{x_j}\|^2}{2\sigma_{dp}^2}\right) \tag{2.20}$$

where the second Gaussian in each component acts on positional vectors $\mathbf{x_l}$ and $\mathbf{x_j}$ so that voxels must not only be similar in features, but also close range enough to be considered correlated voxels. This has been shown to preserve PET unique features better than the initial KEM implementation even before the addition of the PET kernel [75].

KEM reconstruction has been tested for brain imaging [67, 76], and HKEM for the carotid arteries [29], abdominal aorta [3] and brain [67].

## 2.4 Clinical Imaging of the Spinal Cord

### 2.4.1 MRI in the Spinal Cord

Spinal MRI for neurodegenerative diseases is performed in patients under investigation for a diagnosis of MS or ALS. In ALS it is predominantly used to exclude other diseases with a similar clinical presentation [32] however there is no specific indicator for ALS in medical imaging. For MS, MRI of the spinal cord plays a key role in diagnosis, as brain and spinal cord lesions are one of the diagnostic criteria [77]. Typically a spinal cord protocol for patients with neurological disorders would consist of a T1-weighted, T2-weighted and FLAIR pulse sequences [4, 78], some examples of which are shown in figure 2.6.

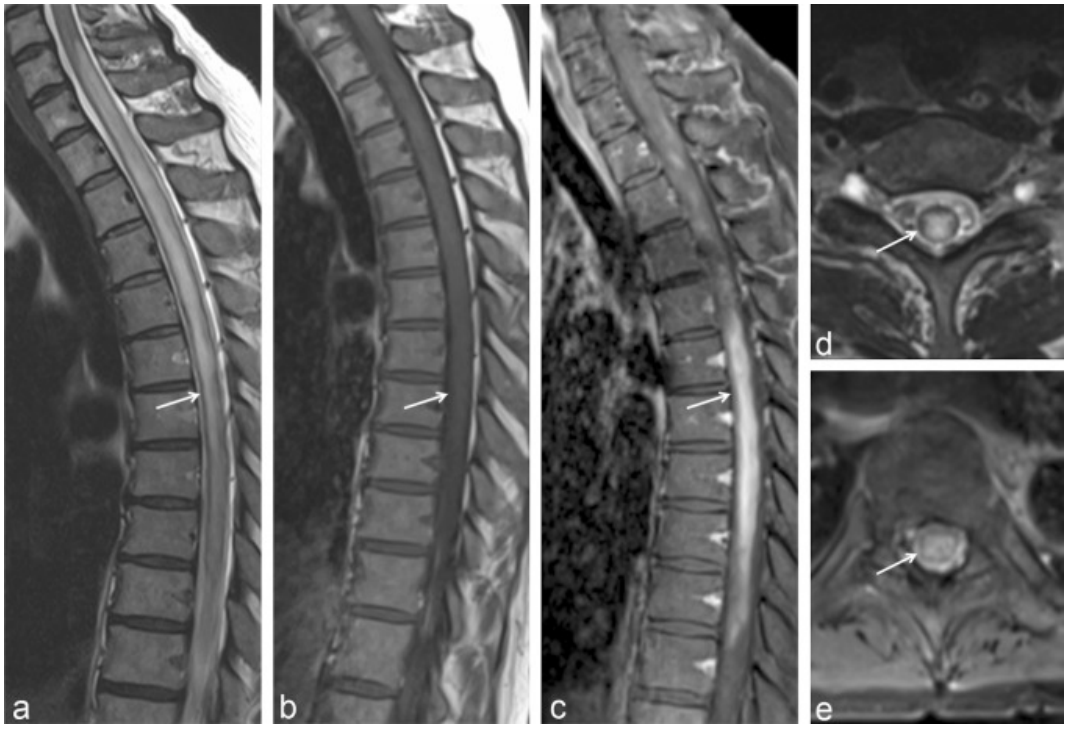


**Figure 2.6**: Examples of T1 (b without contrast agent, c and e with contrast agent) and T2 (a,d) weighted images of the spinal cord reproduced from [4]. The arrows indicate regions of swelling and edema within the spinal cord.

There is a clinical research interest in developing MRI sequences to observe evidence of upper motor neuron degeneration and develop biomarkers to monitor disease progression and therapeutic response, particularly within the spinal cord as this enables investigation of both upper and lower motor neurons [78].A decreased spinal cord cross sectional area measured in MRI images due to spinal atrophy has been shown to correlate with disease severity and progression in ALS

[78]. However, a reliable biomarker for ALS would be beneficial to tracking disease progression in clinical trials, provide a deeper understanding of disease mechanisms, and could prevent delays in diagnosis [35].

Optimising MR pulse sequences for spinal cord imaging can be challenging given its small diameter, field inhomogeneity in the region, partial volume effects, and movement artefacts arising from CSF flow, respiration and cardiac motion. [36].

### 2.4.2 PET in the Spinal Cord

For neurodegenerative diseases, the majority of PET imaging in clinical research focus on assessing brain function [35], although the tracers used are also suitable to assess different changes in the spinal cord. [$^{18}$F]FDG is the most widely used and accessible tracer, and can identify areas of inflammation and changes in metabolic activity corresponding to axonal damage in the spinal cord.

Several studies report an increased [$^{18}$F]FDG uptake in the cervical spinal cord of ALS patients compared to healthy controls [79–82] with more pronounced metabolic activation corresponding to patients presenting with clinical symptoms in the upper limb. Yamashita et al. have also paired [$^{18}$F]FDG PET with [$^{11}$C]FMZ PET [83] and [$^{18}$F]FMISO [84] data to demonstrate hypoxia in the cervical spinal cord corresponding to the rate of disease progression.

Conversely, there is no avid [$^{18}$F]FDG uptake in MS lesions [77], and a global reduction of [$^{18}$F]FDG uptake along the spinal cord has been reported compared to healthy controls [85]. As MS lesions are already visualised in MRI, PET research focuses on the imaging of myelin binding tracers for monitoring disease progression and treatment response in MS [86].

Performing PET/CT imaging on a structure as small as the spinal cord introduces a number of challenges due to its small size and a lack of tissue contrast in the spinal canal from the CT. Because contrast in these CT images is inadequate to identify the spinal cord itself, it is common to use the entire spinal canal as the region of interest and record maximum SUV ($SUV_{MAX}$) [5, 80] when establishing tracer uptake in the spinal cord. When using this method, the maximum uptake is assumed to occur in the spinal cord matter rather than CSF.

### 2.4.3 PET/MR in the Spinal Cord

To date there are no human PET/MR imaging studies in the spinal cord for neurodegenerative diseases. There are 6 studies in neuro-oncology investigating tumour visualisation, and 7 in other areas of research. These have mainly focused

on clinical findings with small patient cohorts, although some have had a more technical focus to optimise patient imaging.

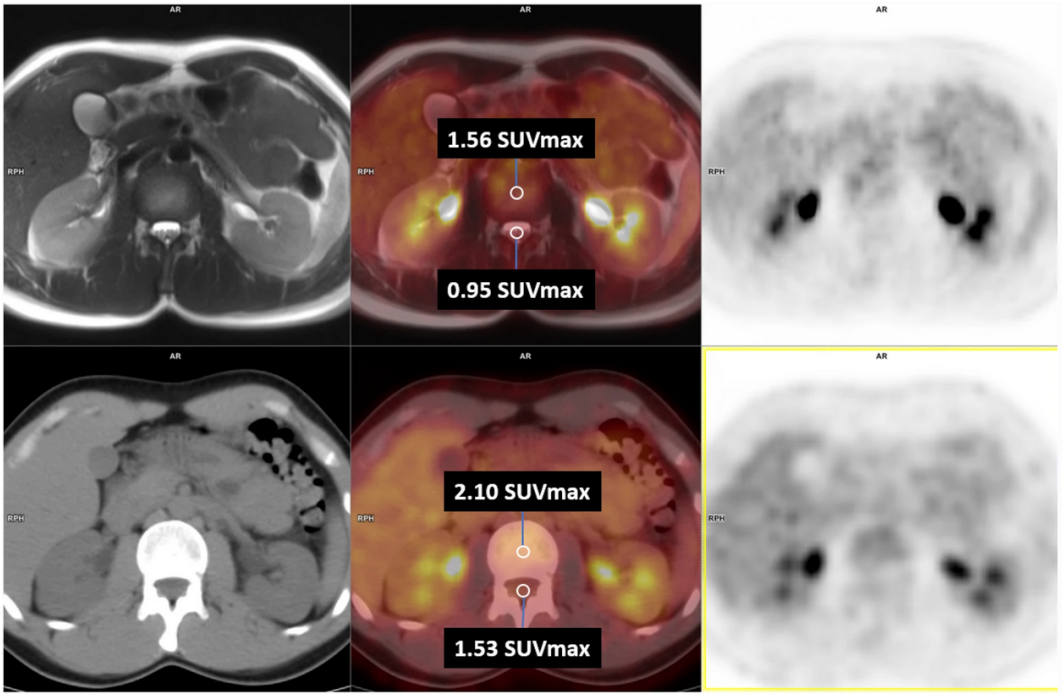


**Figure 2.7**: Examples of whole body PET/MR images from which spinal cord [$^{18}$F]FDG uptake measurements were made in [5], showing and MRI image (top) and CT image (bottom) in the first column, fusion images in the second and PET images in the third column.

Aiello et al [5] published their results comparing [$^{18}$F]FDG uptake in the spinal cord in PET/MR to PET/CT acquisitions. Patients were retrospectively recruited from whole body lymphoma staging scans performed on both PET/CT and PET/MR, with no clinical indication of spinal cord injury or tumour involvement. Region of interest (ROI) analysis was used to calculate SUV for normal spinal cord and compare this to the values obtained using established PET/CT methods, demonstrated in figure 2.7. By using the MR acquisition to delineate the spinal cord they were able to analyse average SUV in the spinal cord specifically, rather than the more commonly used $SUV_{MAX}$ from a region encompassing the entire spinal canal. Results for Normalised Standard Uptake Values (NSUV) are also provided, where uptake is taken as a ratio to background region. SUVs of the spinal cord matched well between PET/MR and PET/CT, but NSUVs were higher in the PET/MR images. This study indicates that spinal cord PET/MRI is quantifiable within the expected range of activity uptake, and provides a set of baseline values against which to compare future work. The group also performed a study looking at the

impact of introducing additional tissue groups to MR attenuation correction templates [87]. However, in both studies data was used retrospectively from whole body acquisitions and were not optimised for spinal acquisitions.

Receptor specific PET/MRI has already demonstrated significant benefit in the characterisation of therapies in neurological disorders in preclinical research [88]. By performing dynamic PET in PET/MRI studies, it is possible to quantify radiotracer uptake changes alongside MRI functional changes according to stimuli [89]. Such works suggest that the monitoring of therapeutic activity in human studies may also be possible using a combination of DTI and the range of specific PET tracers available.

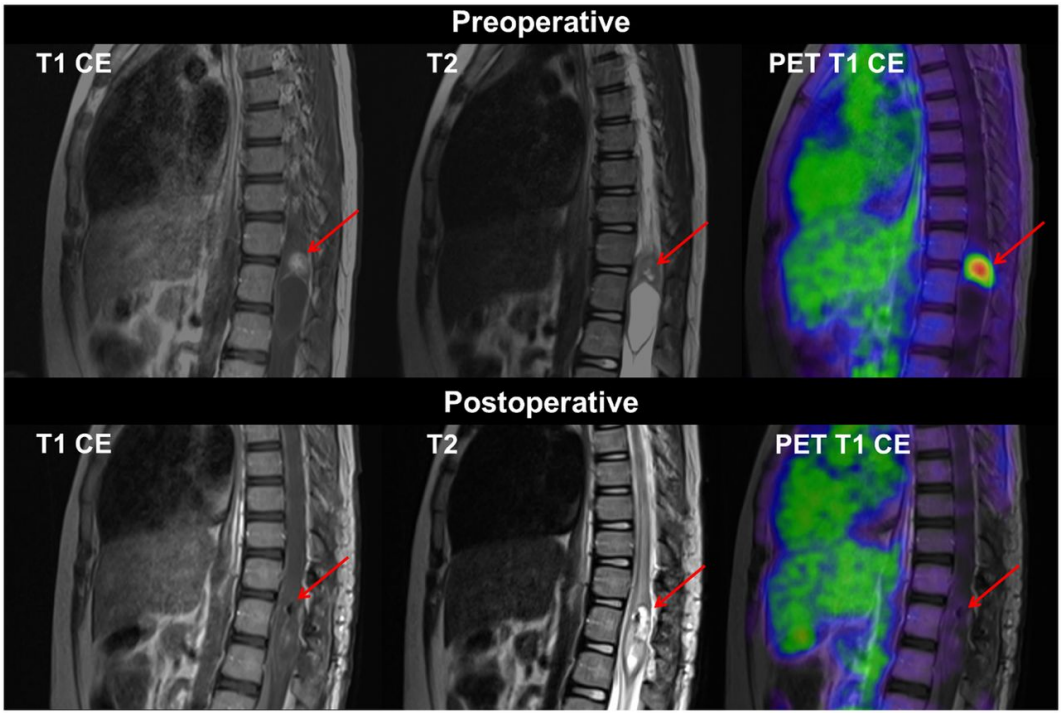


**Figure 2.8**: Examples of PET/MR images of the spinal cord using the tracer FET for pre- and post-operative assesment in pediatric patients with spinal cord tumours, from [6].

Another benefit to PET/MRI is the reduced radiation exposure compared to PET/CT [90]. This is a significant consideration when imaging paediatrics and longitudinal studies, however recent developments in PET/CT have been able to significantly reduce radiation dose from the CT component [91]. Marner et al. [6, 92] have presented the clinical experience of Denmark University Hospital in using PET/MRI [$^{18}$F]FET for paediatric patients with neurological tumours, images from which are reproduced in figure 2.8. PET/MR is used in their workflow for patients where there is difficulty in identifying malignant tumours from MRI alone. More

broadly, PET/MRI in the assessment of spinal tumours in adult patients has also shown the benefit a combined PET/MRI scan has to offer, such as whole body PET staging able to identify both spinal and none-spinal tumours combined with site specific MRI for identification of tumours with low FDG uptake [93]. Acquiring both datasets in one scanning session is also beneficial to patients as it decreases the time spent undergoing diagnostic tests in the hospital.

These studies along with extensive brain imaging performed with PET/MRI [88, 94–98] using FDG, TSPO, $\beta$-Amyloid binding and myelin protein binding PET tracers, provide strong indications of the clinical benefits to spinal cord PET/MRI in differential diagnosis through providing complementary information regarding pathophysiology and disease progression.

Although there are no human studies imaging the spinal cord for neurodegenerative diseases performed using a combined PET/MRI published to date, there are other PET/MR spinal cord studies in other areas of medicine [80, 99] in addition to previous research where the modalities were acquired separately and the required co-registration [83, 84].

## 2.5 Technical Challenges to Spinal Cord PET/MRI

Studies imaging the spinal cord with PET/MR are limited in the research of neurodegenerative diseases, despite the value to the field demonstrated by both PET and MRI as summarised in this chapter. The wider use of PET radiopharmaceuticals that target specific biological pathways known for involvement in neurodegenerative diseases and neuroinflammation also presents a promising avenue of research for spinal cord PET/MR. Where it has been utilised, spinal cord PET/MR has been performed using a whole body imaging approach to both the PET and MRI protocols and image reconstruction. The main technical issues for quantifying spinal cord tracer uptake in PET/MR are:

- Vertebral bone representation in MR derived attenuation correction
- Partial volume effects

Attenuation correction remains a challenge to spinal cord PET/MRI. Samarin et al. [58] showed that replacing bone attenuation coefficients with tissue in attenuation maps yields results close to the true values for lesions near to smaller bone structures such as the ribs, and soft tissue regions distant from the skeleton. However, this didn't hold true for lesions within the spine and pelvis, which were underestimated by up to 16% [58]. However, it has also been shown that attribut-

ing incorrect bone attenuation coefficients, or misclassifying soft tissue as bone also negatively impacts measured PET tracer uptake and PET image quality [19].

Partial volume effects (PVE) are also a source of error in PET/MR as reconstructed PET scanner resolution for the GE Signa PET/MR is 4.2mm in the axial plane and 5.8mm in the axial plane [100](increasing to 3.7mm and 4.8mm when reconstructed with Time of Flight algorithms). As discussed in section 2.1, the spinal cord diameter ranges from an average of 6-8mm in the anterior-posterior direction and 8-13mm in the transverse direction, so is within the order of magnitude to be affected by PVE. Indeed, Patel et al. (2017) [101] show that neighbouring bone marrow uptake correlates to measured spinal cord uptake, suggesting the proximity of these regions within the vertebral column may be leading to an averaging of activities across the two structures. As the positrons mean free path length before annihilation can also affect activity localisation, imaging with different radionuclides may have different PVE, as will the presence of an external magnetic field which can disrupt the proton path, as is the case in PET/MRI [102]. However, given that PET/MRI provides a high resolution, co-registered MR images of soft tissue anatomy, efforts to correct for this in post-processing [44, 103] and in image reconstruction [30], as described in section 2.3, have been developed and are becoming more widely used in PET/MRI. This thesis focuses on approaches that incorporate MR images into PET image reconstruction algorithms.

These unresolved sources of error limit the use of spinal cord PET/MR in research studies, particularly where quantitative accuracy are required. However, the extent of the impact of these effects has not previously been explored. Similarly, partial volume correction, both post-reconstruction approaches and algorithms that incorporate this into the reconstruction process, is an active area of research in PET imaging. However, the solutions presented in section 2.3 have not been assessed for their performance in the spinal cord.

In this thesis, the technical challenges to quantification in PET images of the spinal cord acquired with the GE Signa PET/MRI scanner have been investigated. This is the first study to use phantom and simulation work to explore the impact of incorrect attenuation correction and partial volume effects in the spinal cord specifically. Novel MR guided image reconstruction algorithms were then assessed for image quality and semi-quantitative accuracy in the spinal cord.

# Chapter 3

# Multimodal Phantoms for Clinical PET/MRI

The main body of this section was composed as an article published in the European Journal of Nuclear Medicine and Molecular Imaging Physics [31].

## 3.1 Introduction

Positron Emission Tomography (PET) and Magnetic Resonance Imaging (MRI) are both well established clinical imaging modalities. PET images are formed by detecting the annihilation photons of positrons emitted by a radioactive tracer administered to patients [14]. These are considered functional images, as tracers are targeted to a particular physiological process and the amount of radiation detected is proportional to the uptake of tracer in a region. Measures such as Standardised Uptake Value (SUV) allow the radiotracer uptake of a region to be quantified. MRI detects a radio frequency (RF) signal emitted by protons excited by RF pulses in a strong external magnetic field [37]. This can produce high resolution anatomical images with high contrast between different soft tissues. In recent years, combined PET/MRI scanners have been released by manufacturers and are entering clinical use. These scanners allow for the simultaneous acquisition of PET and MRI data resulting in combined images from both modalities, the advantages of which are evident in a range of clinical areas [23].

In both PET and MRI, test objects known as phantoms are used for scanner performance testing and monitoring, verification of new image acquisition protocols and reconstruction methods, standardisation across equipment and other experimental work. PET phantoms are typically solid vessels of various size and geometry filled with different concentrations of radiotracer solution [104]. For

quality assurance and performance testing, these would typically be a single container filled with fluid to provide a uniform image, or larger acrylic containers with inserts of simple geometries such as cylinders or spheres. The National Electrical Manufacturers Association's (NEMA) report NEMA NU-2 [105] sets out the measurements required for performance assessment of clinical PET systems. This covers assessments of image uniformity, spatial resolution, sensitivity and the assessment of scattered emissions, detection of randoms and the accuracy of any applied corrections. These are typically assessed by filling a phantom or test object of a know size and geometry with a known amount of radioactive tracer. Additionally, phantoms of a known activity concentration are required for the calibration of PET systems to ensure accurate quantification of tracer uptake. This allows for determination of the number of decay events detected against the amount of radioactive tracer the phantom is known to contain. Anthropomorphic phantoms, with cavities which appear to match anatomical geometries in PET images, are used to simulate radiotracer uptake in a specific organ, often against a lower activity background.

MRI phantoms adhere to similar designs for performance testing and are often filled with a highly MRI-visible fluid such as Nickel Chloride or Manganese Chloride solution, as used in the phantom developed by the National Institute of Standards and Technology (NIST), the International Society for Magnetic Resonance in Medicine (ISMRM), the NIST/ISMRM system phantom [106] and American College of Radiology (ACR) phantom [107]. A typical quality assurance program for MRI would look to measure signal to noise ratio (SNR), uniformity, resolution, spatial linearity and assess for imaging artifacts such as distortions and ghosting [108]. The NIST phantom allows for quantitative assessment in MRI, by mapping inserts of known T1, T2 and proton density values with quantitative MRI sequences to validate measurements made by the scanner. Anthropomorphic phantoms in MRI often use gels such as agar to achieve MRI relaxation properties close to human tissues [109].

In these existing forms, neither PET nor MRI phantoms are compatible for imaging with the other modality to take advantage of the simultaneous acquisition available with a combined PET/MRI scanner, simply due to the difference in radiological properties required.

Valladares et al. [110] compared the quality assurance programs for PET/MRI scanners of 8 sites across Europe and found significant variation in approaches. The authors recommend a regime in line with available guidelines such as the National Electrical Manufacturers Association's (NEMA) report NEMA NU-2 [105] for PET and the American Association of Physicists in Medicine (AAPM) Report

028 for MRI [111]. This satisfactorily covers performance monitoring of scanners, but still leaves both modalities tested individually. This doesn't reflect clinical use of the scanners, and in particular doesn't allow for a complete assessment of the image reconstruction process when using MRI based attenuation maps with PET data. It also raises the question as to how phantoms have been used in the field of PET/MRI to date, and to what extent phantoms have been developed that are compatible for simultaneous PET/MRI.

This article examines publications between 2011 and 2021 to identify the phantoms used and developed by institutions working with clinical PET/MRI scanners. In order for a publication to be included in this review, the utility of both PET and MRI data sets must be demonstrated, thus indicating that the phantom chosen shows potential as a test object for simultaneous PET/MRI acquisitions. Mathematical and computational/software phantoms are not considered in this review.

The main part of this review begins by summarising the materials used in phantom design and the challenges faced when choosing materials to create PET/MRI phantoms. We then categorise the phantoms identified from literature into two broad categories. First we cover geometric phantoms, those that feature simple geometries such as those designed for quality assurance programs, which may be commercially available or manufactured in-house. The second is anthropomorphic phantoms, designed to replicate specific human anatomy, physiology or tissue properties in PET/MRI for which there are commercially available and in-house manufactured solutions. For each category we present phantom designs and the use cases demonstrated in recent publications, a summary of which can be seen in figure 3.1. We then discuss how the presented phantoms address key research areas posed in the field of PET/MRI, and the developments still needed to create widely available, reproducible phantoms suitable for simultaneous PET/MRI acquisitions.

## 3.2 Materials in Phantom Design

Ensuring the materials chosen for phantom development exhibit the properties required for both PET and MRI imaging simultaneously can be challenging as PET/CT phantoms focus on radiotracer distribution and electron density of materials, whilst MRI phantoms are optimised to the desired proton relaxation times. A list of the polymers mentioned in this review and their abbreviations are shown in table 3.1. Polymethyl methacrylate (PMMA) is the preferred choice in commercially available phantoms as it is strong, transparent and offers a similar x-ray radiation attenuation to human tissue [14]. However, it is not MRI visible, so the

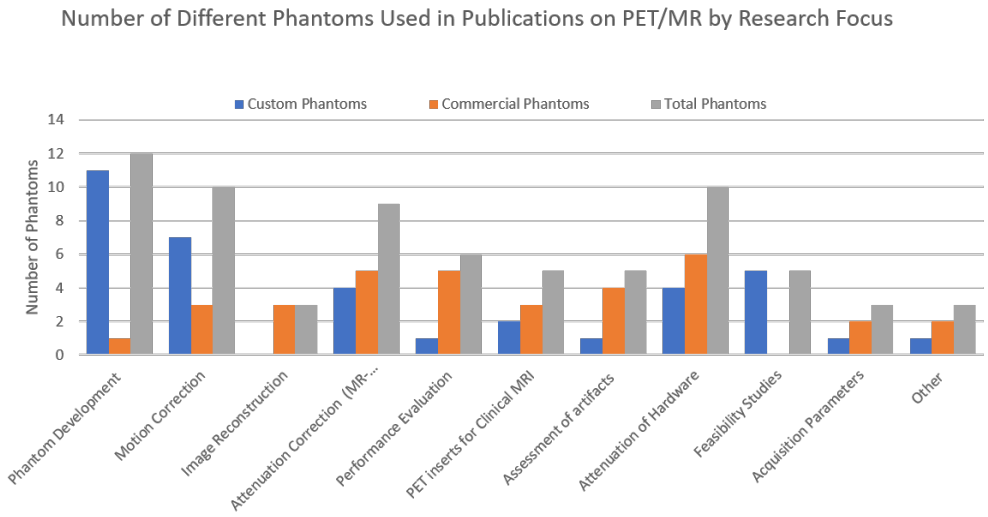


**Figure 3.1**: Research and publication categories within MRI identified in this review and the number of unique phantoms used in each category, separated by custom and commercially available phantom designs.

attenuation properties of PMMA phantoms cannot be easily derived in PET/MRI acquisitions and so alternative materials for phantom development have been explored.

| Abbreviation | Polymer Name |
|---|---|
| PA | Polyamide |
| PE | Polyethylene |
| PEEK | Polyether Ether Ketone |
| PMMA | Poly(Methyl Methacrylate) |
| PP | Polypropylene |
| PTFE | Polytetrafluoroethylene |
| PU | Polyurethane |
| PVA | Polyvinyl Alcohol |
| PVC | Polyvinyl Chloride |

**Table 3.1**: Abbreviations and corresponding full names of polymers used in the manufacture of phantoms featured in this review.

Phantom development, including characterisation of the materials, is an active area of research among groups performing phantom studies in PET/MRI, with 12 phantoms featured in publications on phantom development between 2011 and 2021, as shown in figure 3.1. In-house manufactured anthropomorphic and tissue equivalent phantoms in particular are often featured in a dedicated publication to describe the phantom design and manufacture, or demonstrate its properties as a

suitable PET/MRI phantom.

### 3.2.1 Tissue Mimicking Materials

A recent review on tissue mimicking materials has been published by McGarry et al. [112] providing an overview of the material properties and manufacture methods across a range of imaging modalities. The authors outlined both the requirement for and challenges present in developing tissue mimicking material displaying the desired properties for multiple imaging modalities. Here, an in-depth focus on the materials used as tissue analogues in PET/MRI phantom development is presented, a summary of which is provided in table 3.2.

| Tissue Type | Materials Used |
|---|---|
| Brain | Agarose Gel, PE, Saline soaked Cotton, Water |
| Bone | Gypsum plaster, Dipotassium Phosphate, Cadaver, Petroleum Jelly |
| Soft Tissue | Agarose Gel, Methyl-cellulose Gel, Gelatin, Gel (unspecified), Saline, Water |
| Adipose | Peanut oil, Silicone |
| Tumour/lesion | Wax, Agarose Gel, Gel (unspecified), Gelatin, Plastic or Glass Spheres |
| Heart | Silicone, Gel (unspecified), Water |
| Lung | Rubber Balloon, Cadaver, Silicone |
| Other Tissue | Rubber Balloon, Hosepipe, Silicone, Agarose Gel |
| Other Materials | PMMA, VeroClear, Agilus 30 Clear, PU, PU/PVA mix |

**Table 3.2**: Materials used in anthropomorphic phantoms categorised by the tissues they have been used to represent.

Three phantoms were developed to include animal cadavers of porcine and bovine origin for bone and lung tissue. Animal cadavers can provide materials with similar structure and properties to the equivalent human tissues, however these may be altered in ex-vivo samples [113]. Two of these phantoms were used as part of the validation process for MRI-based attenuation correction [114, 115]. One study described a phantom built with animal femur bone and lung lobe as a feasible solution to create tissue equivalent phantoms for PET, CT and MRI [57]. However, consideration is required as to how components will be cleaned between experiments, to ensure a like-for-like replacement for cadavers at appropriate time intervals and to accommodate for the embalming process. Whilst there are benefits to utilising such phantoms in work around tissue classification in MRI-based attenuation techniques, particularly where a range of tissue types are represented [116], there are no known and verified relaxation properties or attenuation coef-

ficients to validate against. Applications are also limited by a lack of anthropomorphism and the limitation of introducing a meaningful and realistic radiotracer distribution to a cadaver.

### Soft Tissue

Three approaches to modelling brain tissue are encountered in this review. The Hoffman Phantom [117](Data Spectrum Inc.) and Iida phantom [118], as shown in figure 3.2, both form models of the human head using polymers for white matter and an open compartment filled with radiotracer solution for grey matter. This provides an ideal radiotracer distribution, but the polymer structure is invisible to MRI. Saline soaked cotton as used by Okazawa et al. offers limited use as a brain tissue surrogate given that in the form presented no radiotracer is administered [119]. Agarose gel used by Harries et al. benefits from displaying closer MRI signal properties to soft tissue than water or saline [120], however establishing a detailed grey and white matter structure could be challenging in terms of structural integrity, level of detail achievable and how a heterogeneous radiotracer distribution could be established or even reproduced.

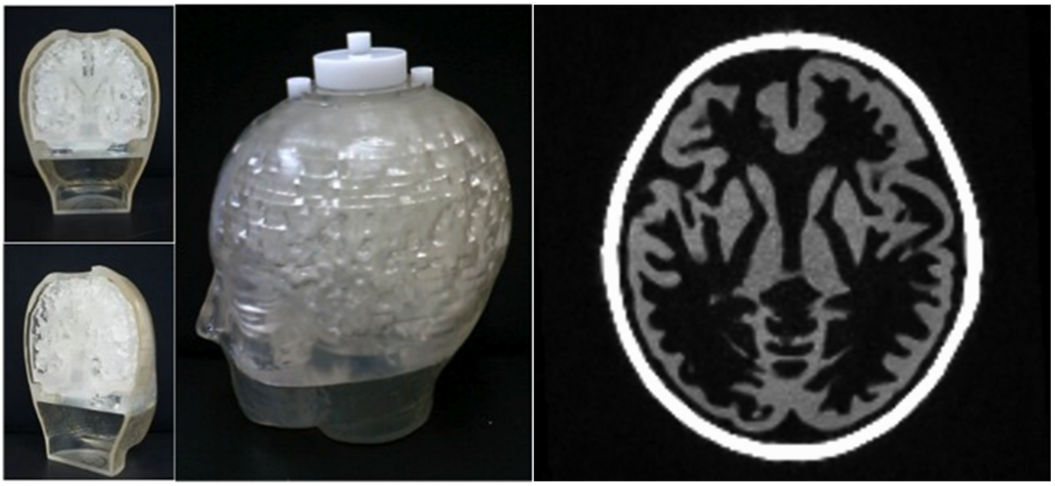

**Figure 3.2**: Images of the Iida brain phantom, reproduced from [7]

Agarose, gelatin and methyl-cellulose gels are used more widely as soft tissue surrogates in several phantoms identified for this review [8, 10, 57, 115, 121, 122]. The ability to customise the MRI relaxation properties of gels with relative ease at manufacture by varying the concentration of gelling and contrast agents, demonstrated extensively by Gillmann et al. [121], allows for flexibility in the number of tissue types represented. Gels can be used to fill cavities or moulded to hold structure without a casing, both of which provided a reproducible geometry.

Moulded structures such as tumours or lesions may then be placed inside a larger gel tissue surrogate [122]. In phantoms simulating cardiac and respiratory motion [9, 10, 123, 124], gels offer an alternative to water whilst maintaining the flexibility to allow movement to occur. Additionally, gels are easily manufactured in-house without the need for specialist equipment.

However, if using short half-life radiotracers such as [$^{18}$F]FDG, gel tissue surrogates must be remade each day they are required, so manufacture and setting time must be accounted for to ensure sufficient radiation is detectable at time of scanning. Alternatively a long half-life radionuclide could be suspended within the gel, but this would require careful consideration of the safe long term storage and disposal of the radioactive gel. Furthermore, each manufacture session is subject to a level uncertainty. McIlvain et al. [125] have encouraged sites to understand the impact the variations in manufacture may have on the material properties. Using gels inside intricate casings may introduce air bubbles during manufacture, and be difficult to clean for re-use. Finally, all of the phantoms identified in this review use homogeneous radiotracer distribution throughout each gel tissue surrogate, however this does not represent every clinical scenario as highlighted by Valladares et al. [126], who presented proposed solutions for heterogeneous tissue equivalent materials for medical imaging phantoms.

#### Bone

Bone material analogues are challenging to create for PET/MRI applications as the chosen material should exhibit a cortical bone, or average bone, electron density for realistic PET attenuation, whilst maintaining very short T1 and T2 relaxation times.

Phantoms with bone surrogates were most commonly created in house using gypsum plaster [120, 121, 127] doped with iodine CT contrast agents and either gadolinium MRI contrast agents or copper sulfate to modify the linear attenuation coefficient and relaxation times respectively. Chandramohan et al. [127] assessed the radiological properties of several samples of gypsum plaster mixed with varying concentrations of each doping agent for comparison with human bone. They found that plaster doped with copper sulfate provided the combined radiological properties suitable to mimic cortical bone, however the relaxation properties of the material were unstable over time and were affected by the introduction of microbubbles into the plaster during manufacture, warranting further investigation. Harries et al. [120] casted a skull from iodine doped plaster, which is classified as bone in five out of six MRI-based attenuation maps, but results in an underestimation of PET activity within the phantom of on average 5%, to a maximum

of 11%. Gillmann et al. [121] took additional steps to create bone structures that also include a bone marrow surrogate of petroleum jelly mixed with dipotassium hydroxide, allowing for lesions to be place inside. As the use of PET/MRI in areas of the body with larger bone structures increases, the differentiation between cortical bone and other features such as bone marrow may become more relevant in phantom experiments. Dipotassium phosphate was used as a bone equivalent material in the Iida phantom [118], however as a liquid solution it is highly visible in MRI images and so is not classified as bone in MRI-based attenuation maps [128].

Overall, gypsum plaster has presented a promising solution to replicating the material properties of cortical bone in PET/MRI phantoms and is a widely available crafting material. However further work is required to assess the effects of different manufacturing methods and the long term stability of the material properties of doped plaster, as has previously been performed for agarose gels in MRI phantom work [125].

#### Adipose Tissue

Fats are largely ignored across the phantoms produced, with only individual use of silicone [120] and peanut oil [121]. Of these materials, peanut oil provided MRI relaxation properties close to those of adipose tissue, whilst silicone exhibits a much shorter T2* [120]. Phantoms designed to represent anatomy such as the breast would benefit from further investigation into use of materials with radiological properties similar to adipose tissue.

### 3.2.2 Polymers and 3D Printing

Casings for organs and the overall phantom were manufactured using a variety of polymers. Most commonly PMMA and PU were used, but 3D printable polymers were also used for individual organs. Of the phantoms featured in this review, the Iida phantom [118] provided attenuation properties for the 3D printed polymer and Talalwa et al. [129] demonstrated the dielectric properties of their proposed porous MRI-visible 3D-printed polymer made of a PU/PVA mix. Gillman et al. [121] reported the CT Hounsfield units and MRI relaxation times for VeroClear (Stratasys) but this is not referenced to any tissue value, suggesting it was not selected to exhibit tissue equivalent properties.

In their systematic review to identify trends in the use of 3D printing in the development of medical imaging phantoms, Fillipou and Tsoumpas [130] found that radiological properties are not commonly tested by manufacturers for 3D

printing. However, Rausch et al. [131] have recently created a phantom using 3D printed polymer RGD252 (Stratasys), previously demonstrated as MRI visible [132], that is visible in both modalities for simultaneous PET/MRI acquisitions.

NIST have released two publications [133, 134] demonstrating CT and MRI properties for a range of commercially available 3D printable polymers for comparison with human tissue. Although several challenges exist to utilising 3D printed phantoms in multimodal imaging [130], future work would benefit from further consideration of the MRI relaxation and PET attenuation properties when choosing polymers from which to 3D print PET/MRI phantoms. In particular, this would encourage the correct classification of structures for MRI-based attenuation correction. Silicone and rubber balloons used to represent the heart [9, 10], lung [123, 124] or bladder [121] also lack MRI visibility. Whilst this is less of an issue for lung tissue as this is typically classified as air, care must be taken to ensure this does not lead to an overestimation of PET activity.

### 3.2.3 Summary of materials in PET/MRI Phantom Design

Gel based phantoms with radiotracer introduced prior to setting provide the option of creating phantoms with soft tissue equivalent MRI relaxation times with a uniform radiotracer distribution, however radiotracer solutions of water or saline are also commonly used and may be doped with gadolinum-based contrast agent. Gypsum plaster has been the most utilised option for bone analogue materials, however further work is required to establish the stability of the phantoms produced and reproducibility of manufacture methods. Few options have been explored in mimicking adipose tissues. Advances in 3D printing and the range of polymers available may offer solutions in the future in creating phantoms for simultaneous PET/MRI, particularly in light of the work performed in assessing the radiological properties of materials available. However, these materials generally lack the large scale manufacture and shelf life capable of creating reproducible phantoms able to be distributed across multiple sites. Subsequently, established polymers in phantom design such as PMMA continue to be used widely for building PET/MRI phantoms despite their lack of signal in MRI.

## 3.3 Geometric and Homogeneous Phantoms

Geometric phantoms are those which feature simple geometric inserts and cannot be considered anthropomorphic. Homogeneous phantoms are phantoms for which there are no inserts, providing a uniform fluid distribution within the phantom body. Twenty-five geometric or homogeneous phantoms were identified in

this review, a breakdown of which is shown in figure 3.3. Although this is only slightly more than half of the phantoms encountered, they appear in 59 of the 92 publications reviewed. Thirteen of these take the form of geometric phantoms, often used in quality assurance measurements. The 9 homogeneous phantoms take the form of a cylindrical container, bottle or canister filled with a single fluid, and are considered to be commercially available.

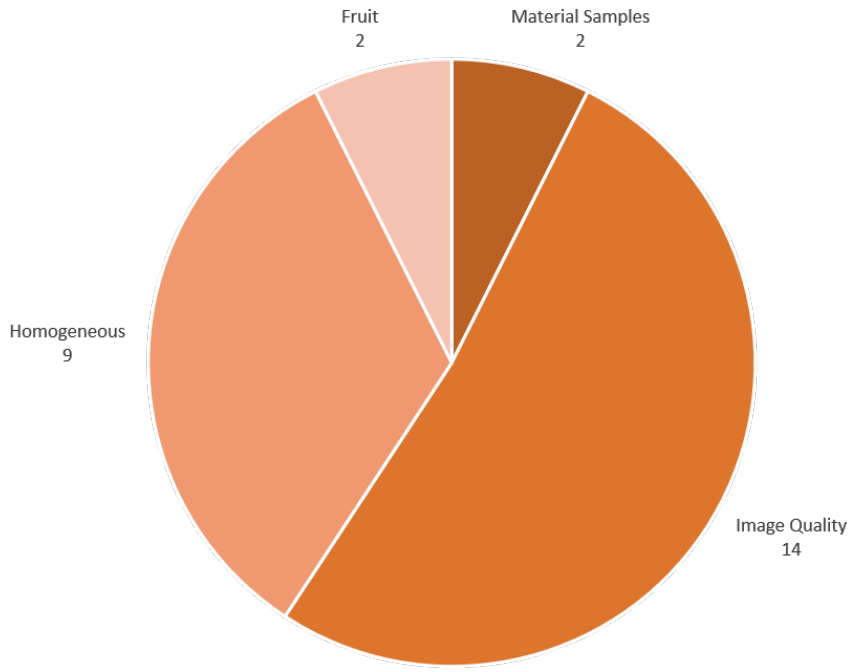


**Figure 3.3**: Physical PET/MRI phantoms categorised by design features. Material samples consist of small amounts of material for characterisation. The fruit category refers to the use of modified fruits as PET/MRI test objects, although these are not discussed in detail.

Of the Geometric phantoms, 9 are custom designed and included in 14 publications. 31 publications use 5 commercially available geometric phantoms, the most common being the International Electrotechnical Commission (IEC) NEMA Body Phantom featured in 19 publications. The predominant use cases for these phantoms within PET/MRI literature are measuring image quality and scanner performance, verifying MRI based attenuation correction and image reconstruction methods, and generating attenuation maps for radio-frequency coils or other hardware.

### 3.3.1 Homogeneous Phantoms

Homogeneous phantoms act as a test object filled with a single, homogeneous fluid, an example of an MRI acquisition for which is shown in figure 3.4. These are simple to use and give indication of performance through assessment of image uniformity and image noise. They are easily accessible, given that they can be fashioned from any water-tight, MRI safe container. The variety of containers available allows researchers to tailor the size of the phantom appropriately.

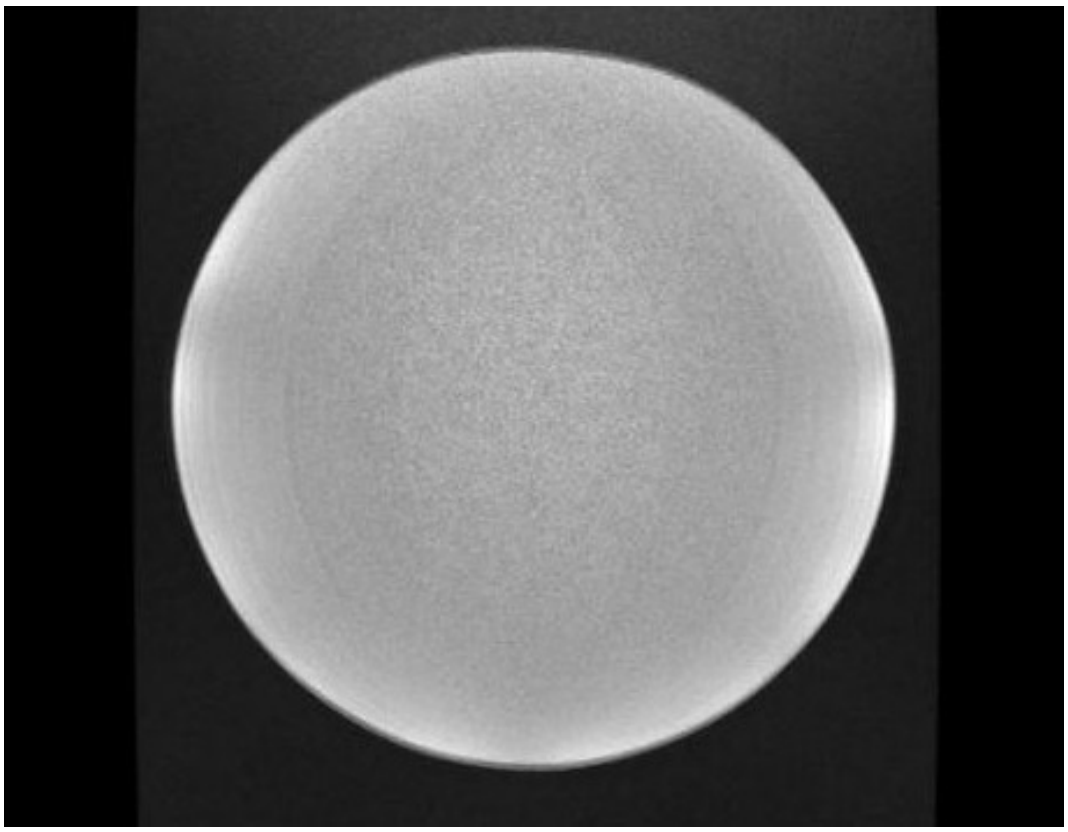

**Figure 3.4**: Cross section of a uniform phantom acquired in MRI (GE Signa PET/MRI scanner).

MRI visibility can be improved by using Nickel Sulfate [135], Sodium Chloride [136] or introducing a gadolinium-based contrast agent [137] alongside the radioactive tracer. This allows researchers to create solutions that can be imaged with both PET and MRI, however containers are not MRI visible and so cannot easily be included in MRI-based attenuation maps. This can be mitigated by using containers with thin walls to minimise PET attenuation by the container and allow for attenuation maps to be approximated to the fluid volume. No two groups of authors used the same uniform phantom, and phantom volumes range from

160ml to 29L. This reflects the differences in studies presented, but also suggests a lack of a standardised approach to assessing uniformity in PET/MRI.

### 3.3.2 Commercially Available Geometric Phantoms

All commercially available geometric phantoms featured in this review are phantoms initially designed for PET or Nuclear Medicine use and licensed by Data Spectrum Corporation:

- IEC (NEMA) Body Phantom
- Esser (ACR) PET Phantom
- Jaszczak Phantom
- NEMA 94 PET Phantom
- Mini Deluxe Phantom

They are widely available and many sites with existing Nuclear Medicine and PET facilities are likely to already possess a subset of these phantoms in order to adhere to quality assurance guidelines [105]. In particular, the IEC (NEMA) Body Phantom continues to be recommended for PET and PET/MRI acceptance testing and quality assurance under the NEMA NU-2 (2018) standard [105, 110]. It consists of a large, elliptical PMMA container with a central cylinder filled with polystyrene, around which hollow spheres are suspended from one end of the phantom. The standardised geometry, manufacture and protocols used ensure comparable measurements between sites and promote reproducibility across different scanners. This is reflected in literature through publications where the IEC Body Phantoms was used to evaluate PET/MRI scanner performance [138–140], and compare performance and protocols to PET/CT [141–144] prior to introducing patients studies. Krokos et al. [139] illustrated the crucial example of ensuring standardisation between several PET/MRI scanners for use in multicentre dementia trials.

A significant drawback of these phantoms is the inability to create accurate MRI-based attenuation maps due to the widespread use of PMMA for the phantom body and its lack of visibility in MRI. Ziegler et al. [145] compare results generated from the NEMA NU-2 Protocol for a Siemens Biograph mMR using images reconstructed with both an MRI-derived attenuation map and a CT-derived attenuation map. They found that using an MRI-derived attenuation map decreased contrast recovery in radioactive spheres, increased contrast recovery in

non-radioactive spheres and increased background variability, indicating a degradation in both image quality and PET quantification due to insufficient correction for attenuation. Their recommended solution was to acquire a CT scan of the phantom separately in order to generate a suitable attenuation map that can be registered to the MRI or PET images to perform image reconstruction of the phantom offline. Further comparisons [146] extended this to include the MRI-based attenuation correction methods employed in the Philips Ingenuity TOF and GE Signa PET/MRI scanners for phantoms, as well as assessment of clinical MRI-based attenuation correction in phantom studies. Replacement of the MRI-based attenuation map with a registered CT-based map appears to be the preferred solution in publications included in this review where geometric phantoms are used. As such, vendors provide a predefined PET attenuation map in the scanner reconstruction software for the IEC Body Phantom for PET performance testing under the NEMA protocol, however this doesn't extend to all commercially available phantoms. The drawback to this however, is that it doesn't allow for assessment of PET images reconstructed with MR derived attenuation maps, which is the method used for patient imaging.

#### Addressing MRI Visibility of Commercially Available Phantoms

In an earlier publication, Ziegler et al. [147] assessed a variety of fluid fillings to improve MRI visibility and attenuation map generation for the IEC Body Phantom. By varying the fluid filling for the phantom, they were able to significantly improve homogeneity in the MRI images and reduce bias in PET data resulting from inconsistencies in the MRI-based attenuation map. The key finding was that a pure water radiotracer solution as recommended in the NEMA NU-2 protocol was the least suitable of the fluids assessed, with triethylene glycol providing the greatest homogeneity. However, none of the fluids presented appear to provide a robust solution for routine use due to risk of toxicity, additional cleaning requirements and costs. Use of any alternative fluids also does not address a lack of phantom housing visibility in MRI.

Currently, no geometric phantoms for the quality assurance of PET/MRI systems exist on the market that are both PET and MRI visible. Whilst many performance issues will be detected by separate testing of MRI and PET components of the scanner, enabling quality assurance phantoms to undergo simultaneous imaging and use the same attenuation correction and image reconstruction methods as would be used clinically is highly desirable. This would act to both confirm the performance of these systems and to allow phantom testing to form part of wider imaging protocol validation projects. Additionally, there is little standardisation

in MRI quality assurance programs [110], increasing the likelihood of cross-site variation in PET quantification given clinical reliance on MRI-based corrections. It is clear that more work is to be done in this area, either through alteration of MRI sequences used to generate phantom attenuation maps, or through the development of phantoms from materials exhibiting properties that allow for their visualisation in MRI acquisitions.

### 3.3.3 Custom Designed Geometric Phantoms

The custom designs of geometric phantoms featured in this review are all borne from a requirement to test features for which no commercial option existed, often extending beyond performance testing of clinical PET/MRI scanners.

#### Rectangular Whole Body Phantom

Braun et al. [148] assessed the feasibility and performance of continuous table motion acquisitions in PET/MRI by developing a large Polypropylene (PP) rectangular phantom to approximate the dimensions of the human body, which was separated into cubic compartments. Each compartment had holes of varying size drilled into the sides to visually assess image quality and quantitatively assess resolution in both PET and MRI. The phantom was filled with a radiotracer solution. Whilst this phantom addressed the question it was designed for and was able to assess both PET and MRI performance [148, 149], it still suffered the same set-backs as commercially available phantoms and requires an external CT-based attenuation map to be used during PET reconstruction.

#### Phantoms to Study Motion Correction

In their assessment of motion correction methods, cylindrical acrylic phantoms filled with water and containing inserts featuring $^{22}$Na point sources were used by two groups [150, 151]. Given that a CT-based attenuation map was required for the reconstruction of PET data in order to account for the trolleys and bases used in these studies, the ability to generate an MRI-based attenuation map may have not been a design priority. However, in both cases motion correction was informed by MRI data and so MRI visibility of the phantom was crucial. Previously, a phantom made of PVA cryogel with radiotracer introduced during manufacture was demonstrated as a PET and MRI visible phantom able to undergo non-rigid movement [152].

### MRI Visible Polymers in Phantom Design

Rausch et al.[131] demonstrated the first PET/MRI phantom in-house-made with MRI visible housing. The cylindrical phantom had rod features on the bottom lid, whilst keeping the top section of the phantom homogenous. The phantom was filled with an aqueous solution of [$^{18}$F]FDG, sodium chloride and a gadolinium-based MRI contrast agent. They compared PET reconstructions of the phantom performed using no attenuation map, attenuation maps generated from the Siemens Biograph mMR DIXON sequences, an optimised phantom-specific MRI-based attenuation map and PET/CT images. Their work demonstrated that polymers are available for phantom construction that can be imaged by simultaneous PET/MRI, although the MRI-based attenuation map overestimated the phantom extent. Further work should be done to verify approaches for optimising MRI-based attenuation maps for phantoms using MRI visible polymers across different scanner models.

### Geometric Phantoms for Brain PET/MRI

Grant et al. [153] first demonstrated a 3D-printed geometric image quality phantom for performance testing the BrainPET (Siemens Healthcare) [53] MRI insert, for which the full characterisation is presented by Bieniosek et al. [154]. It was a cylindrical phantom with one empty quadrant containing plastic rods and three quadrants of solid polymer with cylindrical holes in a range of diameters. The empty spaces were then filled with a radiotracer solution. The group used the phantom for two further publications [155, 156]. The use of 3D printing in phantom development is increasing due to the widespread availability of 3D printers and low manufacturing costs [130], but the field lacks consistent assessment of the reproducibility in 3D printed phantoms. The publication of the phantoms design, manufacture and characteristics [154] facilitates the ability for other groups with 3D printing capabilities to produce and use this phantom in further work. Additionally, they validated the manufacture method through replication of a commercially available phantom and compared PET/CT acquisitions of the commercial and in-house printed phantoms [154], confirming its suitability for phantom manufacture. However, the phantom design does not address MRI visibility of the phantom housing and attenuation correction adequately.

Size appears to have been the driving factor for custom phantoms in brain PET. A cylindrical PMMA phantom with hollow rods and a Polytetrafluoroethylene (PTFE) insert was utilised to validate the use of an orbiting transmission point source for attenuation correction of PET data compared to that of an MRI-

based attenuation map [157]. The authors addressed the challenges in generating accurate MRI-based attenuation maps through implementation of a transmission source mechanism in generating attenuation maps for brain PET/MRI [157]. However, this was then used to replace the MRI based attenuation map entirely with one derived from the transmission source measurements, requiring the use of a specialised MRI coil that is applicable to head imaging only.

#### Geometric Phantoms in Radiosurgery Planning

Lim et al. [158] used two acrylic phantom designs in their study on the feasibility of using [$^{11}$C]Methionine PET in Gamma-Knife radiosurgery planning. This required phantoms that are suitable in validating multiple imaging modalities as they are introduced into the radiotherapy planning framework. These phantoms were imaged with CT, MRI and PET to assess geometric accuracy, image registration and quantitative PET within the Gamma-Knife radiosurgery planning system.

#### Summary of Geometric Phantom Designs

Each of these phantoms is used at one site and designed to address specific research questions, with only one fully presented and characterised to promote its use by other institutions. Characterisation of materials and methods presents a barrier to widespread adoption of in-house manufacture methods such as 3D printing [130], as each group must then perform these measurements. The design and verification of a phantom requires a significant time commitment, and so distribution of this information is valuable to the imaging community to accelerate phantom development. Most recently, an MRI visible polymer has been demonstrated as suitable for PET/MRI use [131], providing a potential solution to MRI-based attenuation correction issues in phantom studies.

## 3.4 Anthropomorphic Phantoms

A total of 20 anthropomorphic and tissue equivalent phantoms were identified in this review, of which 16 are custom designed or in-house manufactured. These phantoms cover 5 areas of human anatomy, as displayed in figure 3.5, with a final category describing phantoms that contain materials equivalent to specific human tissues but do not represent any specific anatomy.

Head and Brain phantoms are the most published category of anatomical phantoms at 16 publications. This reflects the commonly desired clinical PET/MRI

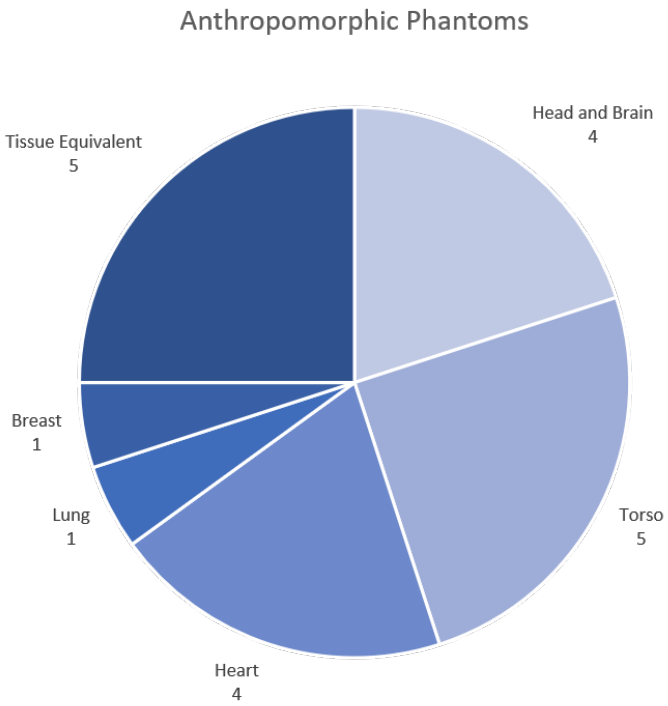


**Figure 3.5**: Anthropomorphic PET/MRI phantoms categorised by the area of human anatomy they represent

application of neurology and the subsequent areas of research addressing attenuation correction in brain imaging [159]. Correcting for bulk and physiological motion are also an important area of interest, the mechanisms of which are beyond the scope of this review, but are presented by Polycarpou et al. in their recent review [41](in press). Physiological motion in particular requires the use of phantoms able to replicate the anatomical geometries and motion required. Again, this is reflected in the phantoms designed and their publications with 7 torso and cardiac phantoms used across 14 publications.

### 3.4.1 Commercially Available Anthropomorphic Phantoms

As with geometric phantoms, the commercially available options utilised for PET/MRI are phantoms originally designed for Nuclear Medicine and PET. These phantoms are well established within the field due to the necessity of administering a radioactive tracer for PET and $\gamma$-camera imaging limiting the recruitment of volunteers for investigative work. By comparison, MRI phantoms often focus on quantitative performance through simple geometries [160], although some anthropomorphic MRI phantoms are commercially available and tissue equivalent mate-

rials are in use throughout the MRI community [109].

### Hoffman Phantom

The Hoffman brain phantom [117] (Data Spectrum Corporation) is one of the most popular anthropomorphic phantom featured in 7 publications identified by this review. It is a PMMA cylinder containing 19 composite polycarbonate plate inserts which, when filled with fluid, simulate normal [$^{18}$F]FDG radiotracer distribution in the brain and a realistic MRI proton density distribution. Optional inserts are also available to simulate defects. The Hoffman phantom has been used to assess the performance of PET inserts in clinical MRI scanners [161–163], evaluate motion correction methods [164, 165], the demonstrate of PET image reconstruction methods [166] and MRI-based attenuation correction [167] methods. This is the only commercially available phantom identified within this review that is also advertised for MRI use, although the polycarbonate plates are not visible in MRI. The design lacks a skull component for a realistic attenuation profile, it does not replicate brain tissue relaxation properties in MRI and the cylindrical design does not conform to human head geometry, which are major limitations for it's use as a human head surrogate in PET/MRI.

### Torso Phantoms

Two commercially available phantoms of the Thorax were used: the elliptical Lung-Spine [168] and Anthropomorphic Torso Phantom [169]. Both phantoms are licensed by Data Spectrum Corporation and are constructed from PMMA with polystyrene-filled lung inserts, solid PTFE spine insert and an optional PMMA cardiac insert modelled on the left ventricle and myocardium. The Anthropomorphic Torso phantom also features a liver insert. The phantom body, cardiac and liver inserts are then filled with radiotracer solution. A PU cardiac insert (Radiology Support Services) representing two cardiac chambers and the myocardium was used independently in one study [170].

### Commercially Available Anthropomorphic Phantom Summary

All of the commercially available anthropomorphic phantoms are constructed from PMMA or PU, and so any solid material is not MRI visible. Despite the concerns raised around MRI-based attenuation correction in geometric phantoms, many studies use MRI-based attenuation maps to reconstruct PET data for these anthropomorphic phantoms, including two studies actively using these phantoms to assess the impact of using MRI-based attenuation correction[167, 169]. This

may be because the differences between MRI-based and CT-based attenuation correction in PET quantification still need to be quantified prior to clinical use, or because MRI-based attenuation methods based on tissue segmentation from anatomical maps [171] are more easily applied to anthropomorphic phantoms than non-anatomical shapes.

The current commercially available phantoms are only able to assess brain and cardiac protocols. This excludes some key applications of interest in clinical PET/MRI, such as [$^{68}$Ga]-PSMA imaging in prostate cancer patients [172]. Crucially, no commercially available anthropomorphic phantoms are able to accurately represent human tissue in both PET and MRI.

### 3.4.2 Custom Anthropomorphic Phantoms

Whilst an accurate representation of anatomical geometry is a key aspect of design across all anthropomorphic phantoms, many in-house manufactured phantoms identified in this review take additional steps to achieve both PET and MRI tissue equivalence, or mimic additional physiological properties.

#### Head and Brain Phantoms

Three human head phantoms were developed between 2011 and 2021. The first of these was the Iida Brain phantom [118], initially developed for use in PET and Single-Photon Emission Computed Tomography (SPECT) imaging, it is designed to represent a realistic human head contour and include a cavity around the brain material filled with dipotassium phosphate to simulate the skull. Both of these features address some of the limitations presented by the Hoffman phantom in brain imaging. The phantom was manufactured through 3D printing, for which Iida et al. [118] demonstrated a high degree of reproducibility. The Iida phantom has been assessed for PET/MRI use, with Johansson et al. [173] providing a description of potential applications, highlighting the issues around a lack of white matter radiotracer distribution and difficulties with MRI-based attenuation correction when scanned with the Phillips Ingenuity PET/MRI scanner, but ultimately concluding it to be a useful test object. The Turku PET Centre group later used the phantom in three additional PET/MRI publications [128, 167, 174] including an international multi-centre study.

Harries et al. [120] presented their solution for a human head phantom with a focus on mimicking both MRI and PET tissue properties. The authors detailed the relevant properties of their chosen materials as well as the limitations in the design and manufacture of this phantom. In particular, the design did not mimic the

structures of grey and white matter in the brain, so whilst the feasibility of manufacturing such a phantom and its compatibility with MRI-based attenuation methods was demonstrated, applications may be limited due to the reduced detail in brain structure compared to the Iida and Hoffman brain phantoms. Additionally, this phantom necessitates in-house manufacture due to the use of short shelf-life materials such as agar. As a result, a centre reproducing this phantom should still perform validation measurements to ensure the desired material properties and geometries have been achieved. Finally, Okazawa et al. [119] used a human skull filled with saline-soaked cotton and radiotracer filled rubber tubes to represent arteries. This phantom was specifically designed to address the authors research question regarding the reliability of quantitative [$^{15}$O] imaging in the carotid arteries using PET/MRI.

#### Torso Phantoms

Larger phantoms representing the pelvis [121] [136] and torso [8] have also been designed and used within PET/MRI. These phantoms feature multiple organs with differing tissue properties and radiotracer uptake, and so 3D printing was utilised to enable the individual design of each component. Currently, the printable materials commonly available to sites without an extensive manufacturing department are limited in the tissue-equivalent properties they can display [112, 130]. As a result, groups developing these phantoms often opted to either 3D-print an outer shell of the organ of interest which may be filled with an appropriate tissue-equivalent material, or use a 3D-printed mould to cast a model using a gel or wax.

The ADAM PETer pelvis phantom [121] was designed for applications regarding the use of multimodal imaging in radiotherapy. It was based on the ADAM-pelvis phantom [175], by further developing the model to be compatible with PET imaging in addition to CT and MRI with the aim to utilize the phantom in the optimisation of PET/MRI guided radiotherapy for prostate cancer patients [121]. The ADAM PETer also introduced 3D printing into the phantoms manufacture to improve the modular design. The phantom featured a large number of materials to simulate various tissues, which were extensively described along with the phantoms lengthy assembly process. However, the authors reported that due to a modular design, switching out of organs of interest was less laborious once the phantom was constructed and so allowed customisation of the phantom for several clinical scenarios [121]. Further work validating the reproducibility of 3D printing organ modules for this phantom would facilitate its use external to the home institution.

Another pelvis phantom [136] consisting of a PMMA container filled with a radiotracer solution has also been tested. It was noted that the phantom is described in other works excluded by the review criteria [176, 177] as featuring multiple organ inserts, however these features were not highlighted in any of the PET/MRI work.

The Wilhelm Anthropomorphic Torso Phantom [8] has been developed by the European Institute of Molecular Imaging as a phantom for PET, CT and MRI capable of replicating cardiac and lung motion. Bolwin et al. [8] described the design, manufacture and characterisation extensively, however this phantom has been used by the institute in several works addressing motion correction in PET/MRI since 2011 [178–181]. Wilhelm features inflatable silicone lung inserts and a silicone cardiac insert. Both sets of inserts are piston driven to induce motion. A double silicone membrane is used for the cardiac insert to create an outer layer that can be filled to represent the myocardium, a schematic for which is shown in figure 3.6. Lung inflation is controlled from the base of the lungs by a rubber membrane to simulate the diaphragm. A liver compartment is also included. The phantom could be customised by the choice of fluid filling for each compartment and additional wax spheres mounted within the phantom as lesions. Models of the heart and lungs were 3D printed to create moulds on which to shape the silicone. No skeletal structure was featured in the phantoms' design which may limit its application in other areas of interest such as MRI-based attenuation correction.

Motion correction is an on-going area of research with different methods appropriate to assess different types of motion [41]. As such, the Wilhelm phantom occupies a niche the needs of which have not been met by commercial vendors. However, this phantom is highly complex, having been developed over many years [8], with a multitude of materials and manufacture methods required for its construction.

### Cardiac and Lung Phantoms

Inflatable double-membrane cardiac phantoms of a reduced complexity have also been demonstrated as suitable for motion correction applications in PET/MRI [9, 10]. These phantoms focussed exclusively on cardiac motion, placing one balloon inside another, filling the interspace with a mix of radiotracer, gadolinium-based contrast agents and gelling agent to represent the myocardium. This was then suspended within a second radiotracer gel mix to simulate a soft tissue background. Similarly, a single membrane balloon has been used to simulate respiratory motion [123, 124]. The materials in these phantoms are more widely accessible to sites without the large time, cost and facilities to create a phantom as complex

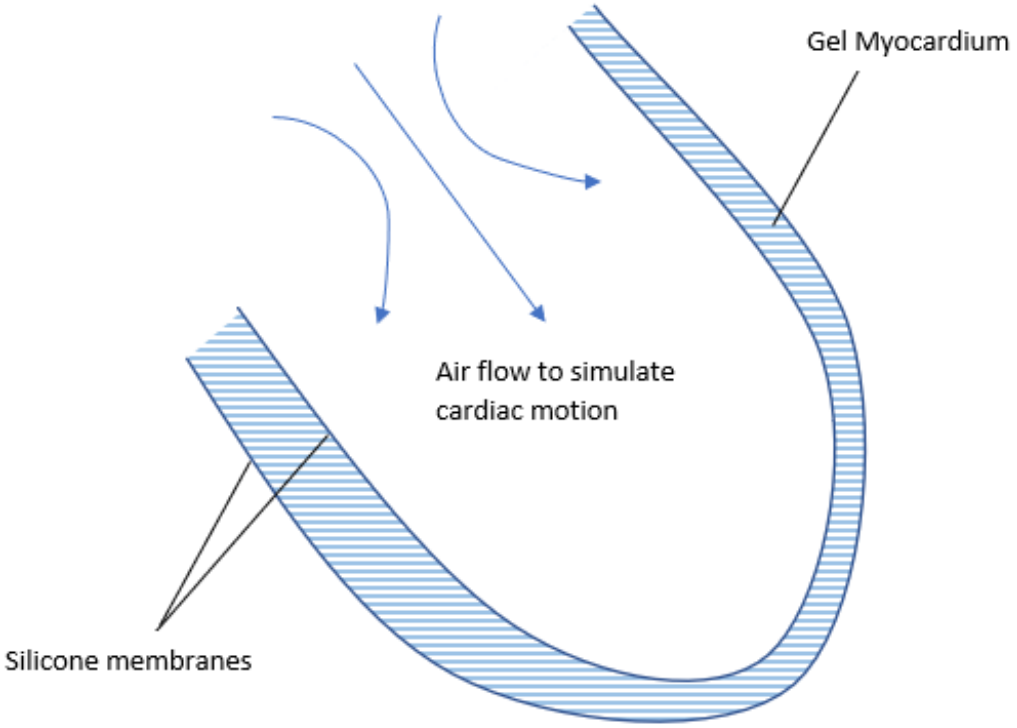


**Figure 3.6**: A schematic demonstrating the general design concepts of phantoms to simulate cardiac motion, as used by [8–10].

as the Wilhelm phantom. However, these phantoms were not described as extensively and are less representative of the clinical scenario both anatomically and in terms of physiological motion.

In myocardial perfusion, O'Doherty et al. [182] used a different phantom, initially designed and described as an MRI phantom [183], to demonstrate the feasibility of first pass myocardial perfusion imaging in PET/MRI. The phantom featured four chambers simulating the atria and ventricles of the heart, with two cylindrical compartments each side representing the myocardium. Tubes representing veins and arteries have been arranged such that the flow of fluid through the phantom simulates entry to the heart from the vena cava. Water is delivered to the phantom from an external pump and control unit. The phantom was demonstrated as suitable for PET/MRI, however the lack of tissue equivalent materials and true anthropomorphism may impact how applicable any results are to clinical imaging. Matusiak [184] presented a Multimodal Heart Phantom (MHP) constructed of PMMA featuring two chambers to simulate left and right ventricles and a surrounding space to simulate the myocardium. The imaging compatibility

of the phantom across SPECT, PET, CT and MRI was demonstrated through visual assessment and image registration between the imaging modalities [184], but no quantitative data were presented.

### Breast Phantom

A modular breast phantom was presented by Aklan et al. [185]. Breast imaging in MRI uses specialised RF coils for which anthropomorphic phantoms are not typically available. The modular breast phantom consisted of two PMMA domes with optional MRI and PET/MRI inserts. The PET/MRI insert features four sizes of glass sphere to be filled with radiotracer solution assembled onto a cross structure that is MRI visible [185]. This phantom was more of a hybrid between the anthropomorphic and geometric phantoms, as the insert features are more representative of those expected in a quality assurance phantom and when filled with water does not replicate the tissue composition of the breast. However, the design has been well described and offers a solution to performance testing and validation of equipment and protocols for breast imaging in PET/MRI, for which the only alternative demonstrated has been uniform bottle phantoms [137].

### Summary of Anthropomorphic Phantom Designs

The in-house manufacture of anthropomorphic phantom featured in this review have demonstrated numerous benefits. One is the relatively low cost of producing phantoms where manufacturing techniques such as 3D-printing [130] and casting from moulds are used. The other is that increasingly complex phantoms can be developed to address specific needs within the field of medical imaging, as with the Wilhelm phantom [8] and ADAM PETer [121]. The ability to customise these phantoms to simulate multiple clinical scenarios also makes the designs appealing, and may lead to validation for patient specific anatomy as seen developing in other modalities[186]. Use of materials able to display similar PET and MRI properties to human tissues promotes the testing of clinical protocols as would be applied to patients, and by extension greater compatibility with systems such as radiotherapy treatment planning or dosimetry software.

The anthropomorphic phantoms presented also demonstrate applications where representation of anatomical geometry is important for a given application even where tissue equivalence may not be achieved. For example, breast phantoms or brain phantoms are useful in the testing and validation of scanner hardware specifically designed for this anatomy [167, 173, 185]. They are also useful in the demonstration of clinical applications which rely more on visual assessment or

organ segmentation, such as in PET and SPECT myocardial perfusion imaging [182].

Conversely, the development, manufacture and characterisation of such phantoms can present a significant time commitment and an initial investment cost for sites without existing manufacture facilities. Even well characterised materials such as agar introduce additional uncertainties to the phantoms properties as they have to be remade for each experiment. Across the literature in this review, description of phantom designs, the material properties assessed, and detail of results presented varies.

Further work is required in this area to increase the utilisation of anthropomorphic phantoms in PET/MRI. The Iida phantom is the only design that appears to have been utilised by multiple institutions [128], but have not demonstrated an adequate level of reproducibility. Significant investment is made into developing and characterising tissue equivalent materials, yet the majority of these designs are housed in a PMMA or PU casing, both of which are not visible in MRI and could affect quantitative PET data when MRI-based attenuation correction is used.

## 3.5 Discussion

This review has presented an overview of the phantoms used and developed by institutions for PET/MRI during the period 2011-2021. These range from simple containers filled with a uniform fluid to large anthropomorphic phantoms simulating human anatomy and physiology. Commercially available phantoms remain the dominant test objects in performance evaluation of PET/MRI systems, and solutions have been proposed to facilitate their continued use by improving MRI visibility [145, 147].

In-house design and manufacture is a more popular choice for producing anthropomorphic phantoms, as they are often designed with specific clinical scenarios or research questions in mind. Consequently, a wide range of materials, designs and manufacture methods are presented. The characterisation and publication of radiological materials for phantom construction and their comparison to human tissue properties is increasing which, alongside the rise in adoption of 3D printing, facilitates the more widespread use of tissue equivalent materials [130]. Through continued assessment of these properties and the uncertainties in manufacture methods, PET/MRI phantoms can move towards adopting standardised approaches suitable for quantitative imaging assessment and cross-site comparisons.

PET/MRI phantom development would benefit from an increase in options

available from the commercial sector and professional bodies pushing for improved solutions for multimodal imaging systems. Of the designs presented in this review, only custom designed phantoms begin to address the question of creating phantoms exhibiting suitable radiological properties for acquiring quantitative data in both PET and MRI. This restricts not only the dissemination of available phantoms, but also the standardisation of clinical procedures and validation related software where these phantoms have been used. The impact of this is that patient imaging is then not necessarily comparable across institutions, with particular concern if patients move across different sites during periods of monitoring reliant on quantitative PET/MRI to inform their clinical pathway.

Applying MRI-based attenuation and scatter correction to phantoms remains challenging. No commercially available phantoms exist that exhibit radiological properties suitable for both PET and MRI, either as quality assurance test objects or anthropomorphic phantoms. PMMA remains the preferred choice for constructing phantoms, but is not MRI visible and is often either omitted from or incorrectly classified in MRI-derived attenuation maps. Polymers available for 3D printing may offer some solution to this, with MRI visible options available. Commercial vendors are key stakeholders in PET/MRI phantom development, offering standardised manufacture, material properties and rigorous quality control to their products. As PET/MRI enters routine clinical use, covering a wider variety of applications, it can only be expected that the necessity for studies performed using widely available, reproducible phantoms increases.

## 3.6 Conclusion

Several commercially available phantoms have been demonstrated as appropriate for limited use in PET/MRI studies, although no vendor has yet released a phantom specifically designed and optimised for both, let alone simultaneous, PET and MRI acquisitions. The development of anthropomorphic phantoms and tissue equivalent materials for PET/MRI has been an active field over the past decade, with an increasing focus toward material characterisation and reproducible manufacture. Further work is required to develop phantoms suitable for holistic performance evaluation of PET/MRI scanners, and in establishing robust manufacture techniques accounting for variation in tissue equivalent materials for improved anthropomorphic phantoms.

# Chapter 4

# Exploration of Resolution Effects in PET with Multi-modal Phantoms.

## 4.1 Introduction

The literature review turned up a number of options for physical PET/MR phantoms, however it also highlighted the difficulties in replicating tissue properties in both PET and MRI. Physical phantom acquisitions remain an important mechanism in benchmarking the performance of a clinical scanner. PET scanners are also calibrated against physical phantoms for quantitation of tracer uptake. For the GE SIGNA PET/MR (GE Healthcare), the scanner is calibrated to a flood phantom with attenuation correction provide by means of a manufacturer supplied correction map registered to the phantom emission tomogram, rather than use of an MR derived attenuation map.

The impact of partial volume effect on PET images [44], and the difficulties of attenuation correcting images in materials and tissues without an MR signal [59] has already been reported on in earlier studies, as described in Chapter 2. However, it was necessary to investigate these effects in the SIGNA PET/MR scanner, and benchmark the performance of both the scanner and most up-to-date PET image reconstruction algorithms. This was achieved through phantom experiments conducted with a geometric phantom and an anatomical phantom.

The aim of these experiments was to assess any partial volume effects arising in measuring structures of a size similar to the spinal cord diameter in PET images at the current performance of the SIGNA PET/MR scanner (GE HealthCare) when using existing MR derived attenuation correction and standard image reconstruc-

tion methods as are used in phantom and clinical scanning. Contrast recovery is also assessed to see how quantification may be affected by partial volume affects and the use of MR derived attenuation maps. A tertiary aim was to determine whether a physical phantom with the tissue surrogates used in this model would be appropriate for this project into spinal cord PET/MRI.

## 4.2 Methods

The NEMA IEC PET Body phantom [105] is recommended as part of the protocol for assessing scanner performance and image quality in clinical PET systems, as described in the previous chapter [31]. Typically a line source is used to assess resolution and point spread function (PSF), however the spheres of the IEC body phantom are of comparable diameter to the spinal cord. The drawback to this is that the partial volume effect is a 3-dimensional effect, and a line source will not experience contribution to the PVE from the axial direction as a spherical or point source does.


**Figure 4.1**: Images of the NEMA IEC PET Body phantom, showing spherical fillable inserts at the top and a central column filled with polystyrene. Images courtesy of Data Spectrum.

A custom phantom designed by collaborators at the University of Leeds [187, 188] and manufactured by Leeds Test Objects Ltd is also used in this study. This phantom was constructed for applications in Radiotherapy planning using MR systems, and was designed to replicate the head, neck and shoulders. It is a 3D printed phantom with an external PMMA shell, 41cm in length from the top of the head to the base and 51cm wide at the widest point of the shoulders. It contains a brain surrogate material made from a 10% Polyvinyl Acetate (PVA-c) solution, an air-filled lung and trachea insert, and a bone surrogate material 3D printed using a ceramic resin. This allows the phantom to replicate these tissue types in CT and MR acquisitions [187], with the PVA-c solution exhibiting a T1 relaxation

time of 1387ms and a T2 relaxation time of 139ms. There is a small hole of 2mm diameter at the top of the head for insertion of a radiation dosimeter. An image of the phantom is displayed in figure 4.2 part A.

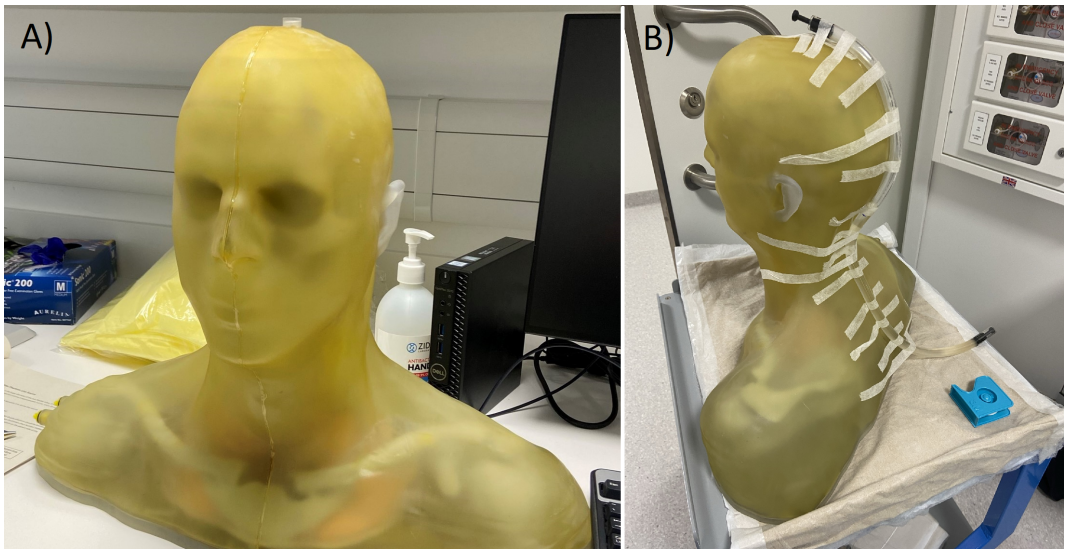


**Figure 4.2**: A) The anthropomorphic Head and Neck Phantom for MRI/Radiotherapy planning and B) modified to attach a tube to simulate spinal cord radiotracer uptake.

The SIGNA PET/MR Scanner (GE Healthcare) used in this thesis features a 3T MR scanner with a TOF-PET scanner located within the bore. The PET scanner features LYSO crystal detectors backed by silicon photomultipliers It has an axial field of view (FOV) of 50cm for the MR component and 25cm for the PET scanner [189]. Image reconstruction is performed either on the scanner workstation with dedicated reconstruction software, or may be performed offline using GE Healthcare reconstruction software. The use of silicon photo-multipliers permits a high detector timing resolution and enables these systems to have TOF capability.

### 4.2.1 IEC NEMA Phantom Acquisition

All acquisitions were performed on the GE HealthCare SIGNA PET/MR scanner at the University of Sheffield MRI unit at the Royal Hallamshire Hospital. The NEMA IEC Body phantom was set up according to the NEMA NU2 standard for performance measurements of PET scanners (2018) [190]. The phantom was filled with a total of 75.6MBq of [$^{18}$F]FDG PET tracer in the main phantom body and more concentrated activity in some of the spherical inserts. Activity was distributed such that the main body of the phantom has a radioactivity concentration of 5.3kBq/ml at the time of scanning, and the ratio of activity in the 'hot' spherical

inserts to the main phantom body is 4:1. The smallest four spheres were filled with activity ('hot' sphere) whilst the two larger spheres were filled with water ('cold' spheres). Acquisitions were performed for 5 minutes, with and without MR 'pulsing' running simultaneously. Finally, a longer acquisition was performed for 20 minutes.

Images were reconstructed using Time of Flight Ordered Subset Expectation Maximisation (TOF-OSEM) (2 subsets, 28 iterations) with a 5mm Gaussian filter applied post-reconstruction in the transaxial plane and a [1 4 1] axial convolution filter for de-noising. Data was also reconstructed using the TOF Q.Clear (beta = 350) algorithm, which includes PSF correction. Both images were reconstructed using attenuation correction derived from a DIXON MRI sequence (known as MR Attenuation Correction or MRAC).

### Analysis

Spherical regions of interest (ROIs) were drawn in each sphere using regions set to the true sphere diameter centred over the matching sphere insert in the PET images. As the sphere diameter is known for the phantom, this assessed how well the PET images of the phantom conform to the it's physical parameters. Background radioactivity concentration was measured as an average over 8 spherical ROIs of 40mm diameter placed in the main body of the phantom where no other PET features are present. Contrast Recovery Coefficient (CRC) was calculated as

$$CRC = \frac{\frac{C_H}{C_B} - 1}{\frac{a_H}{a_B} - 1} \times 100 \tag{4.1}$$

where $C_H$ and $C_B$ are activity concentration (kBq/ml) in the hot sphere and background respectively and $a_H$ and $a_B$ are activity in the hot sphere and background. A contrast recovery of 100% indicates fully recovered contrast that reflects administered activity.

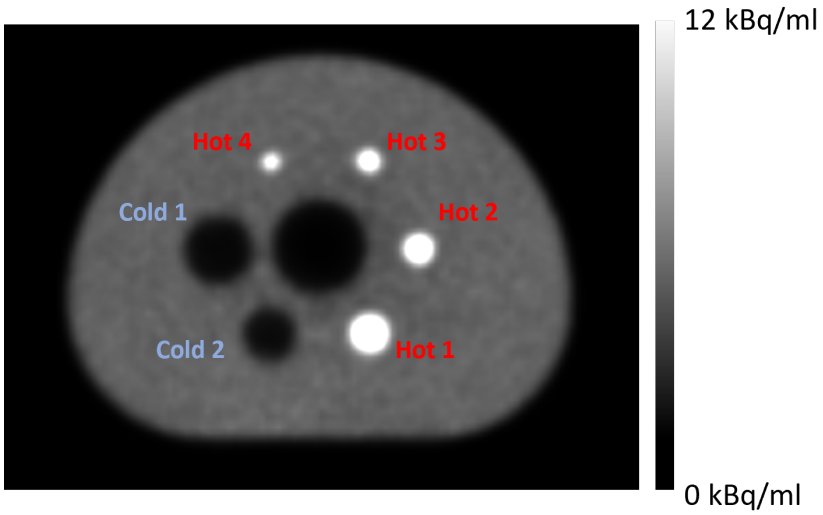


**Figure 4.3**: An example of how spheres are identified in the results section. Spheres are labelled "cold" for spheres filled with water and "hot" for spheres filled with [$^{18}$F]FDG solution.

Line profiles were drawn across the spheres in 3 perpendicular directions along each scanner axis and analysed to obtain full width half maxima (FWHM) in 3D Slicer. These were averaged for each sphere in each reconstruction to give the size of the sphere in each image.

### 4.2.2 Head and Neck Phantom Acquisition

A protocol for the Head and Neck phantom was developed in collaboration with colleagues at University of Sheffield, Sheffield Teaching Hospitals NHS Foundation Trust, University of Leeds and with input from industrial partners at GE. As the phantom does not have a spinal cord insert, a rubber tube of 10mm diameter was attached to the outside of the phantom to allow some assessment comparable to physical dimensions of the spinal cord. It was attached along the back of the phantom to be as close as possible to the spine and bone surrogate material. The head insert was also used to place a radioactive source into the brain region. The phantom set up used in the experiment is shown in figure 4.2.

It was initially planned to fill the main body of the phantom with an [$^{18}$F]FDG and Gadolinium contrast solution to act as the background tissue activity and bring the T2 relaxation time of the fluid more in line with values for muscle. However, the phantom had some small leaks and so it was decided to proceed with the phantom filled with water and only fill the head insert and spinal cord tube with radiotracer.

| MRI Sequence | TE | TR | Matrix Size | Slice Thickness |
|---|---|---|---|---|
| Sagittal T1 FSE | 20ms | 600ms | 320x320 | 3mm |
| Sagittal T2 FSE | 101ms | 2200ms | 320x320 | 3mm |
| Proton Density | 31ms | 2500ms | 384x384 | 3mm |
| Axial T2 Cube | 105ms | 3000ms | 512x512 | 5mm |

**Table 4.1**: MRI sequence parameters used to image the Head and Neck Phantom, where TE is Echo Time, TR is Repetition Time, Bw/Px is Bandwidth per Pixel and NEX is Number of Signal Averages.

The tube acting as the spinal cord surrogate was cut to 50cm and capped at one end. A mix of 8.9MBq [$^{18}$F]FDG radiotracer, 1.4g agar and 4.6g gelatin was prepared with hot water up to a total volume of 50ml. These values were approximated from Blechinger et al. [191] to give a T2 relaxation time of 80ms. The tube was filled with 28ml of the solution to give 5MBq activity. The open end of the tube was then capped and the gel was left to set for 30 minutes. A gel was used to ensure the activity distribution remained in place and retained its shape, to prevent leakage during scanning, and to allow for imaging that would replicate tissue in MRI. A syringe cap was used to create a point source of 6.2MBq [$^{18}$F]FDG, this was sealed and then secured in the head cavity. At the time of scanning the total activity in the phantom was 8.5MBq.

On the scanner bed, the phantom was positioned in a 16 channel head and neck coil. Three PET acquisitions were performed. An initial PET bed position to acquire data of the head of the phantom was conducted for 5 minutes to check positioning, a bed position over the neck and shoulders for 30 minutes, and a second acquisition of the head was then performed for 30 minutes. PET data was acquired in list mode to enable offline reconstruction.

PET images were reconstructed on the scanner using a Time-of-flight Ordered Subset Expectation Maximum (TOF-OSEM) algorithm with point spread function (PSF) modelling with 2 iterations and 28 subsets. Images were reconstructed with attenuation correction derived from a Dixon MR sequence, with the Dixon MR images shown in figure 4.4. All data was exported from the scanners and stored on an XNAT database to access for offline processing. This data consists of compressed List Mode (LM) files (BLF), compressed Histogram DICOM (RPDC) with HDF5 files, PIFA files, reconstructed DICOM images and MRI pfiles.

### Analysis

Line profiles were drawn at each vertebral level from C1 to T3 to acquire the FWHM of the spinal cord tube at that position in both PET and MR acquisi-

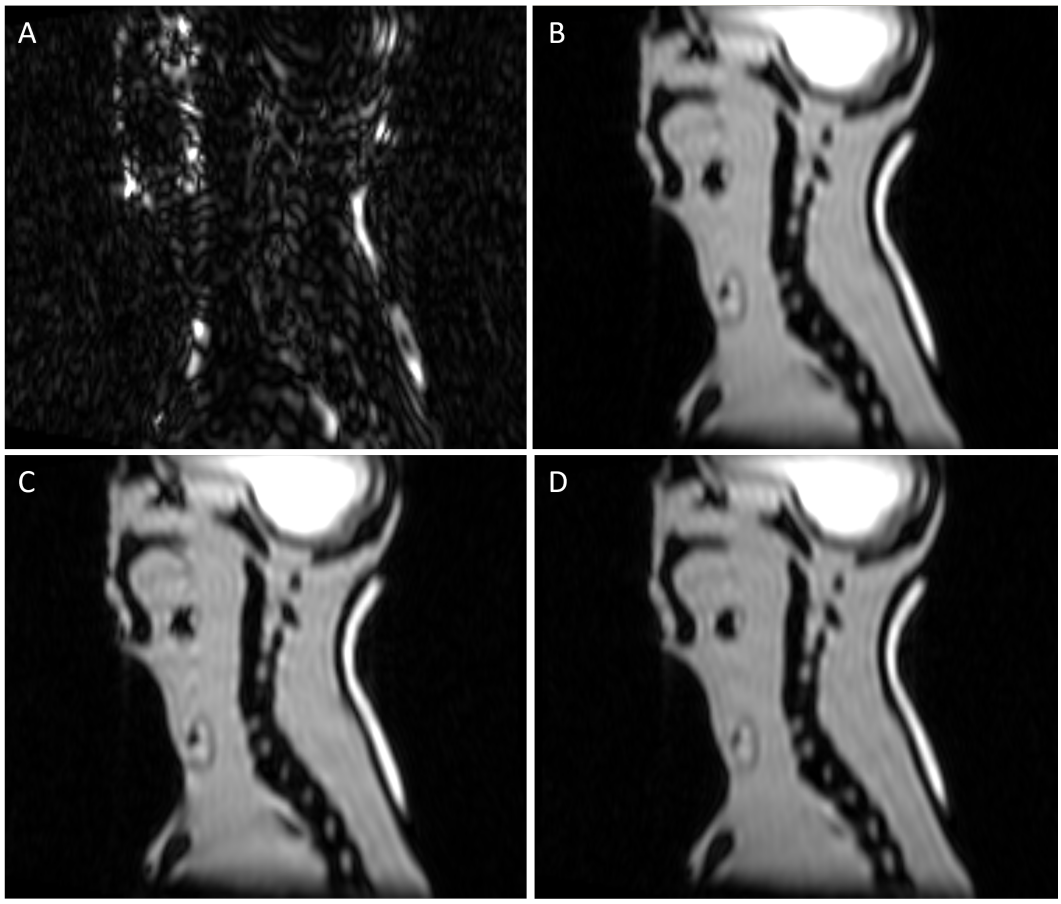


**Figure 4.4**: Example slices of images from the Dixon MRI sequence used to derive attenuation maps, showing the A) water, B) fat, c) In Phase and D) Out of Phase spectroscopic images.

tions. Radioactivity concentration was also measured to compare to administered radioactivity concentration. This is presented as a ratio of measured radioactivity concentration to administered radioactivity concentration, where a ratio of 1 indicates that measured radioactivity concentration accurately reflects the administered tracer radioactivity concentration.

## 4.3 Results

### 4.3.1 IEC NEMA Phantom

Images of the NEMA phantom are displayed in figure 4.5. Measured radioactivity concentration and CRC is higher in images reconstructed with the Q.Clear algorithm, as shown in figure 4.6 and 4.7 respectively. In all cases, measured radioactivity concentration and CRC also increase with the size of the sphere,

particularly for the [$^{18}$F]FDG filled spheres. Average background measured was consistent between PET reconstructions (range: 5.47 - 5.77kBq/ml) and close to the true background radioactivity concentration of 5.3kBq/ml. For a true activity ratio of 4:1, the spheres should measure around 21.2kBq/ml, however all of the active spherical inserts are underestimated in radioactivity concentration measurements. The smallest spheres show the lowest measured radioactivity concentration.

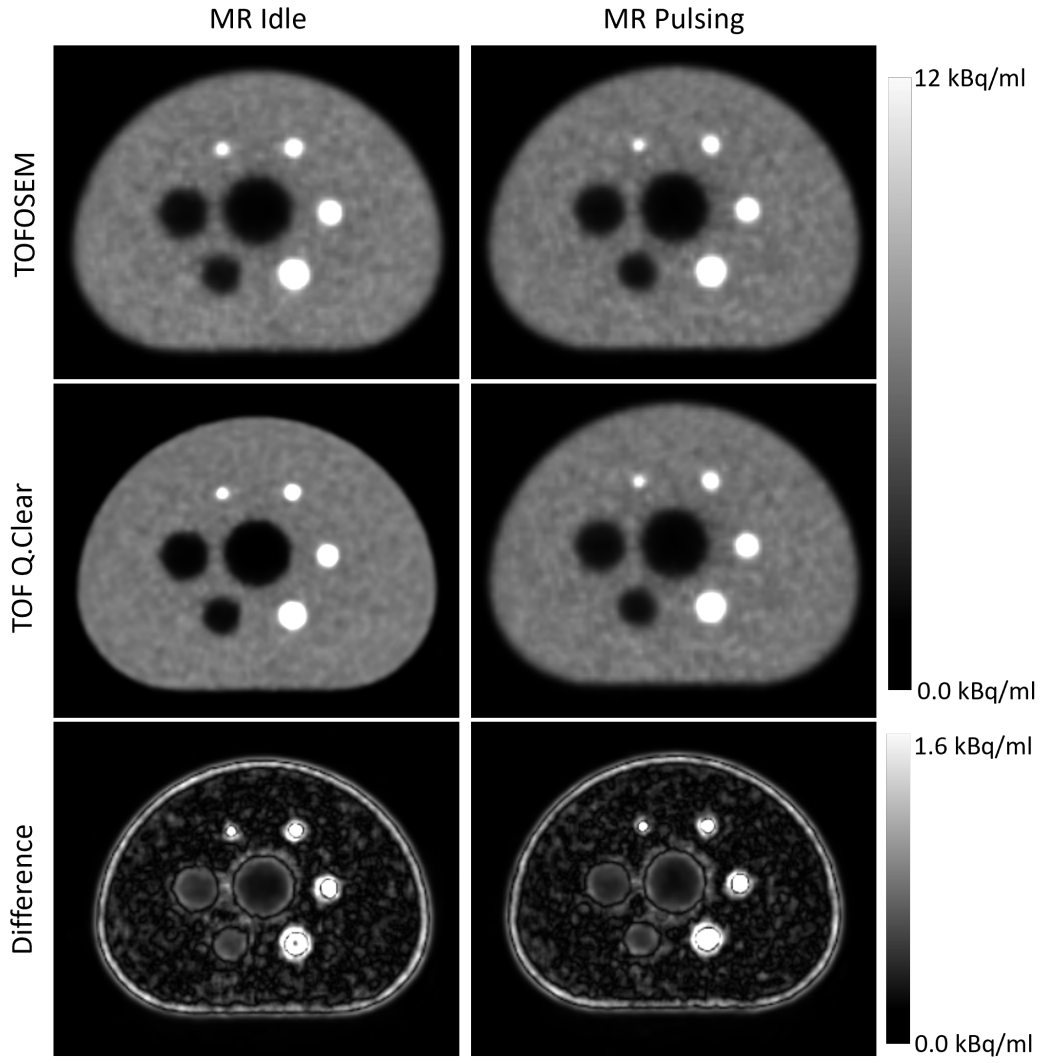


**Figure 4.5**: Reconstructed PET images of the NEMA IEC Body Phantom with TOFOSEM and TOF Q.Clear algorithms, acquired with MR idle and MR pulsing on the PET/MR scanner. The difference image shows the absolute image when the TOFOSEM image is subtracted from the Q.Clear image.

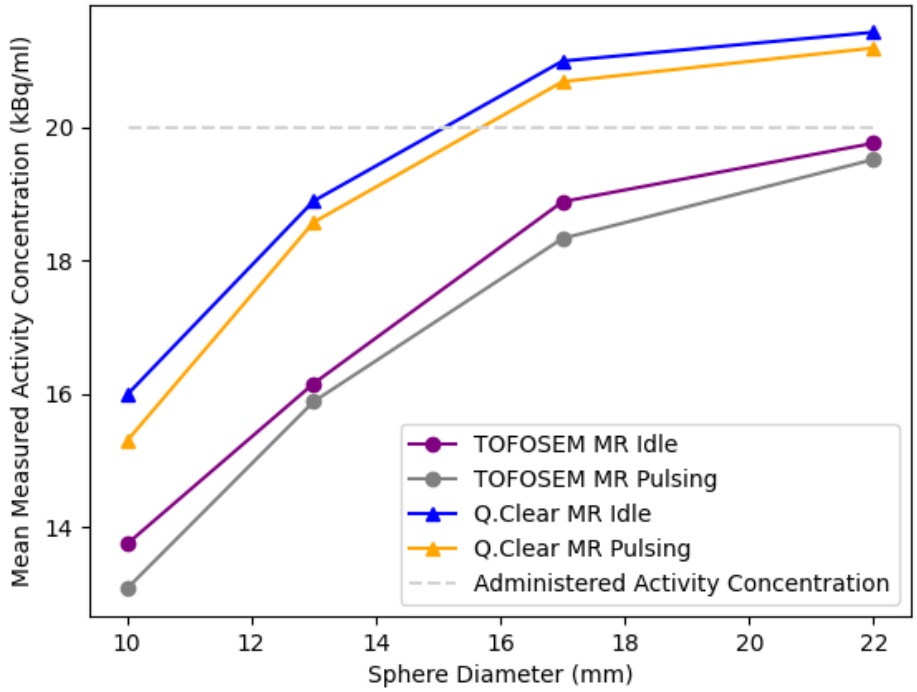


**Figure 4.6**: A plot showing measured activity plot against the diameter of the spherical inserts for [$^{18}$F]FDG filled spheres for the NEMA IEC Body Phantom.

This is also reflected in the CRC, shown in figure 4.7, where a maximum of 59.4% contrast recovery is achieved for the 10mm sphere, despite Q.Clear images showing contrast recovery of over 80% in spheres greater than 17mm diameter. Cold spheres show a "spill in" effect, reading up to 1.4kBq/ml despite containing no radiotracer, as shown in figure 4.8.

Measured FWHM of line profiles across the spherical inserts shows that sphere size is also underestimated in the [$^{18}$F]FDG filled spheres, as shown in figure 4.9, with the FWHM measuring 2-3.6mm smaller than the actual sphere size for the 22mm,17mm,13mm spheres and 1.3-2.7mm smaller for the 10mm sphere.

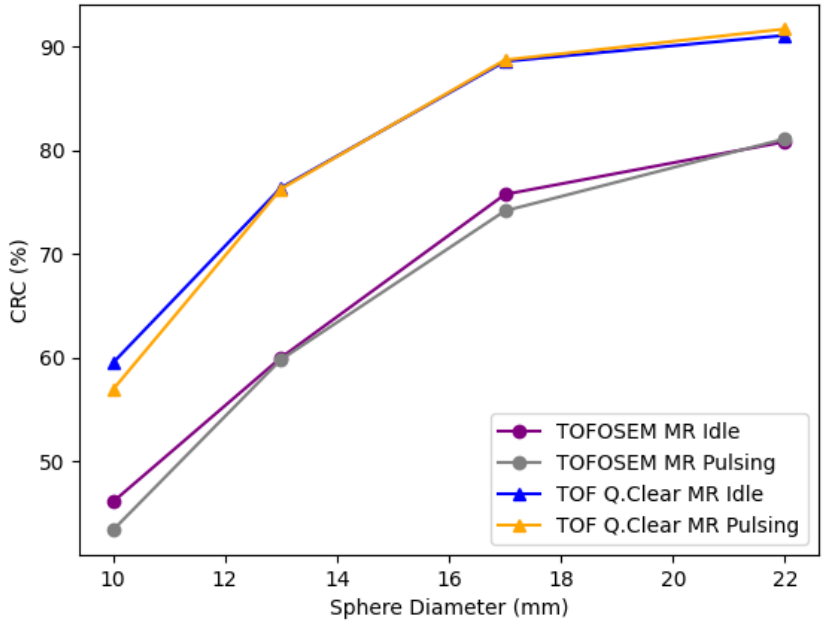


**Figure 4.7**: A plot showing contrast Recovery Coefficient (CRC) plot against the diameter of the [$^{18}$F]FDG filled spheres for the NEMA IEC Body Phantom.

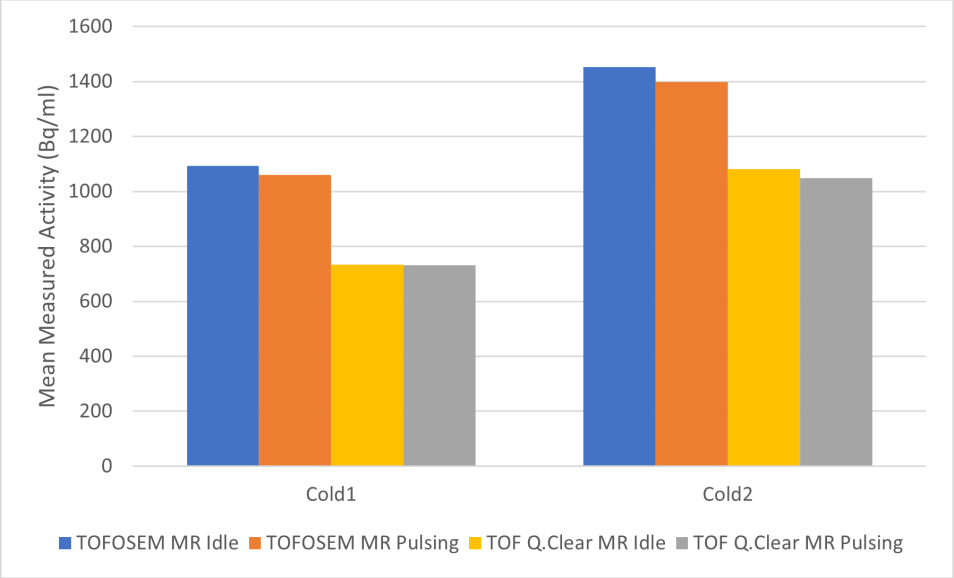


**Figure 4.8**: A graph displaying mean activity concentration in the spheres filled with water only, so contain no administered activity.

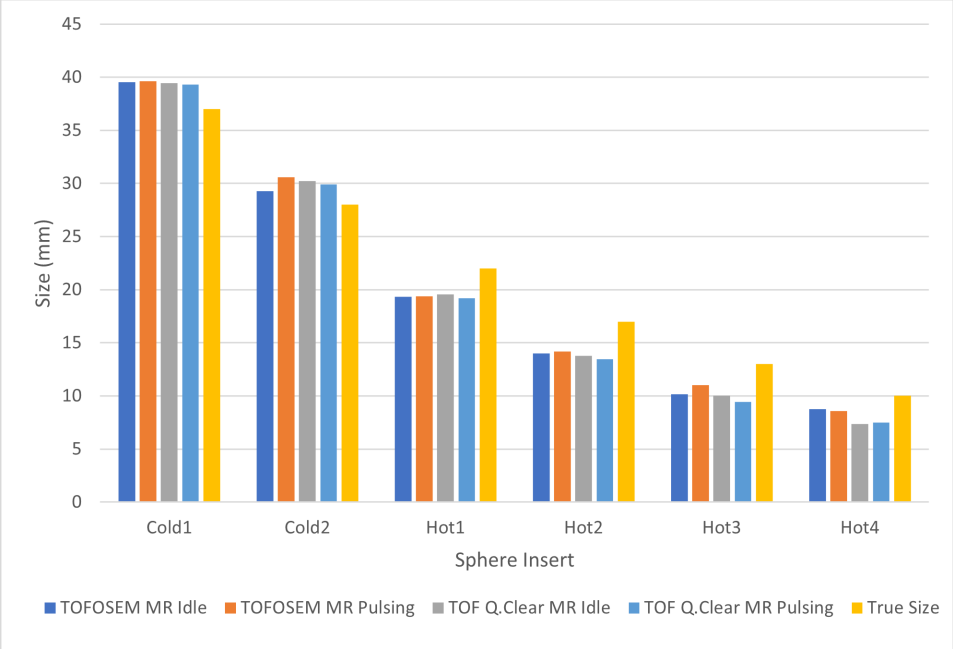


**Figure 4.9**: A graph displaying measured size of spherical insert for the NEMA IEC Body Phantom for different PET reconstruction algorithms.

### 4.3.2 Head and Neck Phantom

Activity in the PET image is well localised to the tube acting as a spinal cord surrogate, as demonstrated in figure 4.10. This indicates that the measured width of the tube is only slightly larger than those measured in the MR image. On average, the FWHM of the tube in PET images is 4.7% larger than the FWHM for the same line profile in the MR image. Images of the head and neck phantom are shown in figure 4.11. The MR image shows different signal intensities for the main body, bone surrogate material, brain surrogate material and the spinal cord tube attached at the back. An example of the line profiles obtained at position C2 is displayed in figure 4.12, showing the sloping edges of the PET radioactivity concentration peak past the edges of the tube compared to the sharp edge and consistent signal measured from the T1 MR image.

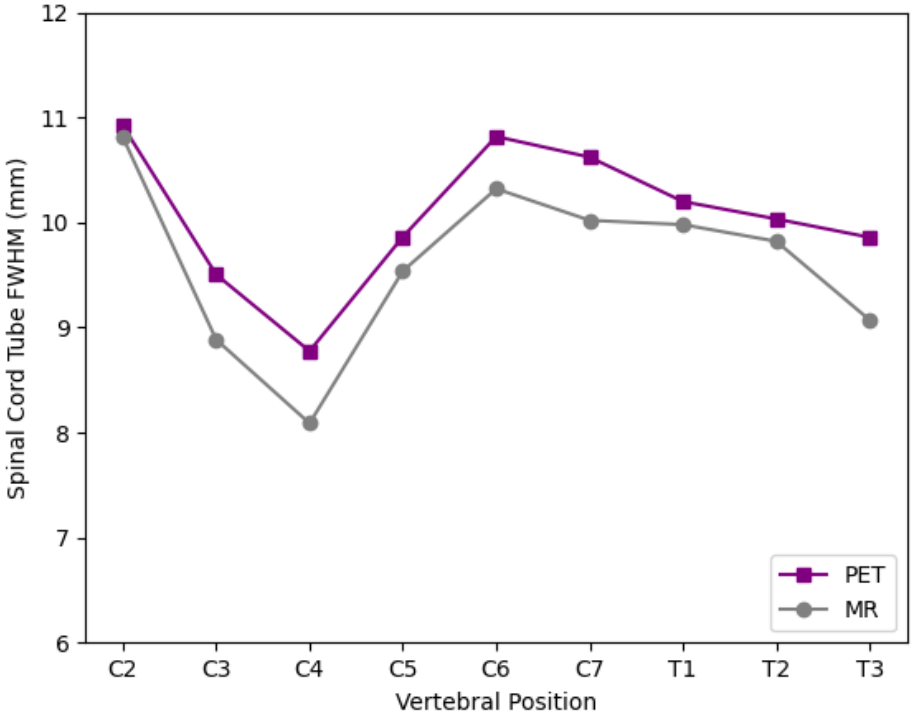


**Figure 4.10**: A plot showing FWHM of the "spinal cord" tube measured from PET and MR images at each vertebral position for the head and neck phantom.

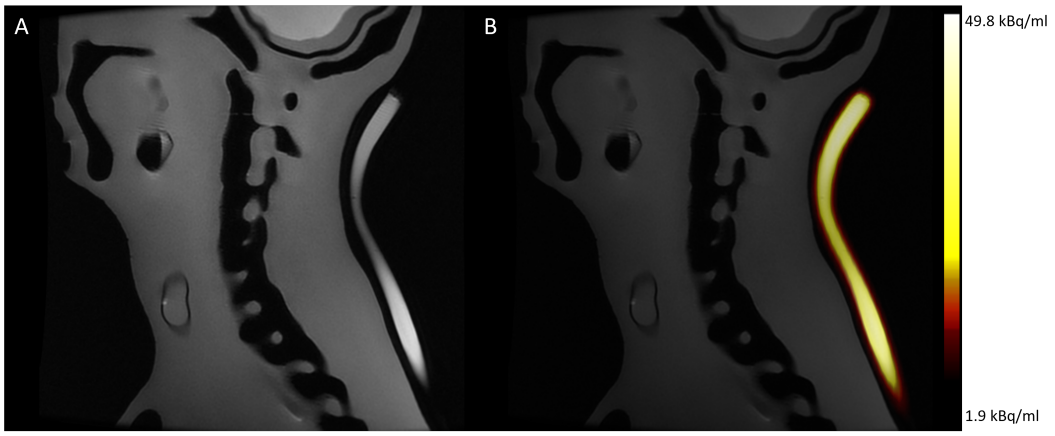


**Figure 4.11**: Sagittal slices of the Head and Neck phantom acquired with T1 weighted MRI (A) and with PET image overlaid (B). The tube is of constant diameter attached to the back of the phantom, however it isn't exactly aligned with the acquisition plane.

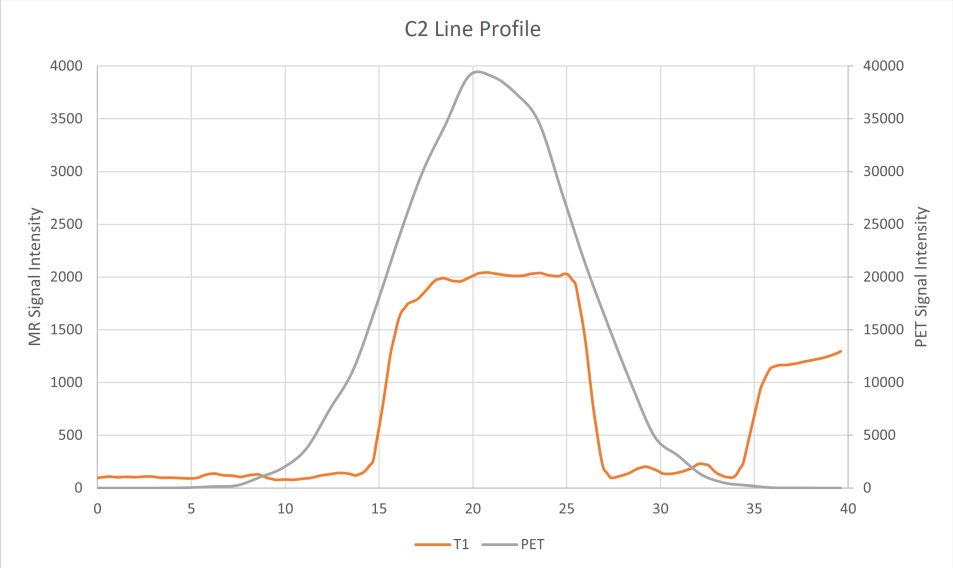


**Figure 4.12**: An example of a line profile for the spinal cord surrogate tube for PET and T1 MRI signal intensity at position C2.

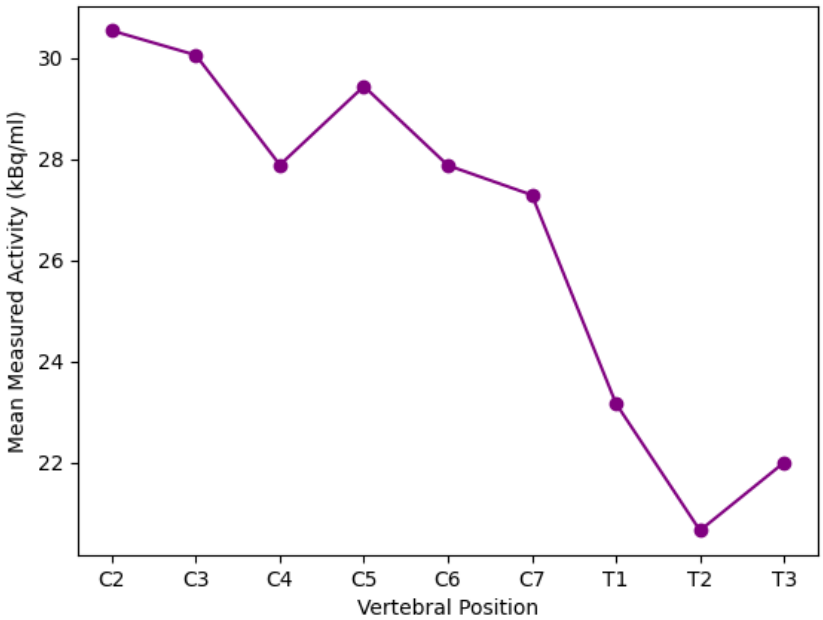


**Figure 4.13**: A plot showing measured radioactivity concentration in the tube at each vertebral position for the head and neck phantom.

Mean radioactivity concentration measured in ROI's within the tube decreases with vertebral position from the neck to the shoulders, as displayed in graph B of figure 4.13. When decay corrected to acquisition start time, an activity of 69kBq/ml is expected to be detected. The highest measured activity is 30.5kBq/ml at C2, which is 43.8% of the expected activity, and decreases to the lowest measured activity of 20.7kBq/ml at T2.

The attenuation maps, or pseudo-CT images, generated within the on board scanner reconstruction software are shown in figure 4.14. These indicate that some areas of the ceramic resin representing bone structures have been assigned as a low density tissue, similar to the lungs, in the chest area. In figure 4.14 this is most clear where the body of the vertebra appears black, indicating a low linear attenuation coefficient is assigned. However, in the shoulders bone features are assigned a higher attenuation value. For accurate attenuation correction, it would be expected that all bone features have a higher linear attenuation coefficient than the surrounding background tissue and lung.

The head insert, shown in figure 4.15, also shows activity outside the point source as measured on MRI. The FWHM of the head insert in the T1 weighted MR images is 3.50mm, but increases to 4.47mm in PET images. Measurements were taken in both x and Y transaxial planes, then averaged. This shows a 27.7% increase in the size of the point source.

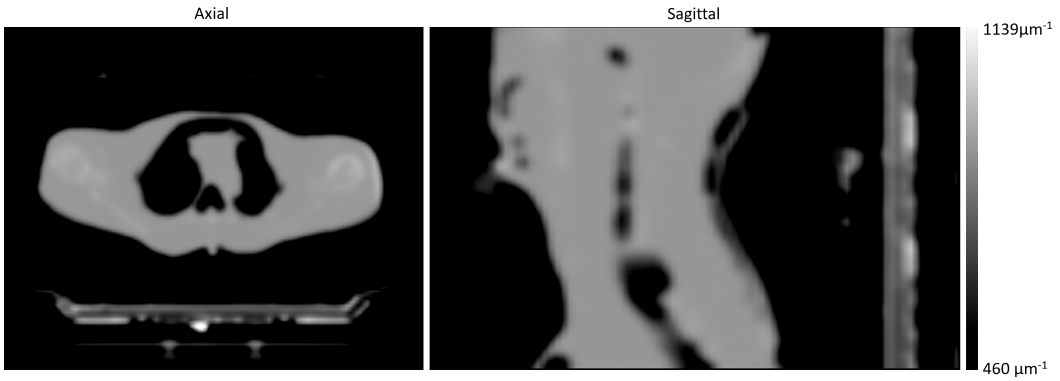


**Figure 4.14**: Example slices in axial and sagittal views of the attenuation map generated of the Head and Neck Phantom from a Dixon MR acquisition, displayed as linear attenuation coefficient in $\mu m^{-1}$.

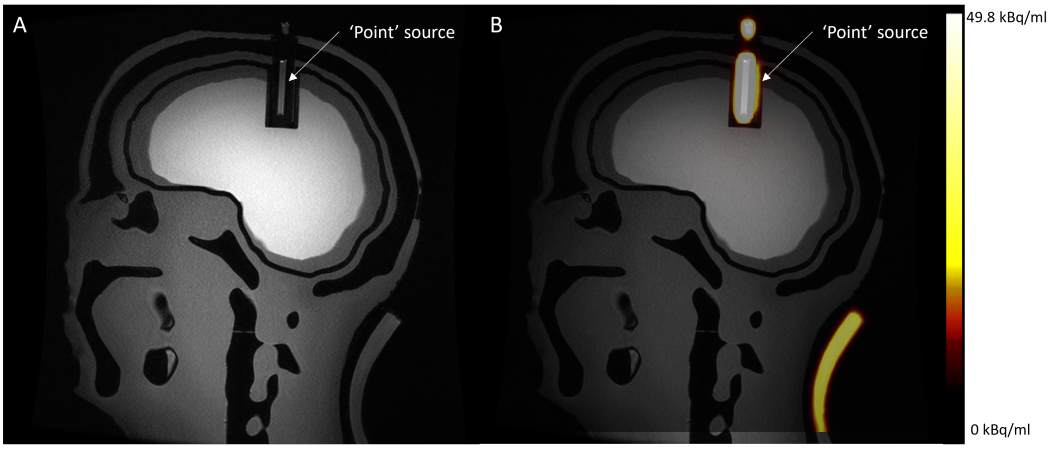


**Figure 4.15**: Sagittal slices of the Head and Neck phantom at the head position, acquired with T1 weighted MRI (A) and with PET image overlaid (B).

## 4.4 Discussion

The results presented here are in line with previously published contrast recovery performance for [$^{18}$F]FDG on the GE SIGNA PET/MR [140], which also show a decrease in CRC with sphere size. For the NEMA IEC Body Phantom, images reconstructed with Q.Clear measured higher radioactivity concentration and higher CRC, with CRC reaching over 90% for the 22mm [$^{18}$F] FDG filled sphere. Contrast recovery coefficient drops in the larger spheres (28mm and 37mm), however these are filled with water only, and a measured radioactivity concentration above zero can reasonably be expected when scatter and background are considered.

The results measuring the FWHM of the spheres suggest some insight into why this decrease in measured radioactivity concentration occurs. Each [$^{18}$F]FDG filled sphere is underestimated by at least 13%, and in some cases up to 27%. The inaccurate measurement of the sphere sizes suggests PET resolution may not be accurate to image features on this scale, giving rise to partial volume effects which reduces quantified activity concentration measured within the spheres.

However, this same underestimation in size is not observed in the tube used to simulate the spinal cord in the Head and Neck phantom. This may be due to phantom geometry, deforming of the tube shape during the experiment leads to inconsistent diameter in some regions, although the diameter of the tube already doesn't accurately reflect changes in human anatomy, which generally decreases into the thoracic spinal cord. In an adult human the diameter may be as small as 6mm [34], so it could be expected that more impact from PVE would occur in these regions. There are also no axial contributions to the PVE due to it's

| Tissue | CT Hounsfield Units | PET linear Attenuation Coefficient ($cm^{-1}$) | T1 Relaxation time at 3T (ms) | T2 Relaxation time at 3T (ms) |
|---|---|---|---|---|
| Cortical Bone | 1000 to 2000 | 0.130 to 0.172 | 400 | 0.3 to 0.5 |
| Muscle | 25 to 40 | 0.094 to 0.100 | 800 to 1000 | 25 to 35 |
| Lung | -200 to -500 | 0.018 to 0.027 | 1000 | 0.7 to 1 |
| Spinal Cord | 35 to 40 | - | 800 to 1000 | 70 to 80 |

**Table 4.2**: Tissue properties and ideal tissue mimicking phantom of the spinal cord should aim to replicate for assessment of spinal cord imaging in PET/MR. Values for tissue properties reported in a range of literature sources [11–17]

cylindrical geometry as there are for the spheres of the NEMA phantom.

The tube also isn't submerged in background activity, but rather is attached to the outside of the phantom. In this respect, the spinal cord surrogate is an inaccurate physical representation, as the tube is effectively a larger line source suspend in air. This changes its position relative to the highly attenuating vertebral bone features. However, a decrease in measured radioactivity concentration relative to the administered activity is still seen in the results for mean ROI radioactivity concentration. This may be due to incorrectly applied attenuation correction. Assigning large sections of the vertebra, the most dense material in the phantom, with an air or lung linear attenuation coefficient will lead to under-correction of PET activity along the affected lines of response. This mainly occurred in the region of the chest and shoulder sections of the phantom, but not in the neck, which would provide some explanation as the why measured radioactivity concentration decreases along the length of the tube from the base of the head into the chest. This is also true in clinical scanning, where bone in Dixon derived PET/MR attenuation maps is assigned the same value as soft tissue, which can lead to an underestimation of activity in the spine [58].

The head and neck phantom was modified for this experiment, but still did not reflect the anatomy under investigation. Ideally, a custom built phantom for the spinal cord would feature a section of the neck and chest with a fillable 1cm diameter tube insert running through the spine surrogate material to more closely simulate the anatomy of the spine and spinal cord. We would propose that such a phantom should aim to replicate both MR and PET tissue properties for the anatomy of interest, the properties of which are displayed in table 4.2.

Whilst acquiring phantom data was useful in identifying areas of investigation in spinal cord PET/MRI, neither phantom was able to replicate the conditions in clinical spinal cord imaging for both PET and MRI. Considering the information

gained from the literature review, it was determined that the cost, timescale and workload required to create a tissue mimicking phantom for the spine and spinal cord in PET/MRI would constitute a substantial project in itself. As a result, further phantom work for this project used the computational phantom - the XCAT version 2 mathematical phantom, created by Segars et al. [192] at Duke University, and widely used as a computational phantom in Nuclear Medicine.

## 4.5 Conclusion

Analysis of the phantom acquisitions from this experiment revealed two sources of error for investigation into their impact on spinal cord PET/MRI. By measuring radioactivity concentration and line profiles across phantom features of comparable size to the spinal cord diameter, we have found the size and boundaries of these features to be inconsistent with their true extent. This indicates that an investigation into partial volume effects in the spinal cord is required.

Secondly, when assessing the attenuation map for the head and neck phantom, we have found features that do not produce an MR signal have been incorrectly assigned when the attenuation map is derived from the Dixon MR sequence. As this applies to cortical bone, a tissue with close proximity to the spinal cord, an investigation into the impact of MR derived attenuation correction on spinal cord imaging in PET/MR is also needed.

# Chapter 5

# Quantification of [$^{18}$F]FDG in the Spinal Cord for PET/MRI

## 5.1 Introduction

Combined Positron Emission Tomography and Magnetic Resonance Imaging (PET/MRI) has been used extensively in the research of neurological conditions in the brain, however, no reliable imaging biomarkers in the spinal cord have been found for a number of neurodegenerative diseases [35]. Previous studies looking at spinal cord PET and PET with computed tomography (PET/CT) in adults have observed a generally decreasing pattern of [$^{18}$F]FDG uptake in the spinal cord from cervical to thoracic spine with a peak in the lower cervical spine[26, 101, 193]. This peak in activity at the lower cervical spine has been explained as being due to an increased amount of grey matter and enlargement of the spinal cord diameter at this position [26]. However, partial volume effects may lead to underestimation of activity in other regions of the spinal cord with a smaller ($< 10mm$) size [193]. Additionally, it is reported that there are quantitative differences in the spinal cord uptake between PET/CT and PET/MRI [5]. One explanation is that the properties of bone are not accounted for in attenuation and scatter correction in PET/MRI when using attenuation maps derived from a Dixon MRI sequence. Some brain imaging protocols implement a Zero Echo Time (ZTE) or Ultrashort Echo Time (UTE) sequence [64, 194], allowing for the skull to be delineated and assigned bone attenuation values However, no commercially available software has implemented solutions for other areas of the body [195]. Some attempts to resolve attenuation correction challenges have lead to investigations into deep learning [196] and other novel methods such as dual tracer imaging to implement an additional bone tissue class into pseudo-CT generation [197].

The first aim of this study is to investigate whether failing to fully account for attenuation and scatter contributions of bone in image reconstruction leads to errors in measured spinal cord activity. This is achieved through a simulation study using the XCAT mathematical phantom [192] to simulate an [$^{18}F$]FDG PET activity distribution to include the spinal cord, which allows for simulated MR derived attenuation maps to be compared to a known true attenuation map. We also investigate how this is impacted by detector resolution and partial volume effects.

The second aim is to determine whether currently implemented image reconstruction methods can resolve attenuation correction errors and partial volume effects in the spinal cord through the use of point spread function (PSF) modelling and time of flight (TOF) corrections. Use of TOF image reconstruction algorithms has previously been reported to reduced quantification errors in bones and lungs when MR derived attenuation maps are used [56], and to improve image contrast and detection of small lesions [198]. We compare mean Standardised uptake values ($SUV_{mean}$) in a section of the spinal cord in images reconstructed from clinical research data using algorithms implemented in the vendor software. To compare against attenuation corrected data, the spine is manually segmented for each subject to introduce as a bone structure into the pseudo-CTs used for attenuation correction.

## 5.2 Methods and Materials

### 5.2.1 Simulation

The XCAT mathematical phantom (version 2) [192] was used to generate [$^{18}F$]FDG tracer distributions of organs in the neck and thorax, shown in figure 5.1, for a single 25cm field of view based on reported uptake in healthy subjects [101, 199–203]. The values used are listed in table 5.1. We used the XCAT standard male and standard female phantoms. Phantoms were simulated to a voxel size of $2.1 \times 2.1 \times 2.8$mm. 511keV photon attenuation maps were also generated for the region by the XCAT software. Attenuation maps were scaled to units $cm^{-1}$. Modified attenuation maps were also generated to simulate those derived from Dixon MRI sequences, which was achieved by replacing all bone linear attenuation coefficients $\geq 1.2cm^{-1}$ with a muscle linear attenuation coefficient of $0.99cm^{-1}$ [14]. Both attenuation maps are shown in figure 5.2.


**Figure 5.1**: The male XCAT phantom as simulated in this project, with an [$^{18}F$]FDG distrbution for 1 field of view of the neck and thorax, scale is in units of kBq/ml.

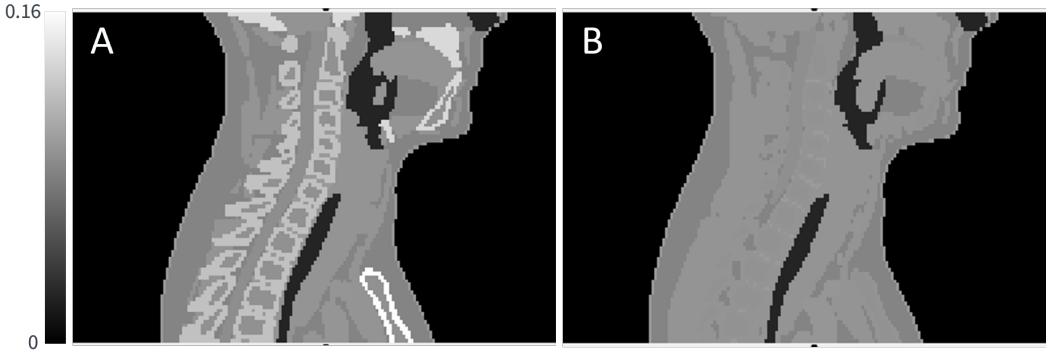


**Figure 5.2**: The attenuation maps of the male XCAT phantom as simulated in this project, with A) showing the original 511keV photon attenuation map, and B) showing the same map with bone features removed to simulate an MR derived attenuation map, scale in units cm$^{-1}$.

Each XCAT distribution was forward projected using SIRF [28] to generate a sinogram of the distribution. Attenuation correction factors (ACFs) were obtained from the attenuation maps with bone attenuation coefficients present, and scatter was calculated using the Single Scatter Simulation (SSS) algorithm in STIR [27]. The XCAT activity, ACF and scatter sinograms were combined for sinograms simulating acquired PET data [204]. Poisson noise was added to sinogram data by scaling the number of counts in the sinogram to a value representative of the acquired PET and randomly drawing samples from a Poisson distribution. The sinogram was then scaled back to the original number of counts prior to image reconstruction. Time of flight information was not included in simulated data.

| Organ | Organ Activity (male XCAT) $kBqml^{-1}$ | Organ Activity (female XCAT) $kBqml^{-1}$ | Reference |
|---|---|---|---|
| Spinal Cord | 8.75 | 8.5 | Patel et al. [101] |
| Cervical Vertebrae (Marrow) | 7.6 | 8 | Shen et al. [199] |
| Thoracic Vertebrae (Marrow) | 8.8 | 9 | Shen et al. [199] |
| Myocardium (LV) | 26 | 33.5 | Zincirkeser et al. [200] |
| Lung | 3 | 3 | Zincirkeser et al. [200] |
| Aorta (Ascending) | 9.5 | 9.5 | Zincirkeser et al. [200] |
| Aorta (Descending) | 10 | 8.5 | Zincirkeser et al. [200] |
| Vena Cava | 8.5 | 8 | Zincirkeser et al. [200] |
| Thyroid | 7.5 | 7.5 | Zincirkeser et al. [200] |
| Salivary Glands | 8.5 | 9.5 | Zincirkeser et al. [200] |
| Nasopharynx | 8.5 | 9.5 | Zincirkeser et al. [200] |
| Tongue | 9.5 | 9.5 | Zincirkeser et al. [200] |
| Tonsil | 19 | 18.5 | Zincirkeser et al. [200] |
| Esophagus | 7.9 | 7.9 | Ramos et al. [201] |
| Larynx | 16.5 | 16.5 | Ramos et al. [201] |
| Lymph | 12.5 | 12.5 | Kang at al. [203] |
| Cerebra | 44.5 | 47.5 | Zincirkeser et al. [200] |
| Cerebellum | 33.5 | 37 | Zincirkeser et al. [200] |
| Breast | - | 2.15 | Ramos et al. [201] |
| Blood Pool (Heart) | 10 | 10 | Heusch et al. [202] |
| Muscle (Background) | 3.7 | 3.7 | Heusch et al. [202] |
| Skin | 4.7 | 4.7 | Ramos et al. [201] |

**Table 5.1**: PET organ activities used in assigning uptake when configuring the XCAT phantoms, calculated from values reported in literature. Where SUV was reported, organ activity was estimated for an administered activity of 400MBq and body weights supplied for the relevant XCAT phantoms. In cases where values were not segregated by sex the same value was used in both phantoms.

ACFs and scatter were also calculated for the attenuation maps without bone to be used during image reconstruction. Simulated sinograms were reconstructed using an Ordered Subset Expectation Maximisation (OSEM) algorithm (28 subsets, 2 iterations, voxel size $2 \times 2 \times 2.8$mm) with attenuation and scatter correction. Image reconstruction for each phantom was performed twice: once with attenuation and scatter correction calculated from the attenuation map with bone and once with corrections calculated from the attenuation map without bone. A schematic of the main processes involved in this simulation is shown in figure 5.3. Point spread function (PSF) modelling was not included.

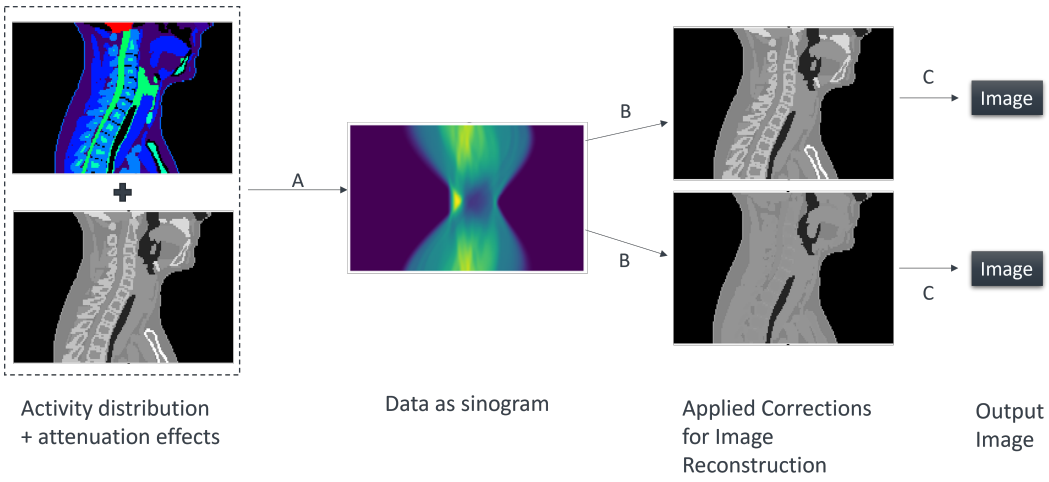


**Figure 5.3**: A simple schematic of the simulation and image reconstruction process as described in this chapter. Step A) represents the forward projection of the phantom distributions to sinogrma data, b) represents the calculation of correction factors for the two different image reconstruction methods and C) represents reconstruction of the corrected data to the resulting images.

To perform simulations at scanner resolution, the average distance of the spinal cord to the image centre was measured on patient acquisitions so that NEMA performance results for the scanner could be used to determine an appropriate resolution for the simulation representative of spinal cord acquisitions. From an average distance of 2.4cm, a transaxial resolution of 4.4mm and an axial resolution of 6mm, which was simulated by applying a 3D Gaussian filter to the generated XCAT activity distributions and attenuation maps using ImageJ [205]. The simulation and image reconstruction process in STIR was repeated as described above for these filtered XCAT phantom distributions to simulate sinogram data and images acquired on a scanner detector resolution representative of a clinical PET/MRI scanner.

#### Analysis

5mm spherical ROIs were drawn in the spinal cord at each vertebral level corresponding to vertebra C1 to T5. Mean activity and standard deviation were measured for each ROI.

Measurements were averaged for the male and female XCAT phantom images and linear regression was performed using mean measured uptake from each ROI to demonstrate the trend of activity along the length of the spinal cord, with 95% confidence intervals also calculated. Wilcoxon signed rank test was used to determine the statistical significance of results, as this analysis is suitable for non-parametric paired data. Results are considered statistically significant where $P < 0.05$.

### 5.2.2 Clinical Acquisition

Imaging was performed on the SIGNA PET/MR scanner (GE HealthCare Inc.) in accordance with the Declaration of Helsinki, with ethics committee approval and all participants gave written informed consent. Two participants were administered 250MBq [$^{18}F$]FDG 60 minutes before acquisition. This gives a mean effective radiation dose of 4.75mSv to the patient, using the conversion of 0.19mSv/MBq as stated in International Commission on Radiological Protection (ICRP) report 106 [206]. PET data was acquired at two bed positions for 10 min per bed in head-first supine orientation. MRI was performed simultaneously to PET using the body coil for the dedicated attenuation correction Dixon and Zero Echo Time (ZTE) sequences, as well was as the following anatomical sequences using a head and neck coil: axial T1-weighted Fast Spin Echo (FSE) and Axial T2-weighted FLAIR (Fluid Attenuated Inversion Recovery) for the brain, and sagittal T2-weighted FSE, Sagittal T1-weighted FLAIR and Axial T2-weighted FSE of the spinal cord.

PET image reconstruction was performed offline using the vendor-provided software Duetto version 02.18, using both OSEM and TOFOSEM (Time of Flight OSEM) with 28 subsets and 2 iterations to a voxel size $2.3 \times 2.3 \times 2.8$mm. Reconstructions with PSF modelling were performed separately to the same parameters. MR-derived attenuation correction was used with ZTE sequences included for the head, and built-in templates for MR coils [207]. Images were reconstructed both without any post-filtering and with a 5mm transaxial Gaussian filter and 3-point axial convolution filter of [1 4 1] applied post reconstruction. All parameters were chosen as representative of clinical use cases.

Reconstructions were also performed using the Q.Clear algorithm, a Bayesian penalised likelihood reconstruction method (GE HealthCare Inc.) with a single

parameter beta ($b$) that can be modified by the user. This dictates the strength of the prior as shown in equation 2.4 (denoted at $\beta$). Q.Clear and TOF Q.Clear were performed with $b$ = 100, 200, and 400, all of which are initialised using a 2 iteration OSEM reconstruction. Q.Clear reconstruction improves signal to noise ratio and visual detection of lesions, however previous work to quantify measured activity and contrast recovery has shown that $b \leq 400$ is required for features with less than 10mm diameter without losing signal intensity and contrast to noise ratio (CNR) [68], so optimisation of higher beta values was not pursued in this study.

### Introducing Vertebral Bone to Attenuation Correction

Another avenue of investigation into the effects of vertebral bone in attenuation correction was to introduce vertebral bone into the image reconstruction process for participant acquisitions. Cortical bone in the vertebra was manually segmented using the software 3DSlicer 5.6.1 [208] from ZTE, and anatomical T1 and T2 images acquired simultaneously with PET for study participants.

Pseudo-CTs derived from Dixon MR images, from which attenuation maps are calculated and are displayed in Hounsfield units (HU), were modified by introducing the vertebral bone segmentations as areas with 800HU [11]. These pseudo-CTs were then used for attenuation and scatter correction, and image reconstruction was performed as described in section 6.2.2.

### Analysis

Activity is normalised to body weight and displayed as Standardised uptake values ($SUV_{bw}$), which is used in all results presented for this part of the study. Spherical ROIs, 5mm in diameter, were drawn in the spinal cord at each vertebral level on the T2 weighted MRI from C1 to T4 and used to mean SUV ($SUV_{mean}$) and standard deviation for each ROI in the PET images.

$SUV_{mean}$ for each ROI was averaged over both patient acquisitions and linear regression was performed to demonstrate the trend of activity along the length of the spinal cord. Wilcoxon signed rank test was used to determine the statistical significance of results, with Bonferroni corrections applied where test were applied to compare several different results. The Bonferroni correction is a conservative safeguard against type 1 errors in statistical analysis, by dividing the usually accepted significance value of $P > 0.05$ by the number of times the test is run.

## 5.3 Results

### 5.3.1 XCAT Simulations

For the XCAT phantom simulated at 2mm resolution, a decreasing pattern of uptake along the length of the spinal cord is measured, as shown in figure 5.4, despite a constant value initially assigned in the XCAT distribution. When bone features are maintained in attenuation and scatter correction, measured uptake in the cervical spine is more consistent with the initial assigned value, but decreases in the thoracic spinal cord. For images reconstructed without bone included in attenuation maps measured uptake is overall lower then the fully attenuation corrected images, ranging from 3%-6.7% decrease in the cervical spinal cord and 9.5%-10.4% in the thoracic spinal cord ($P < 0.001$).

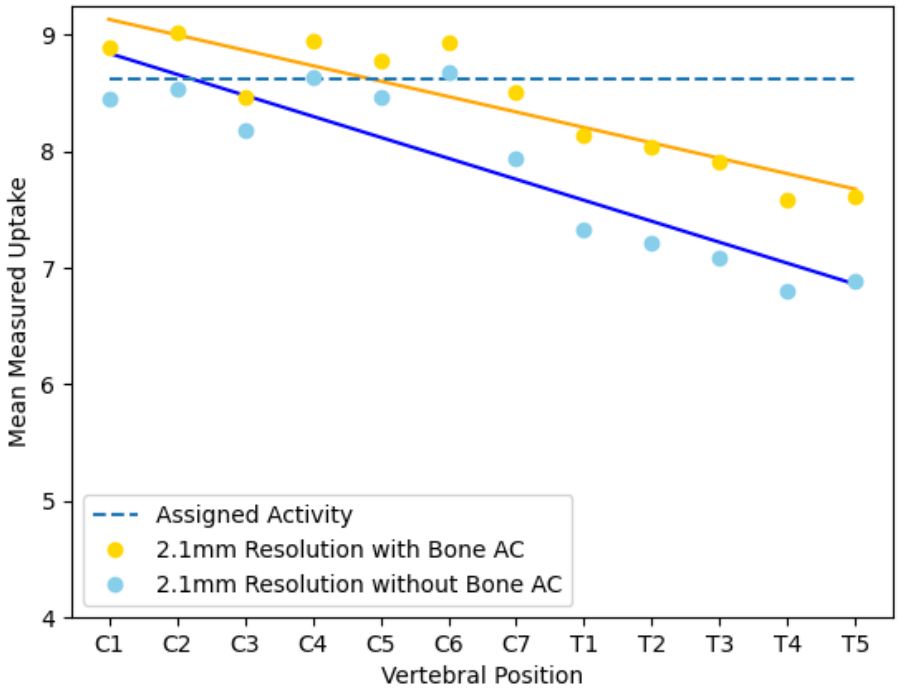


**Figure 5.4**: Average activity measured in the spinal cord at each vertebral position for images of the simulated XCAT phantoms at high resolution ($2 \times 2 \times 2.8$mm) when reconstructed using an attenuation map with or without bone.

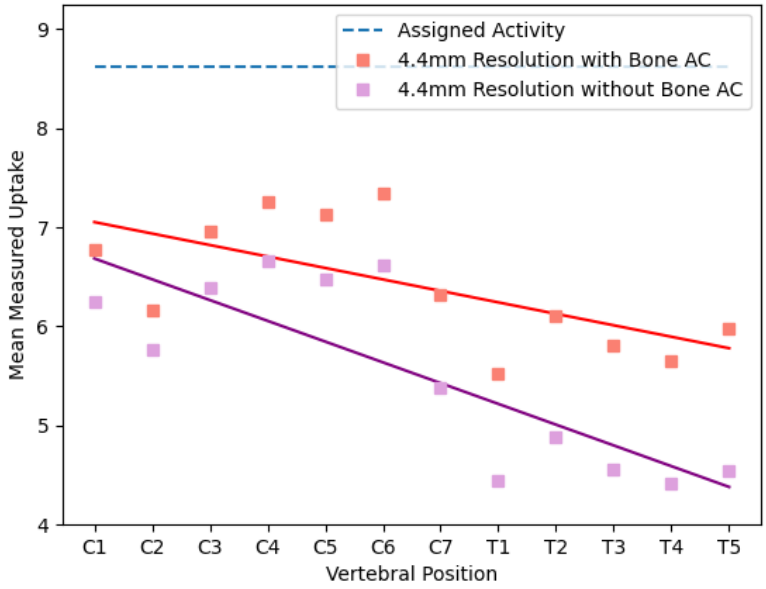


**Figure 5.5**: Average activity measured in the spinal cord at each vertebral position for images of the simulated XCAT phantoms at scanner resolution ($4.2 \times 4.2 \times 6.1$mm) when reconstructed using an attenuation map with or without bone, with trendlines calculated by linear regression.

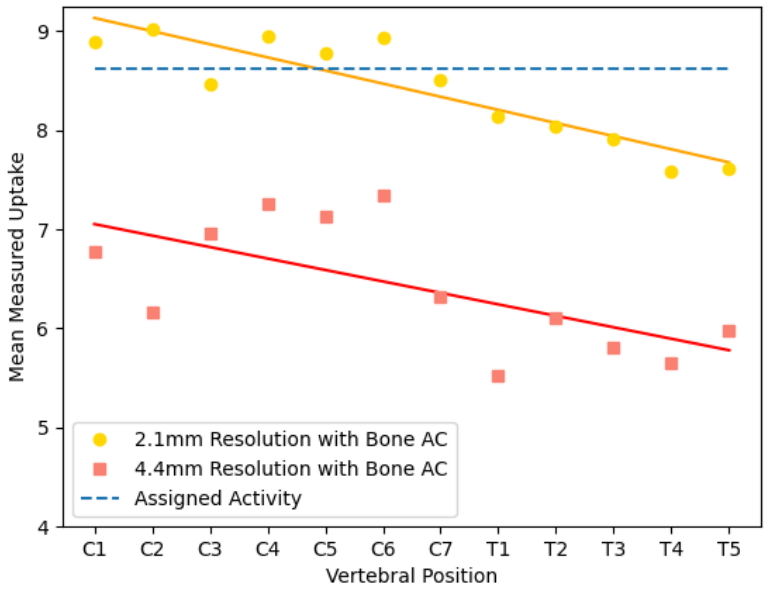


**Figure 5.6**: Graphs comparing different simulated detector resolution when reconstructed using an attenuation map with bone.

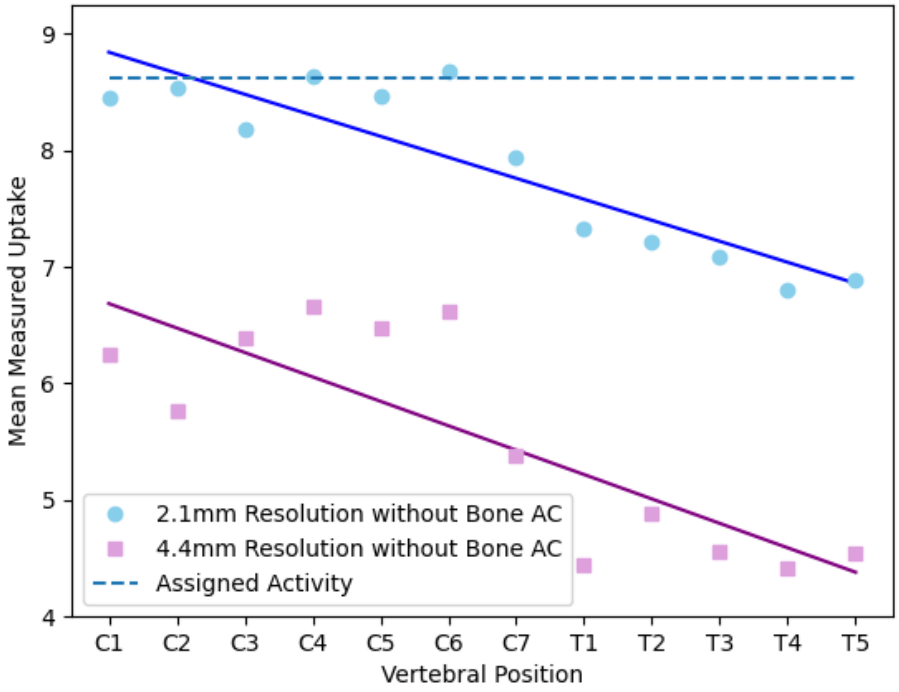


**Figure 5.7**: Graphs comparing different simulated detector resolution when reconstructed using an attenuation map without bone (b).

Images reconstructed from sinograms of the XCAT phantom simulated with a 4.2mm detector resolution show a more rapidly decreasing trend in measured uptake along the length of the spinal cord compared to the higher resolution images, as shown in figures 5.5, 5.6 and 5.7. This is also shown visually in fig 5.8 where the difference between the original distribution and reconstructed images is higher in the thoracic spine. The difference in uptake is measured at a 17.8%-32.2% difference in images fully attenuation and scatter corrected ($P < 0.001$) when comparing different simulated resolutions. The difference in measured activity in the spinal cord between attenuation correction methods is also greater, giving a 6.4%-14.8% difference in the cervical spine and 19.4%-23.9% difference in the thoracic spine ($P < 0.001$).

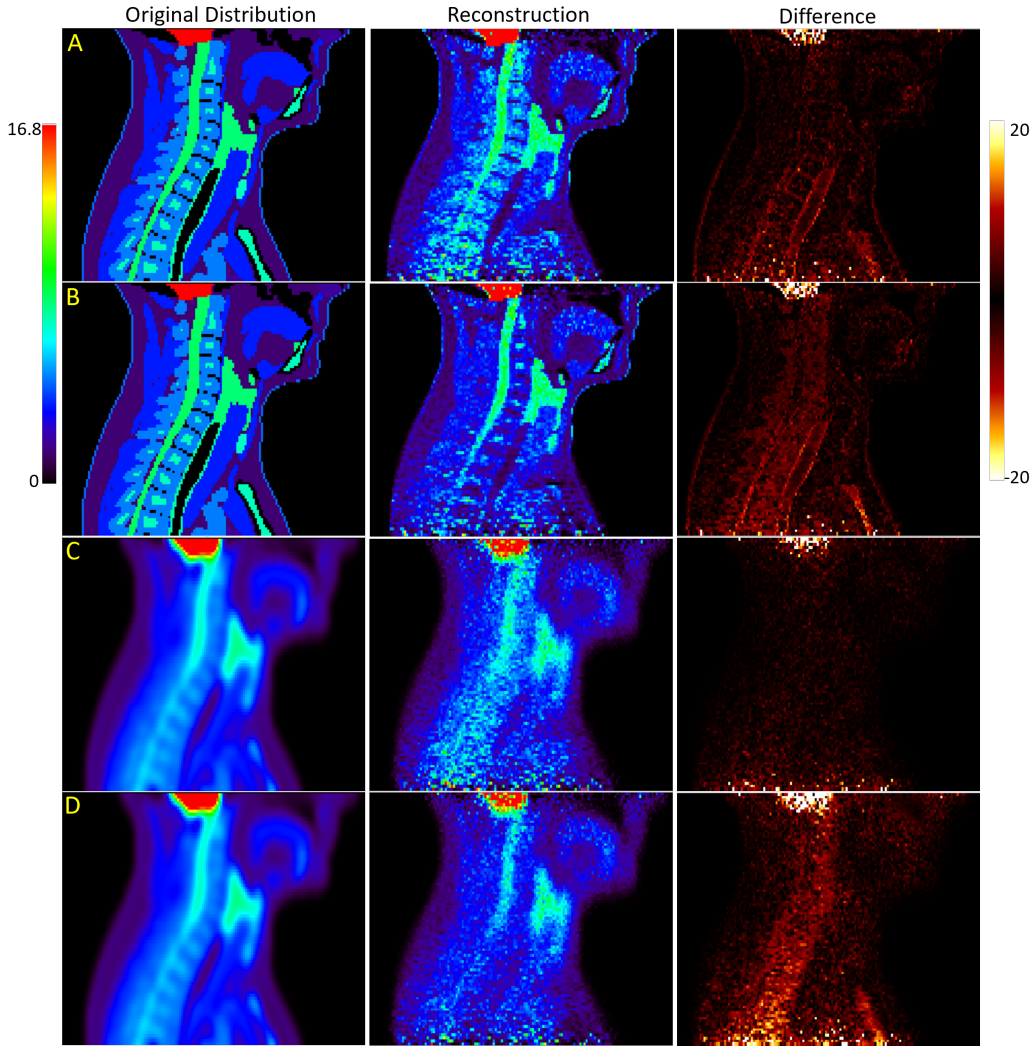


**Figure 5.8**: Images of the XCAT male phantom reconstructed with OSEM at high resolution (rows A,B) and scanner resolution (rows C,D) with rows B and D using attenuation maps without bone. The last image in each row shows the difference between reconstruction and original simulated distribution.

### 5.3.2 Clinical Acquisitions

$SUV_{mean}$ in images reconstructed with vertebral bone added to pseudo-CT's for attenuation correction was increased across all algorithms, compared to using the original MR derived pseudo-CT. In non-TOF OSEM reconstructions, this corresponds to a 1.7%-11% increase in $SUV_{mean}$ in the cervical spinal cord and 10.7%-16.4% in the thoracic spinal cord ($P < 0.001$) when the spine is included for attenuation correction, as demonstrated by the trends displayed in figure 5.9. An example of the modified pseudo-CT, incorporating vertebral bone as segmented from MR, is provided in figure 5.10.

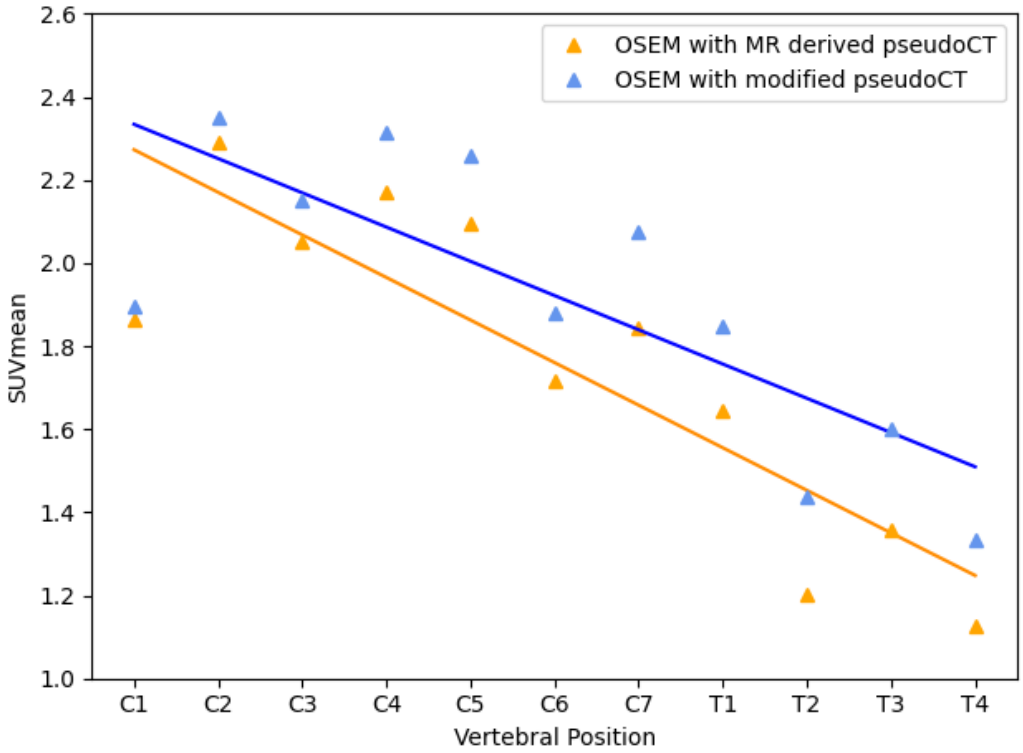


**Figure 5.9**: Linear trend lines of average measured activity along the spinal cord for PET images reconstructed using an OSEM algorithm with an MR derived attenuation map and an attenuation map with segmented vertebral bone added.

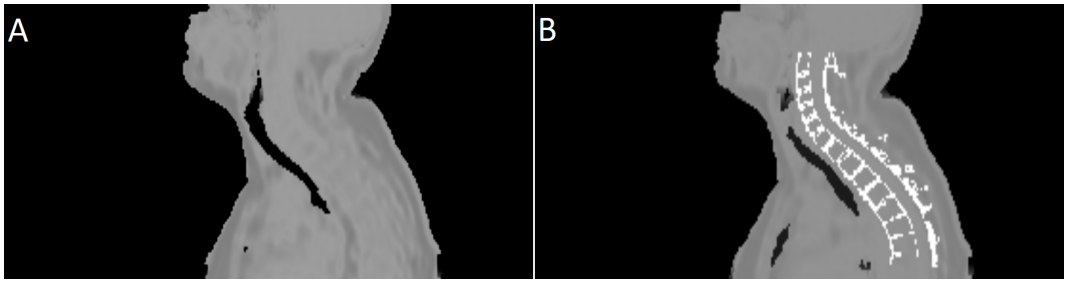


**Figure 5.10**: An example of pseudo-CT's used to derive attenuation maps when created from Dixon MRI sequence by the vendor software (A) and with segmented cortical bone from the spine added (B)

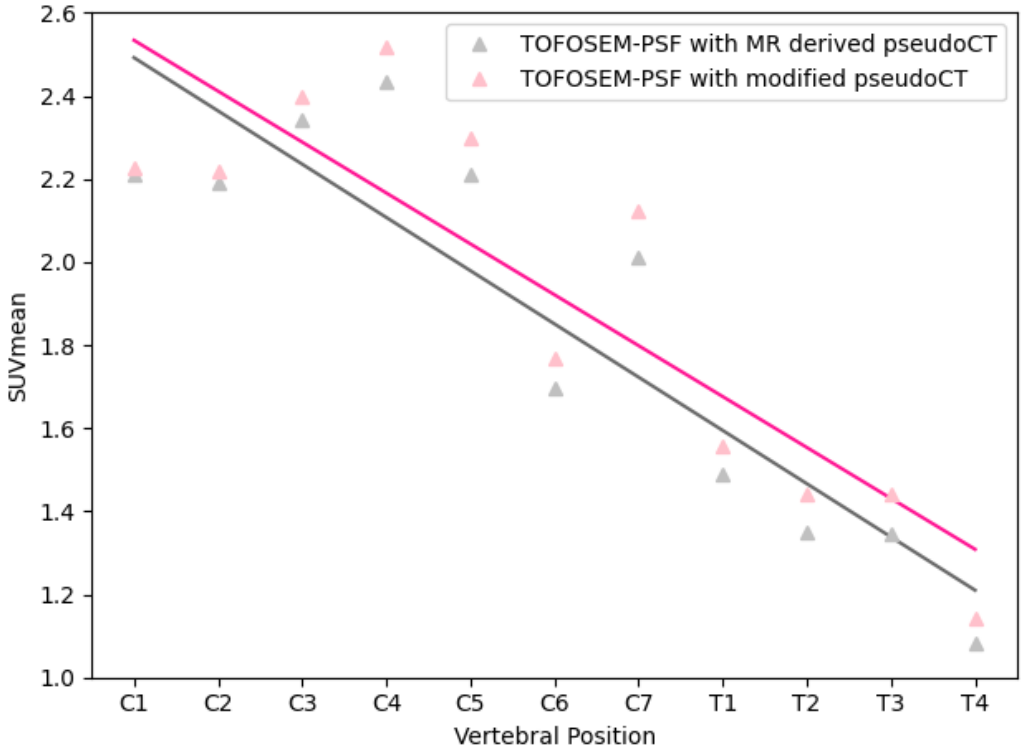


**Figure 5.11**: Linear regression of $SUV_{mean}$ along the spinal cord for images reconstructed with TOFOSEM with PSF modelling, showing measurements for images with and without the vertebral bone segmentation included in the attenuation map.

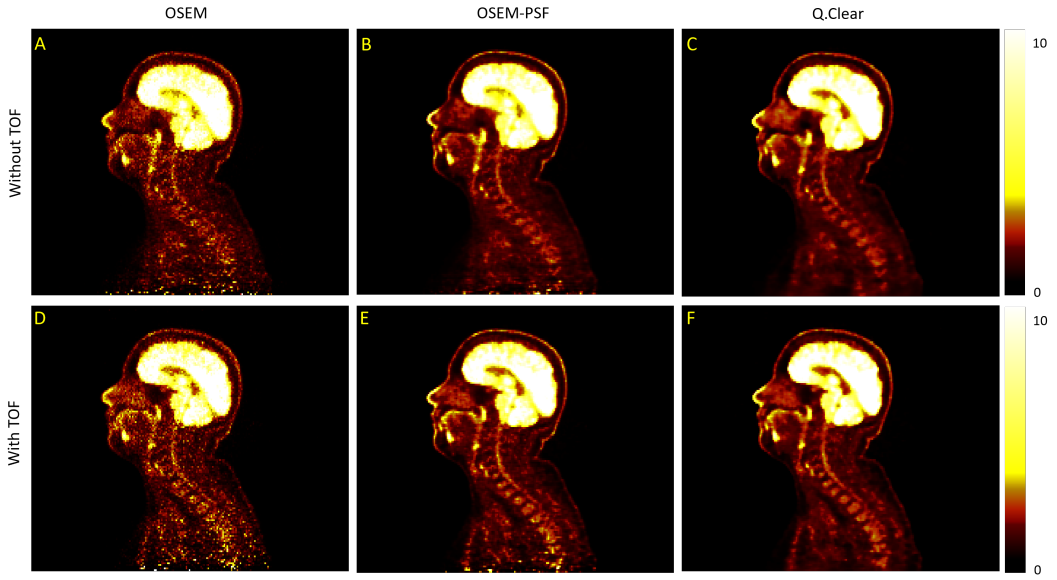


**Figure 5.12**: Examples of PET images reconstructed using different image reconstruction algorithms for the same acquisition, with no post-filtering applied, displayed in $SUV_{bw}$. The algorithms used are OSEM (A), OSEM-PSF (B), Q.Clear (C), TOFOSEM (D), TOFOSEM-PSF (E), TOF Q.Clear (F).

Using time of flight (TOF) algorithms, as in figure 5.11, reduces the difference between reconstructions with and without vertebral bone attenuation to 0.7%-6.6% for TOFOSEM-PSF ($P < 0.001$), compared to the 1.9%-17.2% when OSEM-PSF is used. Changes to $SUV_{mean}$ in the spinal cord following TOF correction are not considered significant when compared to the same algorithm without TOF ($0.03 \leq P \leq 0.7$ for compared algorithms, with significance taken to be $\alpha = 0.017$ following Bonferroni correction for 3 comparisons). This is highlighted in figure 5.12, which displays images for the same patient and same pseudo-CT reconstructed with each algorithm option available, with no obvious differences in the spinal cord.

Applying PSF corrections doesn't introduce any change to the trend in activity along the spinal cord ($P = 0.6$ for MR derived pseudo-CT and $P = 0.9$ for modified pseudo-CT, shown in figure 5.13) or impact the comparison between attenuation correction approaches at the chosen parameters of 2 iterations and 28 subsets, as shown in figures 5.14. However, figures 5.16 and 5.18 demonstrate that at an increased number of iterations images reconstructed with PSF correction do see an increase in measured activity for OSEM and TOF-OSEM algorithms ($P = 0.01$ and $P = 0.05$ respectively at 10 iterations), and this is greater than the increase from OSEM convergence alone (figures 5.15 and 5.17. However, as displayed in figure 5.19, increasing the number of iterations significantly increases noise in the final images.

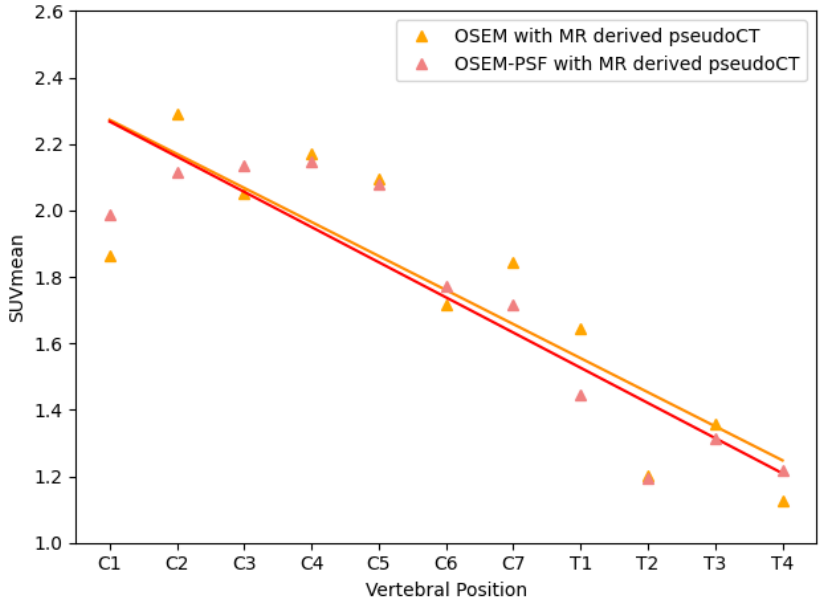


**Figure 5.13**: Linear trend lines of average measured activity along the spinal cord for PET images reconstructed with attenuation corrected with an MR derived attenuation map, using an OSEM algorithm at 2 iterations and 28 subsets, with and without PSF correction applied.

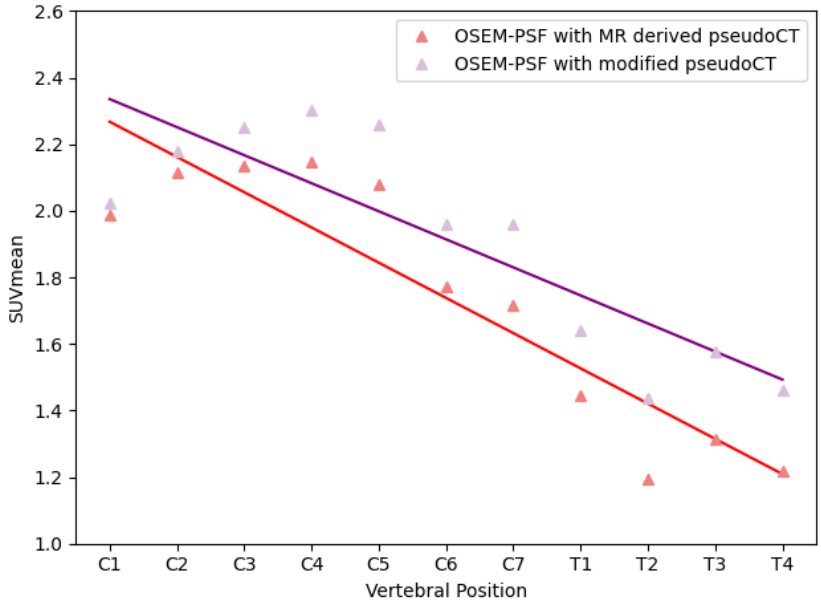


**Figure 5.14**: Linear trend lines of average measured activity along the spinal cord for PET images reconstructed using an OSEM algorithm with PSF correction, and attenuation corrected with an MR derived attenuation map and an attenuation map with segmented vertebral bone added.

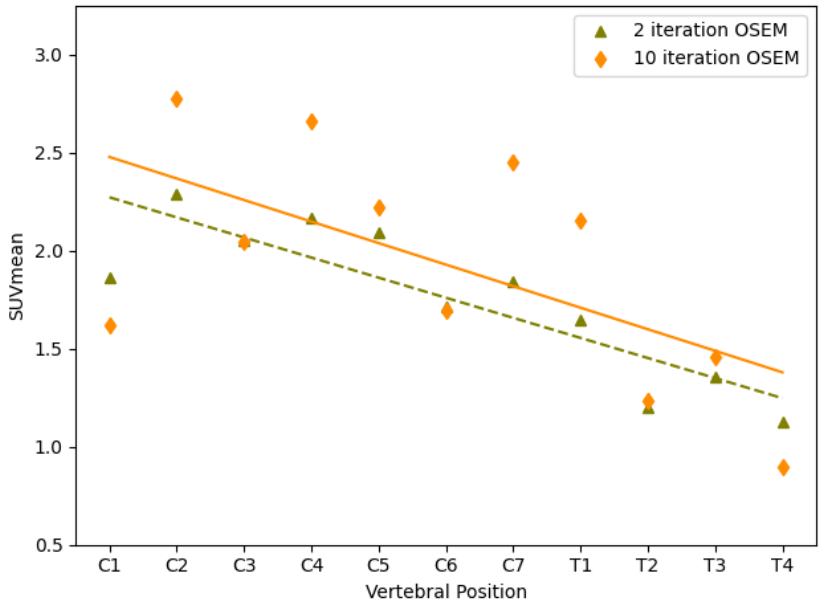


**Figure 5.15**: Linear regression of $SUV_{mean}$ along the spinal cord for images reconstructed with OSEM with an MR derived attenuation map. Dashed lines indicate measurements for images reconstructed to 2 iterations while the solid line shows the same measurements in images reconstructed to 10 iterations.

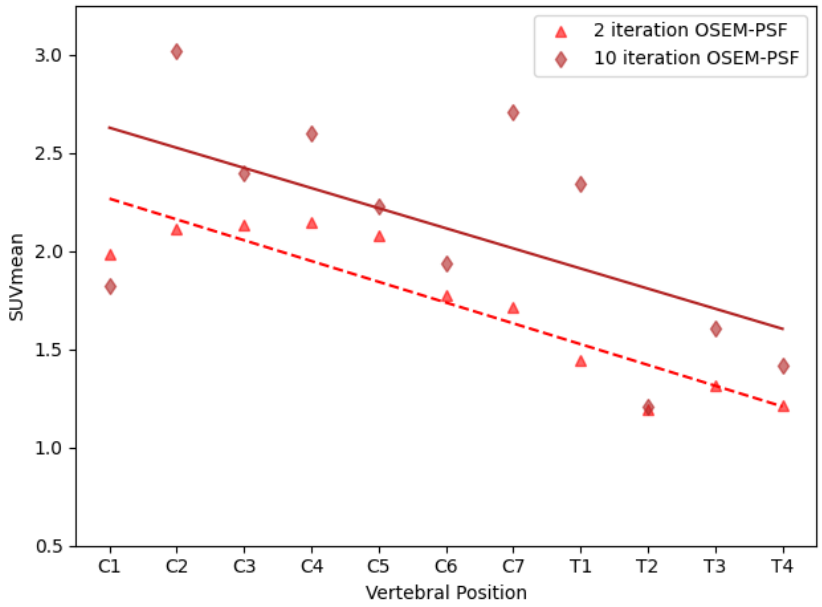


**Figure 5.16**: Linear regression of $SUV_{mean}$ along the spinal cord for images reconstructed with OSEM-PSF, with an MR derived attenuation map. Dashed lines indicate measurements for images reconstructed to 2 iterations while the solid line shows the same measurements in images reconstructed to 10 iterations.

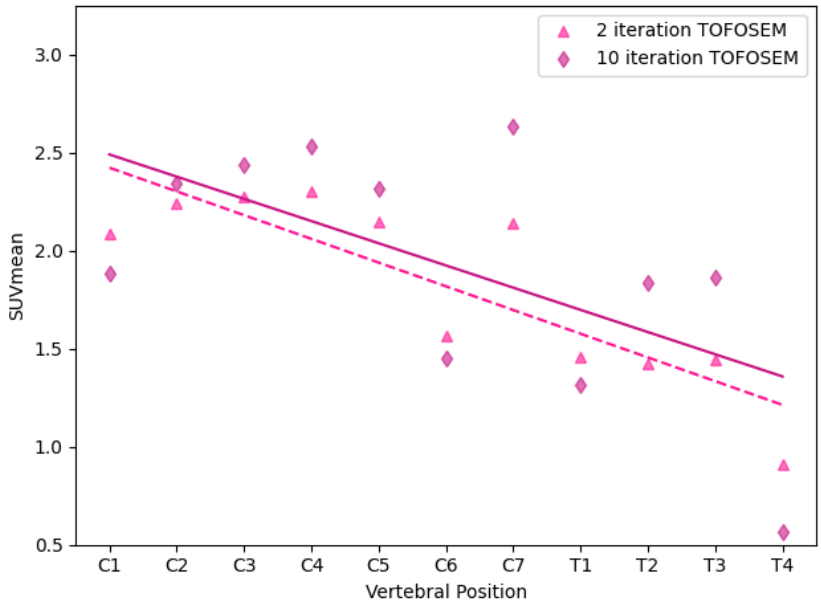


**Figure 5.17**: Linear regression of $SUV_{mean}$ along the spinal cord for images reconstructed with TOFOSEM, with an MR derived attenuation map. Dashed lines indicate measurements for images reconstructed to 2 iterations while the solid line shows the same measurements in images reconstructed to 10 iterations.

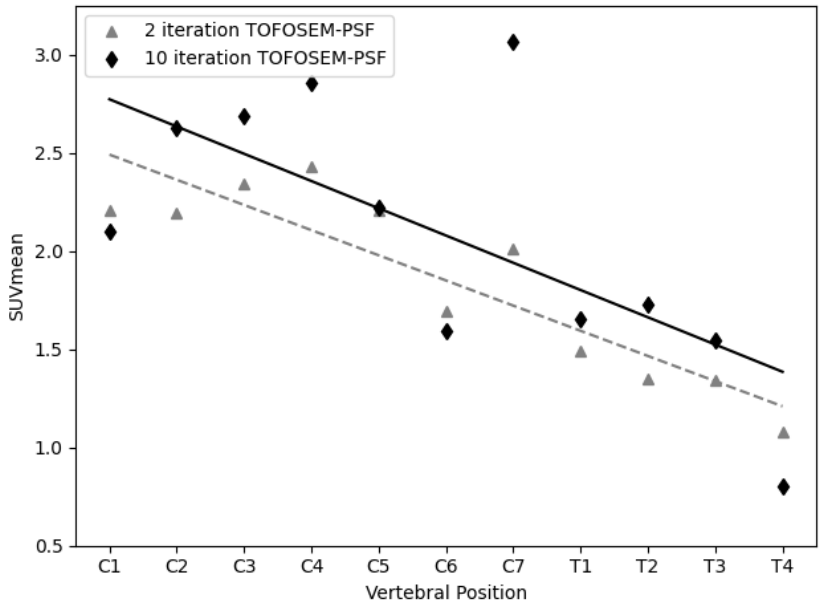


**Figure 5.18**: Linear regression of $SUV_{mean}$ along the spinal cord for images reconstructed with TOFOSEM-PSF, with an MR derived attenuation map. Dashed lines indicate measurements for images reconstructed to 2 iterations while the solid line shows the same measurements in images reconstructed to 10 iterations.

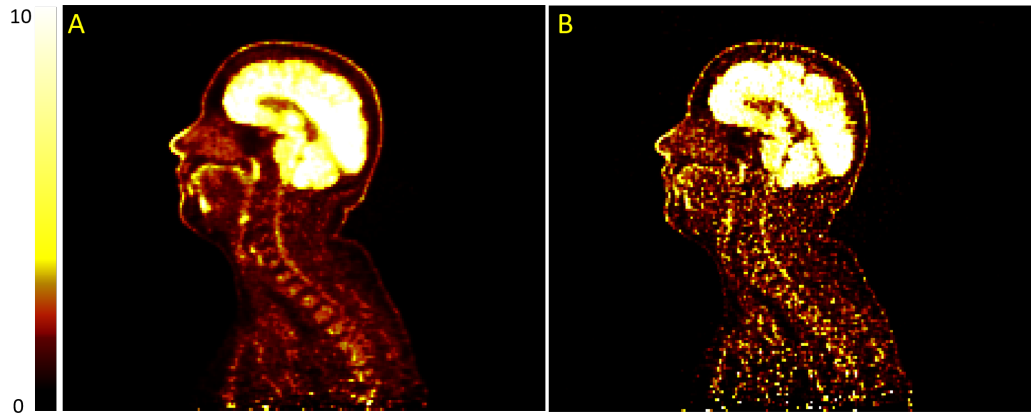


**Figure 5.19**: Example images for images reconstructed with TOFOSEM-PSF at 2 iterations (A) and 10 iterations (B). The image becomes sharper and recover more activity in the spinal cord at higher iterations but with a large increase in image noise.

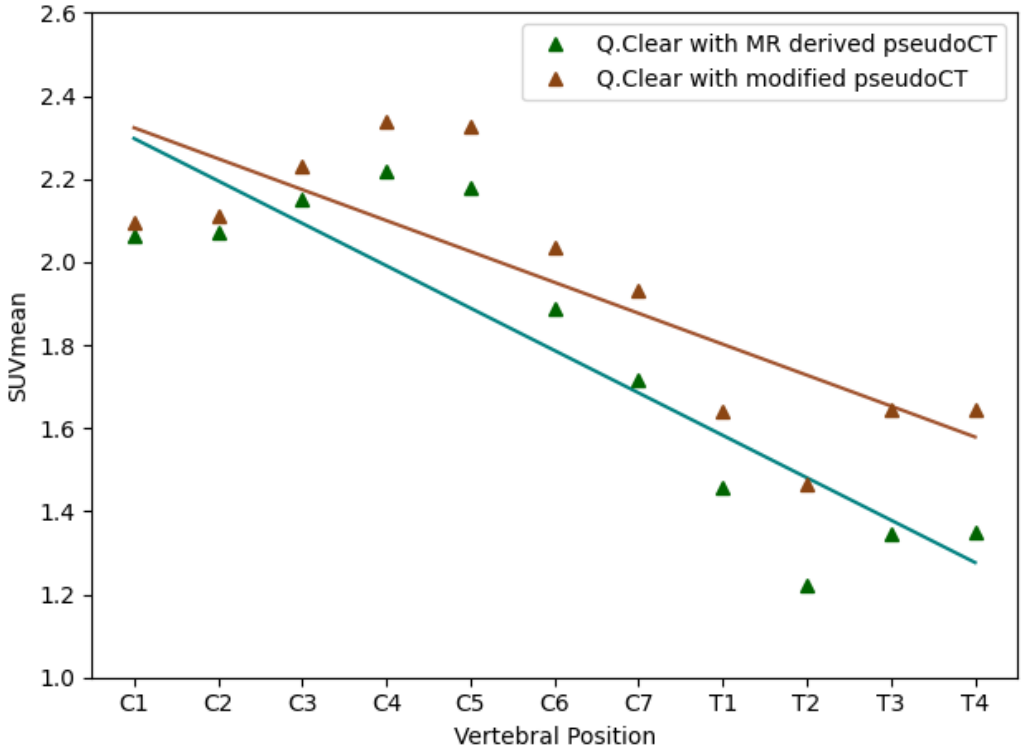


**Figure 5.20**: Linear trend lines of average measured activity along the spinal cord for PET images reconstructed using the Q.Clear algorithm, with attenuation corrected with an MR derived attenuation map and an attenuation map with segmented vertebral bone added.

The same trends were observed in images reconstructed using the Q.Clear algorithm, demonstrated in figure 5.20 and 5.21. Changing beta in TOF Q.Clear reconstructions introduced small quantitative changes ($P < 0.001$ for $\beta = 100$ to $\beta = 400$, $P = 0.002$ for all other comparisons) with $SUV_{mean}$ decreasing with increasing beta, as shown in figure 5.22. Of the beta values tested, assigning b = 100 gave the smallest difference in $SUV_{mean}$ between images reconstructed with the MR-derived and modified pseudo-CT's for attenuation correction, ranging from 0.6%-5.2%. This result was the smallest range of difference in $SUV_{mean}$ found when comparing images reconstructed with different attenuation correction pseudo-CTs in this study.

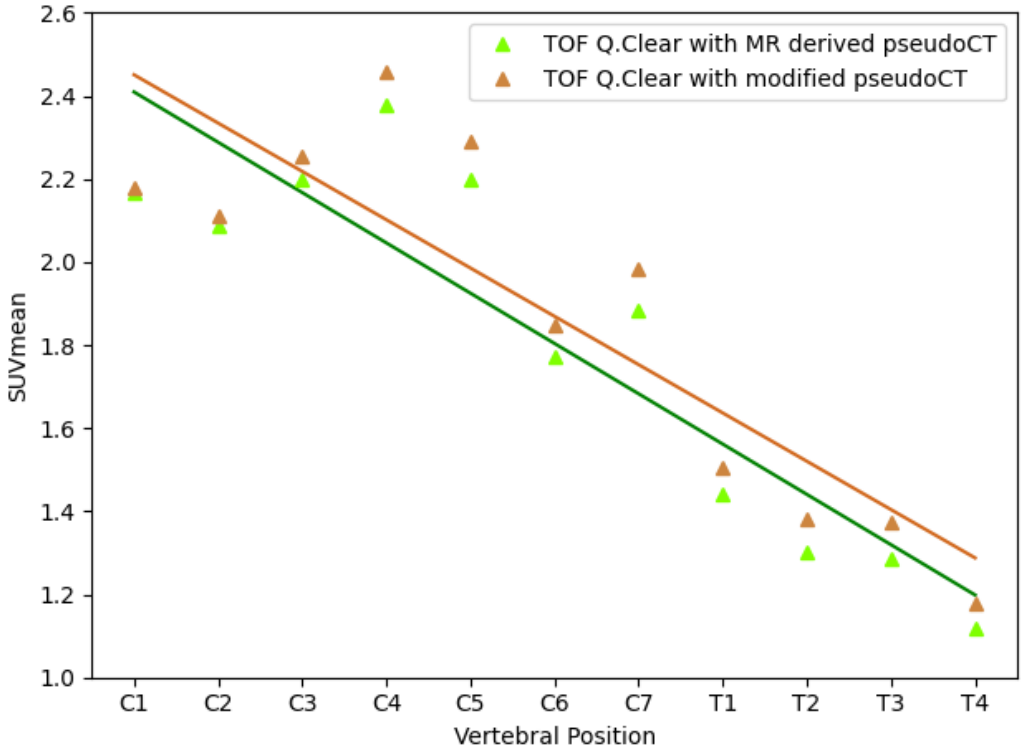


**Figure 5.21**: Linear trend lines of average measured activity along the spinal cord for PET images reconstructed using the TOF Q.Clear algorithm, with attenuation corrected with an MR derived attenuation map and an attenuation map with segmented vertebral bone added.

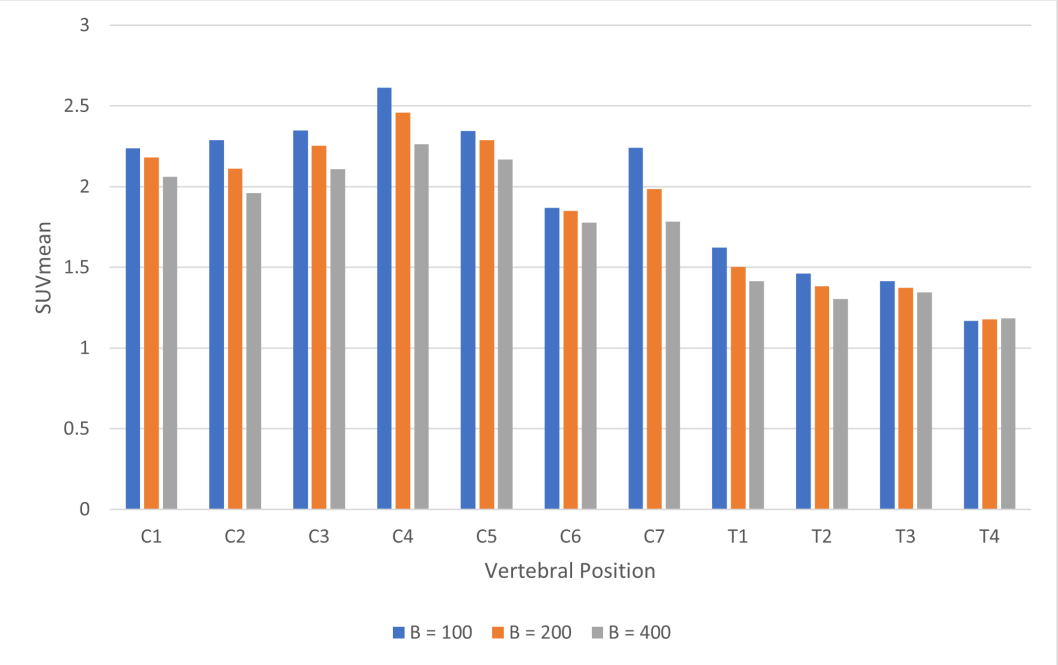


**Figure 5.22**: Histogram of $SUV_{mean}$ in the spinal cord by vertebral position for images reconstructed using TOF Q.Clear with beta = 100, 200, 400.

Examples of images for each OSEM algorithm used with and without post-filtering are displayed in figures 5.25 and 5.26. Images with post-filtering applied demonstrate the same trends in $SUV_{mean}$ along the spinal cord, but with an reduction in measured activity by 1.1%-20.7%. This was only considered significant for reconstructions with PSF modelling ($P < 0.001$ OSEM-PSF, $P = 0.002$ TOFOSEM-PSF, with an example of this trendline shown in figures 5.23 and 5.24). Differences between images reconstructed with and without vertebral bone included in the attenuation maps were also consistent with unfiltered images. In time of flight reconstructions, the difference in $SUV_{mean}$ between spinal cord ROI in equivalent images when post-filtering was applied was greater, up to 20.7% of TOFOSEM and 17.9% for TOFOSEM-PSF, than the difference measured when applying different attenuation correction approaches (range 0.7%-6.6%).

Whilst in all clinical acquisitions the linear trendlines show a decrease in radiotracer uptake along the length of the spinal cord, it is apparent from the plotted data points in figures 5.9, 5.11, 5.13, 5.14, 5.20, 5.21 that the pattern of measured tracer uptake is consistent at the start of the cervical spine, but decreases rapidly into the thoracic spinal cord. This is also consistent with visual interpretation of the images in figure 5.12, as well as the expectation that uptake may be reduced here due to increased attenuation along LORS in the thorax compared to the neck, and the known decrease in spinal cord diameter in the thoracic spine.

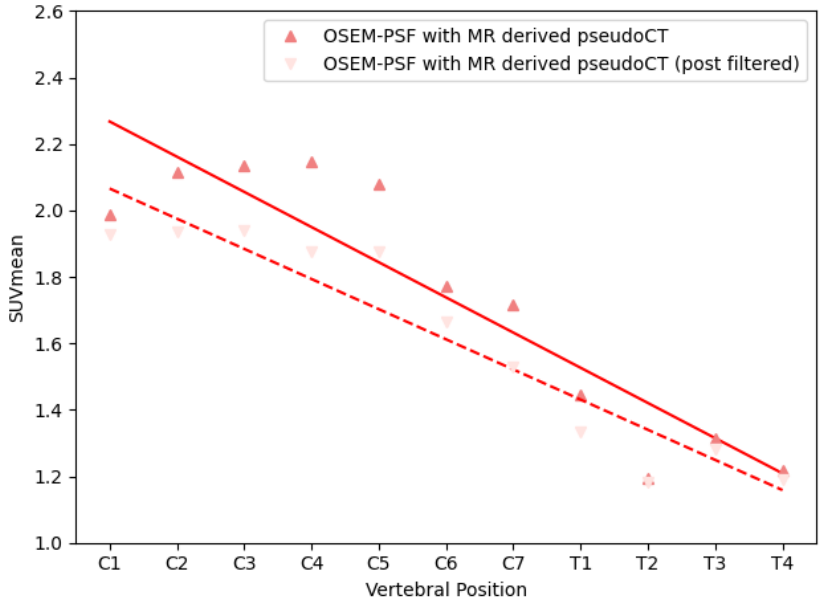


**Figure 5.23**: Linear trend lines of average measured activity along the spinal cord for PET images reconstructed using an OSEM algorithm with PSF correction and a Gaussian post-filter applied, and attenuation corrected with an MR derived attenuation map.

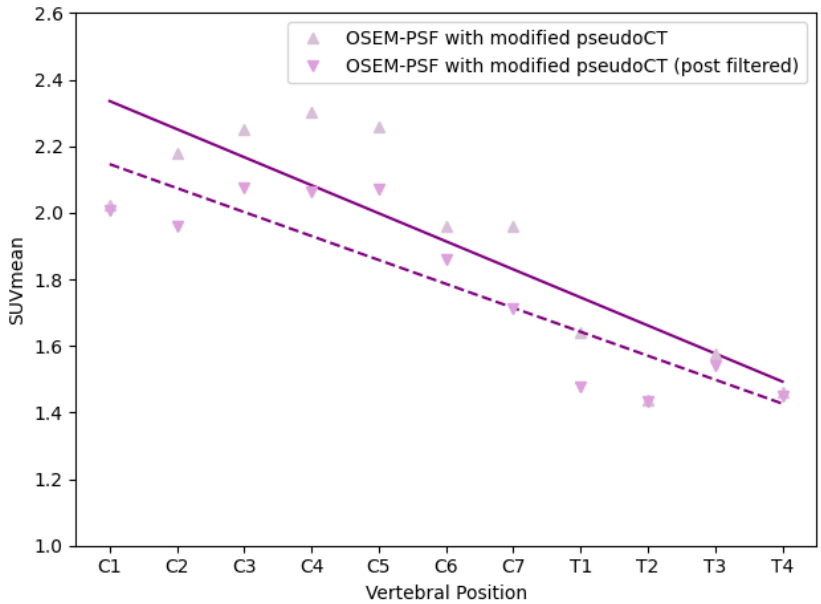


**Figure 5.24**: Linear trend lines of average measured activity along the spinal cord for PET images reconstructed using an OSEM algorithm with PSF correction and a Gaussian post-filter applied, and attenuation corrected with an attenuation map with segmented vertebral bone added.

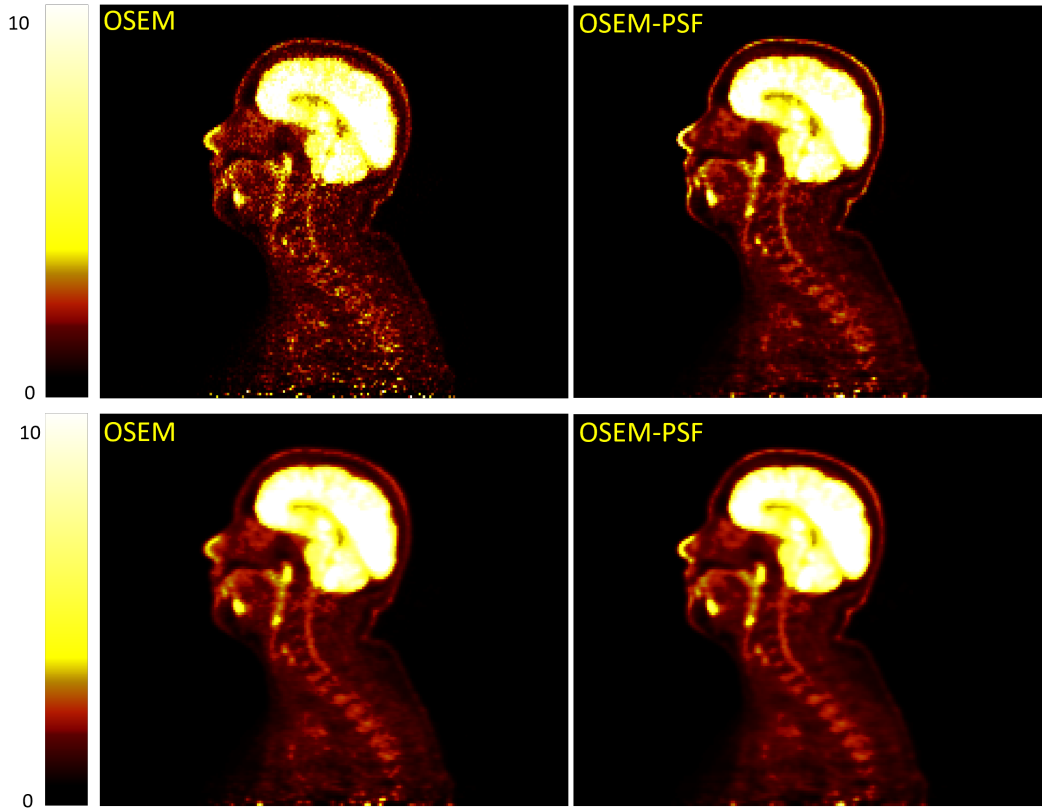


**Figure 5.25**: Examples of PET images with post-filtering (5mm transaxial Gaussian filter and 3 point axial convolution [1 4 1] filter) applied (bottom row) to OSEM reconstructed images with and without PSF modelling, displayed in $SUV_{bw}$.

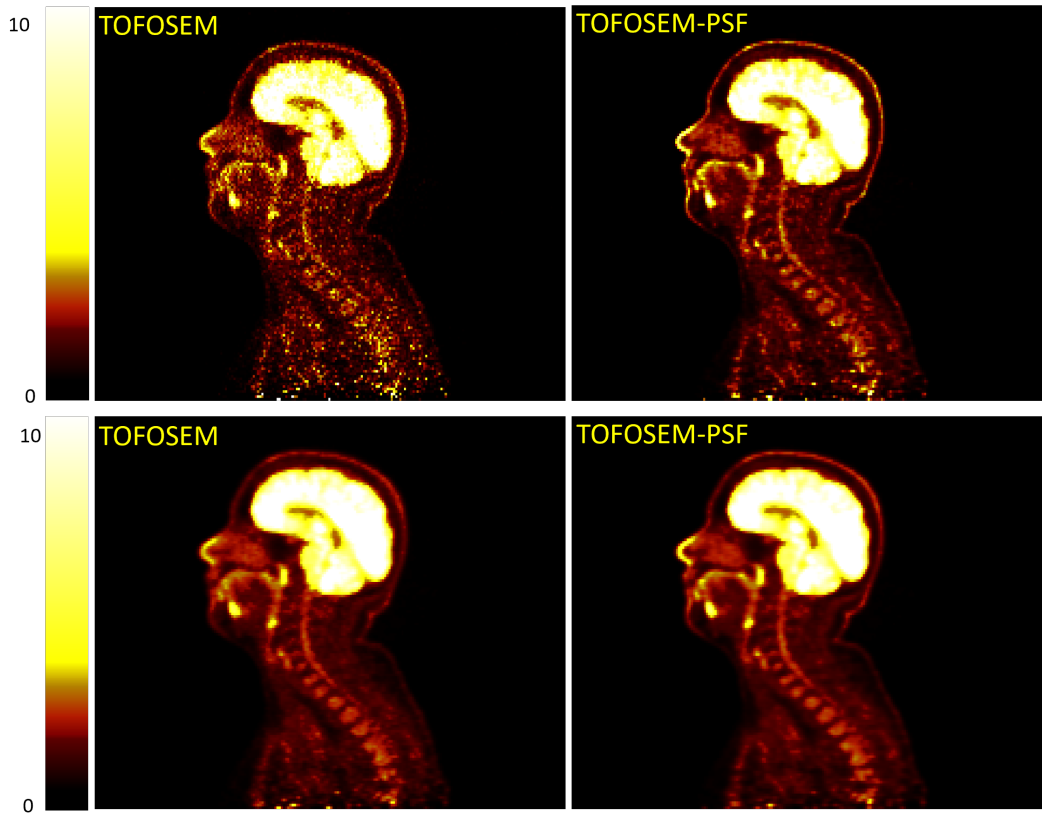


**Figure 5.26**: Examples of PET images with post-filtering (5mm transaxial Gaussian filter and 3 point axial convolution [1 4 1] filter) applied (bottom row) to TOFOSEM reconstructed images with and without PSF modelling, displayed in $SUV_{bw}$.

## 5.4 Discussion

XCAT simulation results indicate that disregarding bone in attenuation correction maps affects the quantification of the activity in the spinal cord, with a statistically significant decrease in measured uptake of up to 10.4% when compared to fully attenuation corrected images. This is in line with a previous study [58] reporting on the impact of MR-derived attenuation correction on SUV in spine lesions, where they conclude that the impact of removing bone from attenuation maps is dependent on the proximity of the region of interest to bone. Detector resolution also plays a role in this by reducing overall measured activity by up to 32.2% relative to the true uptake which we conclude is due to partial volume effect. This acts in combination with the choice of attenuation correction leading to a further reduction in activity when bone is ignored in MR derived attenuation maps, particularly in the thoracic spine. This consideration is important as previous literature reports a decreased pattern of uptake along the length of the spinal cord to be physiological [101, 193]. Whilst there is other evidence to suggest this may be true for [$^{18}F$]FDG uptake [26, 193], research is ongoing into novel central nervous system tracers for which this is not the case [209] and the effects presented in this study may confound results for these studies.

Time of flight is not considered as part of the simulation phase of this study, which would also improve the localisation of detected photons. These results suggest that partial volume effects do occur in spinal cord PET, as previously proposed [26], and that partial volume correction should also improve quantification in the spinal cord. One way in which this is commonly performed is by detector response modelling, which is not considered during simulation due to the lack of an appropriate model in the current implementation of SIRF.

In patient data, the addition of cortical bone from the vertebra to attenuation maps lead to an overall increase in measured uptake in the spinal cord of up to 17.2%. Although this wasn't as large a difference as demonstrated in simulated data, it is in line with previous work investigating 5-tissue class attenuation maps for spinal cord PET/MR [87]. OSEM and OSEM-PSF reconstructions saw the largest disparity between images reconstructed with or without vertebral bone. Inserting segmented bone features into attenuation maps can be prone to errors when applying a Hounsfield unit that is not patient specific [19]. MR derived segmentation can also be affected by patient motion [210], which is not accounted for in this study. However, in the absence of same patient CT acquisitions this provides a useful example of the role vertebral bone plays in attenuation correction. The PSF modelling used in this software is based on the scanner model and

includes spatial variation across the field of view, but introducing PSF modelling didn't make a significant difference to measured activity in the spinal cord for the reconstruction parameters used. The OSEM parameters were chosen to reflect common clinical practice, however, it has been shown that applying PSF in EM algorithms can slow convergence in early iterations [211]. Subsequently, we have demonstrated that applying PSF corrections when reconstructing PET data does lead to an increase in $SUV_{mean}$ in images reconstructed with OSEM and TOFOSEM to 10 iterations, however this must be balanced with increased image noise and computation time.

TOF correction caused the inclusion of vertebral bone in attenuation correction to have less of an impact on measured uptake, suggesting that time of flight in PET-MR can overcome the barriers faced by a lack of CT or transmission based attenuation correction. This aligns with previously reported results in other organs [56]. This may be due to improved contrast recovery and faster convergence in TOF reconstructions as emission data is better localised [56, 198]. As PET image reconstruction is a complex problem with multiple sources of error, including those arising from attenuation and scatter, using TOF algorithms may lead to the effects of these errors also becoming more localised. Further assessment against a known ground truth image would help in determining the impact TOF algorithms have on quantification across the whole image.

Applying post-filtering reduced measured uptake in all cases, to a maximum reduction of 20.7%. In TOF reconstructions this had a greater impact on $SUV_{mean}$ in the spinal cord than changing attenuation correction approach, which showed a maximum of 6.6% change in $SUV_{mean}$. For small diameter structures, care should be taken in performing quantification on post-filtered images.

Results from the Q.Clear algorithm displayed the same trends as in OSEM, with TOF reducing the difference in $SUV_{mean}$ between different attenuation correction maps from a maximum of 18.3% reduction in $SUV_{mean}$ for Q.Clear to a maximum of 6.2% with TOF Q.Clear at beta = 200. Increasing beta decreased measured uptake in the spinal cord, in agreement with previously reported results [68, 212]. The images reconstructed with beta = 100 gave the lowest difference between the two attenuation maps, which also corresponds to the previous studies in suggesting that a beta value of 100 - 200 is more appropriate for applications with small ($< 10mm$) regions of interest when using Q.Clear.

### 5.4.1 Future Work

Future work in this area would be to investigate resolution recovery and partial volume correction that can be applied to PET data in PET/MRI. Hybrid recon-

struction algorithms, using anatomical MRI as a prior for PET data reconstruction [29], could be beneficial in maintaining the distinction between the spinal cord and surrounding active tissue in PET/MRI, and has previously been implemented for time of flight PET data [189].

Numerous partial volume correction and resolution recovery methods using features from other imaging modalities have also been published [49, 103] with specific interest in this area for application with PET/MR scanners allowing for readily available spatially registered MR images acquired simultaneously with PET data [213]. Further investigations into applying these to spinal cord PET could prove advantageous, given the high resolution and tissue contrast available in the spine through MRI [214].

## 5.5 Conclusion

In this study we have demonstrated that in systems without time of flight, ignoring vertebral bone in PET/MRI leads to an underestimation in tracer uptake in the spinal cord of up to 23.9%, particularly in the thoracic spine. We have also demonstrated that for a system performance with a 4.4mm resolution, measured PET uptake in the spinal cord is reduced by up to 32.2% compared to higher resolution systems. We conclude that this is due to partial volume effects and has more impact on quantification than ignoring bone in attenuation correction. Applying TOF correction can reduce disparity in $SUV_{mean}$ between images reconstructed with and without vertebral bone included in attenuation maps to a range of 0.7% - 6.6%. Applying PSF modelling to both OSEM and TOFOSEM reconstruction methods requires a higher number of iterations than is often used in clinical practice to recover measured uptake, although reconstruction with the Q.Clear algorithm was able to recover more activity. More research is needed as to how best to apply partial volume correction in PET imaging to facilitate accurate quantification of PET tracer uptake in the spinal cord in PET/MRI.

# Chapter 6

# MR Guided PET Reconstruction for Spinal Cord PET/MRI.

## 6.1 Introduction

Anatomically guided PET reconstruction is a longstanding field of research in medical image reconstruction [30], with the algorithms made more feasible by the widespread use of combined PET/MR scanners. MRI can provide high resolution anatomical images with high contrast between different soft tissue structures, which can be utilised by MR-guided PET image reconstruction algorithms to improve localisation of PET activity and resolution recovery in PET images.

Several approaches have been developed for anatomically guided PET reconstruction which include anatomical information into an iterative reconstruction technique. The maximum *a posteriori* expectation maximisation (MAP-EM) algorithm [215] can be modified to include anatomical information from MR as a prior [216]. Bowsher et al proposed a method to incorporate an anatomical prior into Bayesian reconstruction algorithms [71] by computing edge information from an anatomical image to avoid over-smoothing across edges by the penalisation factors. This approach is popular, and has since been applied to MAP-EM reconstruction [67, 217]. Joint entropy (JE) or mutual information (MI) approaches [218] devise a similarity weighting between PET and MR information to further guide the penalty function in Bayesian reconstruction methods, making the algorithm more robust to mismatches between PET and MRI. Finally, kernel expectation maximisation (KEM) [74] and the hybrid kernel expectation maximisation (HKEM) [29] incorporate anatomical information into the more familiar maximum likelihood (ML) iterative algorithm by constructing a kernel matrix prioritising similarity between the image update and the kernel matrix.

Simultaneous acquisition of PET and MR improves spatial co-registration of images and reduces errors in anatomically guided image reconstruction [30, 219], while the inclusion of both PET and MR information into the image reconstruction process further reduces the impact of image misalignment between PET and MR [220, 221]. These methods have been shown to outperform partial volume correction applied post-reconstruction [217]. Many of these algorithms are demonstrated for use in brain PET/MRI [22, 67, 74, 216, 217], however, studies in the spinal cord are lacking. Conditions that affect the wider central nervous system (CNS) such as Multiple Sclerosis (MS) and Amyotrophic Lateral Sclerosis (ALS) warrant interest in imaging the spinal cord [95, 222], particularly as more CNS specific tracers continue to be developed [223].

The aim of this study is to establish whether using MR-guided PET reconstruction algorithms can improve the accuracy of measured uptake in the spinal cord, when compared to commonly used algorithms OSEM and Q.Clear. The secondary aim is to determine whether MR-guided PET reconstruction leads to an improvement in PET image quality compared to OSEM and Q.Clear reconstructed images.

In this study, we present the first results in applying MR-guided reconstruction algorithms to spinal cord imaging in PET/MRI. We investigate use of the HKEM algorithm [29] in the STIR software package [27]. This algorithm has previously been shown to improve the image quality for PET images of the carotid arteries [29] and aortic aneurysms [3], which are both small structures in areas of relatively high background activity.

We also demonstrate the use of MR-guided PET image reconstruction on clinical PET/MR data using an algorithm developed by GE Healthcare in their offline PET image reconstruction software Duetto (GE HealthCare). This algorithm is an implementation of a Bowsher's prior [71] modified to incorporate both PET and MR data through the calculation of a similarity coefficient between the PET and MR images, and incorporated into the existing Bayesian penalised likelihood reconstruction algorithm, Q.Clear [68].

## 6.2 Methods and Materials

### 6.2.1 Simulation

The XCAT mathematical phantom (version 2) [192] was used to generate [$^{18}F$]FDG tracer distributions of organs in the neck and thorax for a single 25cm field of view based on reported uptake in healthy subjects [101, 200–202, 224]. We used the XCAT standard male and standard female phantoms. Phantoms were simulated

to a voxel size of $2.1 \times 2.1 \times 2.8\text{mm}^3$. 511keV photon attenuation maps were also generated for the region by the XCAT software. Attenuation maps were scaled to units $cm^{-1}$. Modified attenuation maps were also generated to simulate those derived from Dixon MRI sequences, which was achieved by replacing all bone linear attenuation coefficients $\geq 1.2cm^{-1}$ with a muscle linear attenuation coefficient of $0.99cm^{-1}$ [14].

An anatomical MR image of the XCAT phantom was simulated by assigning pixel intensity values for major tissue types in T2-weighted MR images, as measured from a sagittal T2-weighted FSE image acquired on-site, to the XCAT phantom in place of organ activity values for the spinal cord, bone marrow, cortical bone, and lung, then assigning a single fat or muscle image pixel intensity to all other organs and tissues within the field of view. A prior with just the spinal cord segmented from the synthetic MR was also created for each phantom.

To perform simulations at a scanner detector resolution representative of a clinical PET/MRI scanner, the average distance of the spinal cord to the image centre was measured on patient acquisitions so that NEMA performance results for the scanner could be used to determine an appropriate resolution for the simulation representative of spinal cord acquisitions. From an average distance of 2.4cm, a transaxial resolution of 4.4mm and an axial resolution of 6mm, which was simulated by applying a 3D Gaussian filter to the generated XCAT activity distributions and attenuation maps using ImageJ [205].

Each XCAT distribution was forward projected using SIRF (version 3.4.0) [28] to generate a sinogram of the distribution. Attenuation correction factors (ACFs) were obtained from the attenuation maps with bone attenuation coefficients present, and scatter was calculated using the Single Scatter Simulation (SSS) algorithm in STIR (version 5.0.2) [27]. The XCAT activity, ACF and scatter sinograms were combined for sinograms simulating acquired PET data [204]. Poisson noise was added to sinogram data by scaling the number of counts in the sinogram to a value representative of the acquired PET and randomly drawing samples from a Poisson distribution. The sinogram was then scaled back to the original number of counts prior to image reconstruction. Time of flight information was not included in simulated data.

ACFs and scatter were also calculated for the attenuation maps without bone to be used during image reconstruction. Simulated sinograms were reconstructed using an Ordered Subset Expectation Maximisation (OSEM) algorithm (28 subsets, 10 iterations, voxel size $2 \times 2 \times 2.8\text{mm}^3$) with attenuation and scatter correction. Image reconstruction for each phantom was performed twice: once with attenuation and scatter correction calculated from the attenuation map with bone and

once with corrections calculated from the attenuation map without bone. Point spread function (PSF) modelling was not included. A 5mm Gaussian filter was applied post-reconstruction as this is often used in the clinical setting.

HKEM image reconstruction (28 subsets, 10 iterations, voxel size $2 \times 2 \times 2.8\text{mm}^3$) was performed with the simulated T2-weighted MR image provided as a prior for the reconstruction kernel and uses the attenuation map without bone features for attenuation and scatter correction. One of the previous publications using the HKEM algorithm segmented the organ of interest from MR images before using them as a prior [220]. To determine whether the prior should have the organ of interest segmented out first, reconstructions were also performed using just the spinal cord segmented from the synthetic T2 MRIs. Parameters for the kernel used were varied to determine the optimal parameters for most uptake measured. $\sigma_{dm} = 3$, $\sigma_{dp} = 3$ where kept consistent, but $\sigma_m = 0.1, 1$, $\sigma_p = 0.1, 0.5, 1$, and neighbourhood size $N = 3, 5$ were tested, where $\sigma_m$ and $\sigma_{dm}$ are scaling factors for the MR part of the kernel and $\sigma_p$ and $\sigma_{dp}$ are scaling factors for the PET part.

### Analysis

5mm spherical ROIs were drawn in the spinal cord at each vertebral level corresponding to vertebra C1 to T5. Mean activity and standard deviation were measured for each ROI.

Contrast to noise ratio (CNR) and Coefficient of Variation (CoV) were used as image quality metrics. CNR is calculated as

$$CNR = \frac{s - b}{\sqrt{SD_s^2 + SD_b^2}} \tag{6.1}$$

where s is the mean value in the spinal cord ROI, b is the mean value in the reference region. $SD_s$ and $SD_b$ are the standard deviation in the spinal cord ROI and the reference region respectively. CoV is

$$CoV = \frac{\sigma}{\mu} \times 100 \tag{6.2}$$

where $\sigma$ is the ROI standard deviation and $\mu$ is the ROI mean. CNR and CoV were calculated from results averaged across all spinal cord ROI. A 10mm ROI in the aortic arch was used for the reference region. The aortic arch was chosen as a reference region due to being the only blood pool region within the field of view, as other more common reference regions such as the liver and cerebellum were not simulated as part of this study. Wilcoxon signed rank test was used to determine

the statistical significance of results, as this analysis is suitable for non-parametric paired data. Results are considered statistically significant where $P < 0.05$.

### 6.2.2 Clinical Acquisition

Imaging was performed on the SIGNA PET/MR scanner (GE HealthCare Inc.) in accordance with the Declaration of Helsinki, with ethics committee approval and all participants gave written informed consent. Two participants, a healthy volunteer and an ALS patient, were administered 250MBq [$^{18}F$]FDG bolus injection 60 minutes before acquisition. PET data was acquired at two bed positions for 10 min each in head-first supine orientation. MRI was performed simultaneously to PET using the body coil for the dedicated attenuation correction Dixon and Zero Echo Time (ZTE) sequences, as well as the following anatomical sequences using a head and neck coil: axial T1-weighted Fast Spin Echo (FSE) and Axial T2-weighted FLAIR (Fluid Attenuated Inversion Recovery) for the brain, and sagittal T2-weighted FSE, Sagittal T1-weighted FLAIR of the spinal cord.

PET image reconstruction was performed offline using the vendor-provided software Duetto version 02.19 using an MR guided list-mode reconstruction algorithm with TOF Q.Clear. The penalisation factor for Q.Clear, beta ($b$), is user defined and was set to 0. An initial PET seed is reconstructed with OSEM (30 subset, 1 iteration) and the Sagittal T1- and T2-weighted spine MR images are used to generate a similarity coefficient for assigning voxel neighbourhoods. Subsequent image updates apply Q.Clear with noise suppression over pixel neighbourhoods defined using the similarity weighting between PET and MR anatomical images. Areas of the PET field of view for which no anatomy is provided are reconstructed by the Q.Clear algorithm with no additional weighting or penalisation except beta as a user defined parameter. TOF Q.Clear with $b = 200$ was used for comparing algorithm performance. Both of these algorithms include PSF correction.

Reconstructions were also performed using the TOF Q.Clear algorithm for comparison, with $b$ = 0, 100, 200, and 400, all of which are initialised using a 2 iteration OSEM reconstruction.

#### Analysis

Activity is normalised to body weight and displayed as Standardised uptake values ($SUV_{bw}$), which is used in all results presented for this part of the study. Regions of interest (ROIs), 5mm in diameter, were drawn in the spinal cord at each vertebral level on the T2 weighted MRI from C1 to T6 and used to calculate mean SUV ($SUV_{mean}$) and standard deviation for each ROI in the PET images.

$SUV_{bw}$ was averaged over the datasets and a linear regression was performed to demonstrate the trend of activity along the length of the spinal cord. Wilcoxon signed rank test was used to determine the statistical significance of results. CNR and CoV were also calculated using a reference region in the aortic arch.

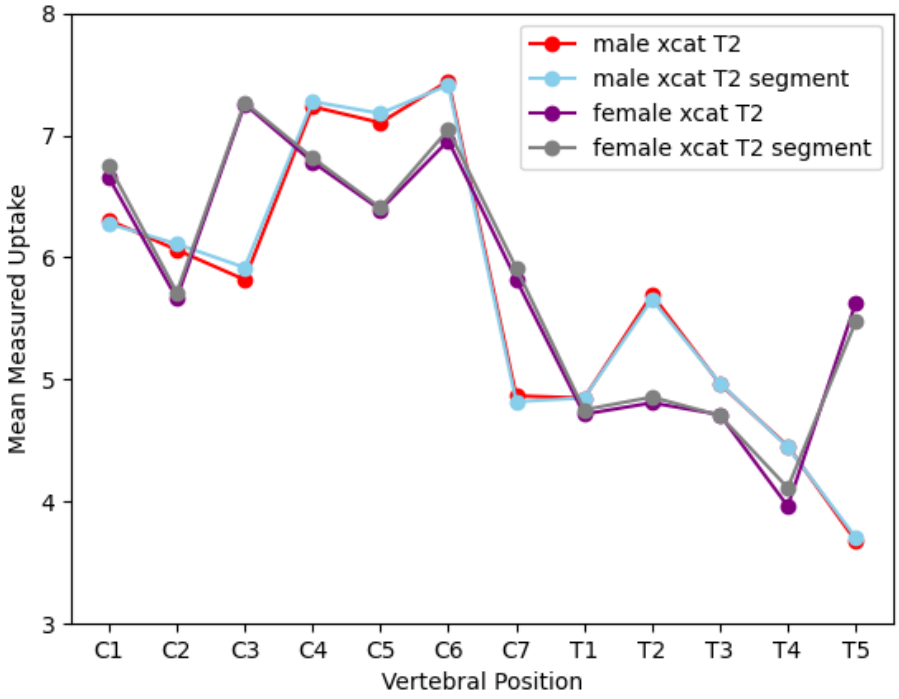


**Figure 6.1**: A graph showing the effect of different T2 MR priors on measured PET uptake in the spinal cord for the male and female XCAT phantoms.

## 6.3 Results

### 6.3.1 XCAT Simulations

No difference was found between using the synthetic T2 MR as a prior compared to segmenting out the spinal cord first, as show in figure 6.1. Graphs showing the difference in uptake measurements for the XCAT phantoms are displayed in figures 6.2 and 6.3. Changing $\sigma_m = \sigma_p = 0.1$ reduced uptake measured at some vertebral positions compared to $\sigma_m = \sigma_p = 1$, but made no significant difference to results (Male XCAT phantom $p = 0.3$, female XCAT phantom $p = 0.06$). Similarly, setting $\sigma_p = 0.5$ with $\sigma_m = 0.1$ made no apparent difference to uptake measurement compared to $\sigma_m$=$\sigma_p$=1 (Male XCAT phantom $p = 0.09$, female

XCAT phantom $p = 0.06$). Therefore, $\sigma_m$=$\sigma_p$=1 was chosen as the optimal HKEM reconstruction values for comparison with OSEM in line with previously reported results [3]. Increasing the number of voxels in the voxel neighbourhood N from 3 to 5 reduced measured uptake along the length of the spinal cord (Male XCAT phantom $p = 0.04$, female XCAT phantom $p = 0.02$). This is to be expected, as this permits smoothing over a large area of voxels, which improves image quality metrics whilst smoothing the signal intensity over the larger neighbourhood. As a result, N=3 was chosen as the optimal value for HKEM reconstructions.

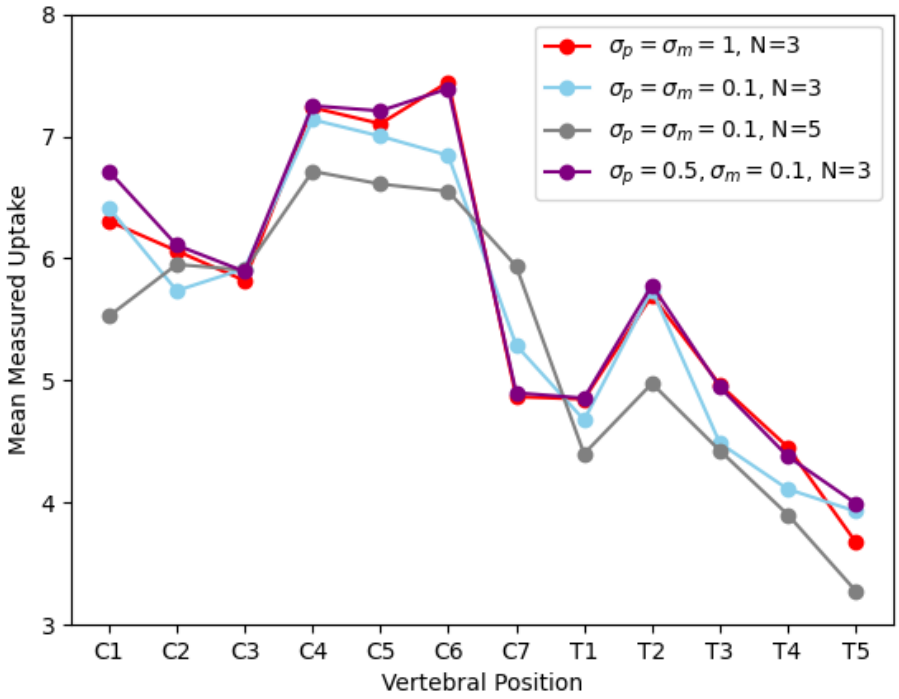


**Figure 6.2**: A graph showing the effect of different HKEM parameters on measured PET uptake in the spinal cord for the male XCAT phantom.

Images of both XCAT phantoms with OSEM and HKEM algorithms, and difference images are presented in figure 6.4. HKEM reconstructions appear markedly different to OSEM reconstructions, particularly in noise present across the entire image, which is shown in rows A and C of figure 6.4. However, when compared to post-filtered OSEM reconstructions, the difference between images is reduced and remains predominantly in the areas of the brain, with slight difference visible in the spinal cord (rows B and D of figure 6.4). However, this could be a reflection of the fact that both images have much less noise and lower coefficient of variation than the OSEM reconstructed images without post-filtering, given that the images

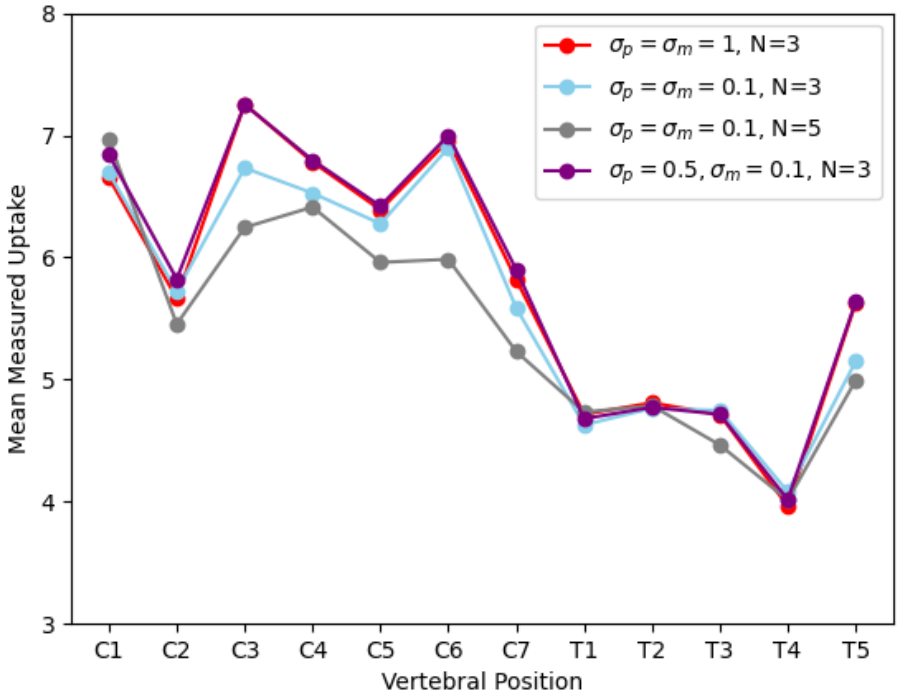


**Figure 6.3**: A graph showing the effect of different HKEM parameters on measured PET uptake in the spinal cord for the female XCAT phantom.

themselves show different quantitative values for spinal cord ROIs in figure 6.5 and 6.6.

Analysis of measured activity uptake in the spinal cord showed an average increase in measured uptake of 3.9% in the HKEM male XCAT phantom image compared to OSEM, and a maximum of 12% increase at T3, visible in figure 6.5. Differences were statistically significant with a p-value of $p = 0.03$. Image quality metrics are displayed in table 6.1, and are improved in the HKEM image ($CNR = 0.86$, $CoV = 17.7\%$) compared to OSEM ($CNR = 0.31$, $CoV = 46.1\%$). Image quality metrics are further improved for post-filtered OSEM images ($CNR = 2.2$, $CoV = 5\%$), however the dashed line in figure 6.5 shows that measured uptake is decreased throughout the spinal cord in these images.

In the female XCAT phantom, the average increase in measured uptake is overall much smaller, with an average increase of 0.7% in measured uptake in the HKEM image, despite the larger maximum increase of 18.4% at C1. This is shown in graph B of figure 6.6, which also demonstrates that in the female phantom, measured uptake in the HKEM is generally increased in the cervical spine compared to OSEM, but decreased in the thoracic spine ($p = 0.62$). Image quality metrics

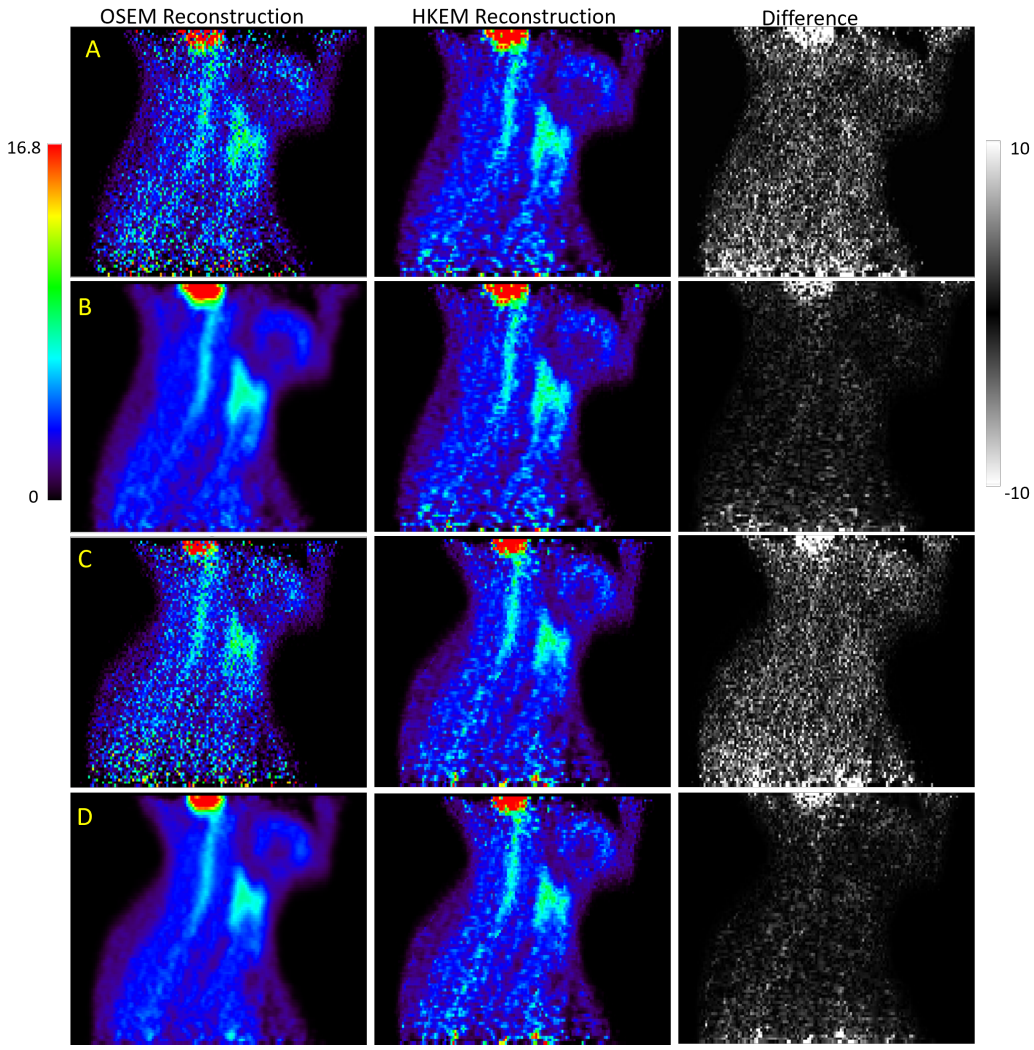


**Figure 6.4**: Images of the XCAT male (rows A,B) and female (rows C,D) phantoms reconstructed with OSEM (first column) and HKEM (second column). Rows B and D show post-filtered reconstructed OSEM images. The last image in each row shows the difference between OSEM and HKEM reconstruction.

| **Reconstruction Algorithm** | **Average CNR** | | **Average CoV** | |
|---|---|---|---|---|
| | Male XCAT | Female XCAT | Male XCAT | Female XCAT |
| OSEM | 0.3 | 0.6 | 46% | 36% |
| OSEM + Post Filter | 2.2 | 3.9 | 5% | 5% |
| HKEM | 0.9 | 1.5 | 18% | 16% |

**Table 6.1**: Image quality metrics in reconstructed PET images of the XCAT phantoms for OSEM, Post-filtered OSEM and HKEM algorithms, for ROIs in the spinal cord.

are also improved in the HKEM image ($CNR = 1.52$, $CoV = 15.7\%$) compared to OSEM ($CNR = 0.59$, $CoV = 35.9\%$) for the female XCAT phantom. Similarly to the male XCAT phantom, image quality metrics are furthered improved through post-filtering OSEM image reconstructions ($CNR = 3.9$, $CoV = 5\%$), however quantitative accuracy is once again reduced in figure 6.6.

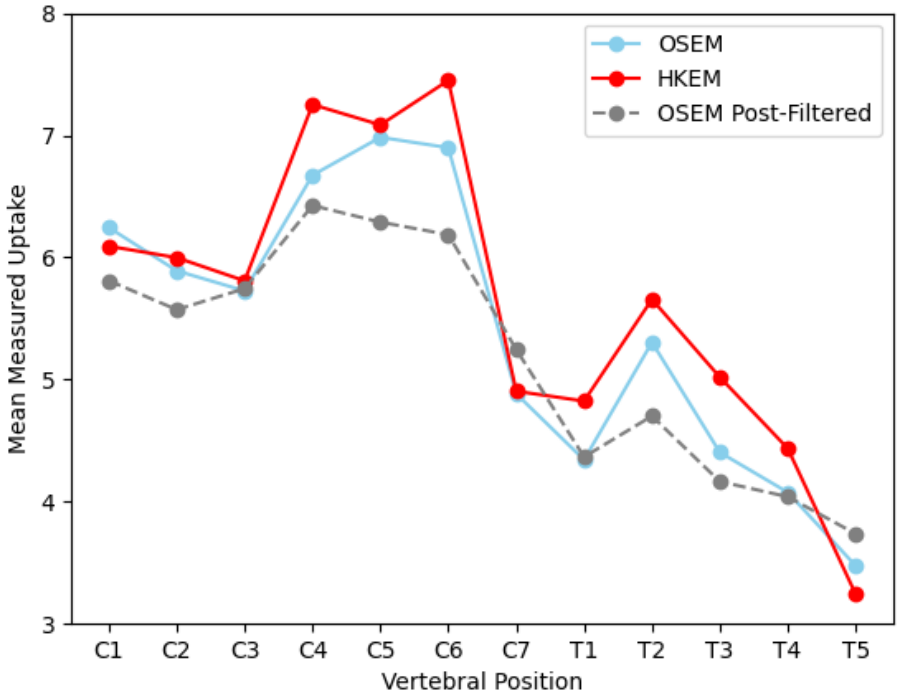


**Figure 6.5**: A graph showing measured uptake along the spinal cord for the male xcat phantom in OSEM, Post-filtered (5mm Gaussian) OSEM and HKEM images. All images are attenuation and scatter corrected using an attenuation map without bone, simulating an MR derived attenuation map.

When post-filtering is applied to OSEM images, measured uptake is reduced compared to both OSEM without post-filtering and HKEM reconstructed images in both phantoms. In the male phantom, measured uptake in the HKEM reconstructed image is an average of 4.6% higher ($p = 0.02$, maximum increased uptake 29.6% at C6) and in the female phantom by an average of 7.4% ($p = 0.002$, maximum increased uptake 19.6% at T5). These results are displayed as a dashed line in figure **??**. CNR for the post-filtered OSEM images is lower than the HKEM reconstructed image for the male XCAT phantom ($CNR = 0.7$), but not the female XCAT phantom ($CNR = 3.9$). However, CoV is lower in post-filtered OSEM images the HKEM reconstructed images in both cases (male phantom: $CoV = 4.4$,

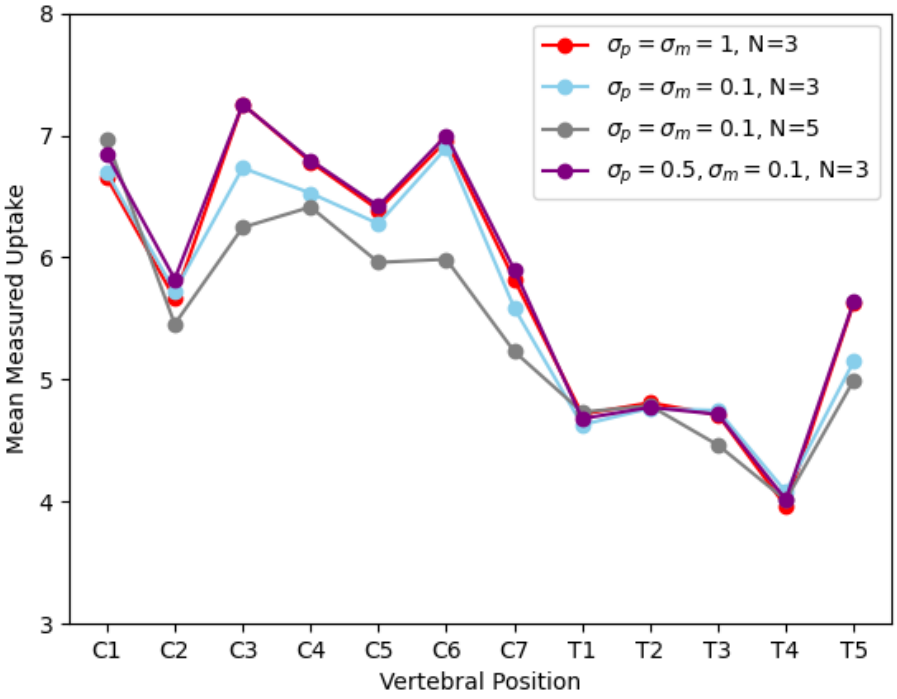


**Figure 6.6**: A graph showing measured uptake along the spinal cord for the female xcat phantom in OSEM, Post-filtered (5mm Gaussian) OSEM and HKEM images. All images are attenuation and scatter corrected using an attenuation map without bone, simulating an MR derived attenuation map.

female phantom: $CoV = 4.8$).

The spinal cord isn't at a fixed distance from the isocentre for it's full length. As resolution varies across the PET field of view, decreasing with transaxial distance from the isocentre [140], we have shown how uptake changes with ROI displacement from the centre of the field of view in the transaxial plane in figure 6.7 and6.8. Both phantoms show a decrease in measured uptake with increasing distance from the image centre, and in figure 6.7, it appears that HKEM recovers activity well in the distal ROIs, however this isn't demonstrated for both cases. These graphs show an expected pattern of uptake, as the spinal cord is further from the isocentre as it moves along the thoracic spine. A reduced uptake along the length of the thoracic spinal cord is expected as the cord diameter is smaller in this region compared to the cervical spine [34].

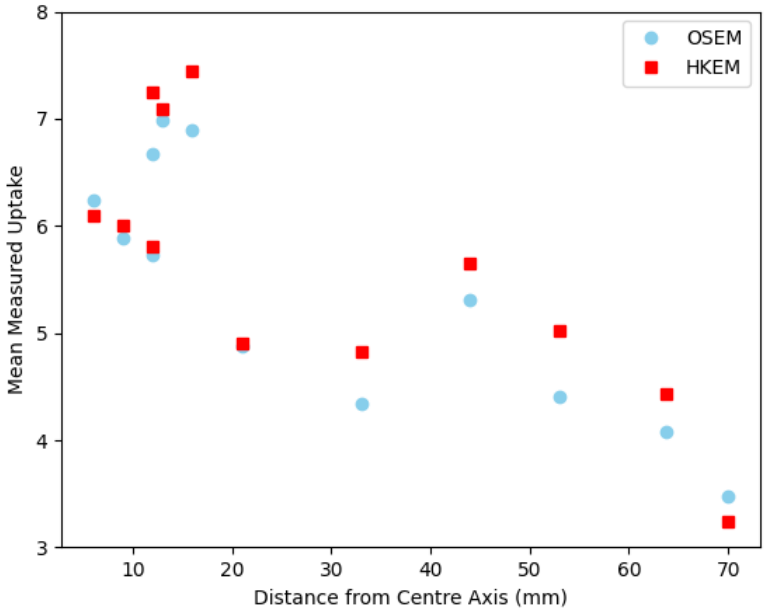


**Figure 6.7**: A graph showing measured uptake in the spinal cord for the male xcat phantom against ROI displacement from the centre of the field of view transaxially.

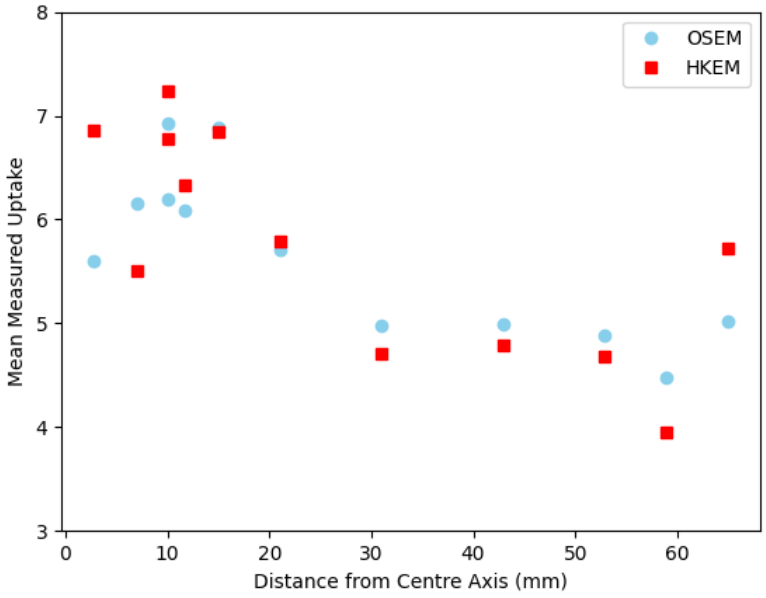


**Figure 6.8**: A graph showing measured uptake in the spinal cord for the female xcat phantom against ROI displacement from the centre of the field of view transaxially.

### 6.3.2 Clinical Acquisitions

Images of both clinical subjects reconstructed with TOF Q.Clear and MR-guided Q.Clear are displayed in figure 6.9. The MR-guided reconstructed images maintain the noise suppression provided by Q.Clear, but visibly enhance anatomical edges of the spine and spinal cord. As a result, resolving between bone marrow uptake and spinal cord uptake in the thoracic spine is visually clearer in image C of both figures compared to images A or B.

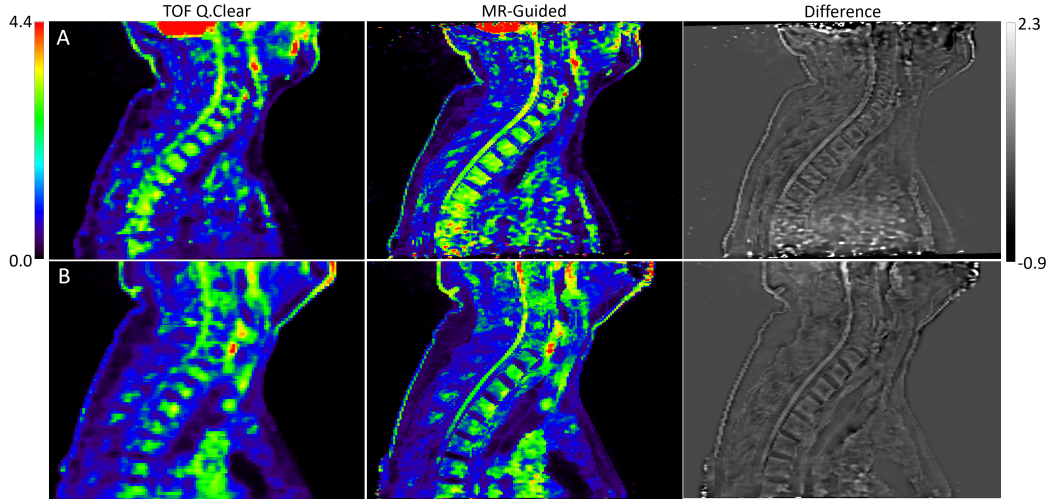


**Figure 6.9**: [$^{18}F$]FDG PET images of a volunteer (row A) and Amyotrophic Lateral Sclerosis (ALS) patient (row B) reconstructed with TOF Q.Clear, MR-guided TOF Q.Clear and showing a difference image betweens the reconstruction algorithms.

Given the difference in HKEM performance during the simulated study between the male and female phantom presented in 6.3.1, results here are also segregated with graphs showing $SUV_{mean}$ against vertebral position presented for both subjects in figures 6.10 and 6.11. However, in both cases the MR-guided reconstruction shows an increased uptake in the spinal cord when compared to TOF Q.Clear (average increase in measured uptake: 24.7%, $p \leq 0.001$ and 50.6%, $p \leq 0.001$) reconstructed images. This is demonstrated by looking at plots of $SUV_{mean}$ averaged over both patients in figure 6.12, where the higher quantification in MR guided reconstruction is seen compared to TOF Q.Clear for comparable values of beta ($p = 0.49$).

As demonstrated in the XCAT phantom, both the patient and volunteer show a decrease in $SUV_{mean}$ in ROIs measured further from the centre of the field of view, show in figures 6.13 and 6.14. In both cases, MR guided reconstruction is able to recover more activity in distal ROIs than TOF Q.Clear, and this is particularly prominent in figure 6.13.

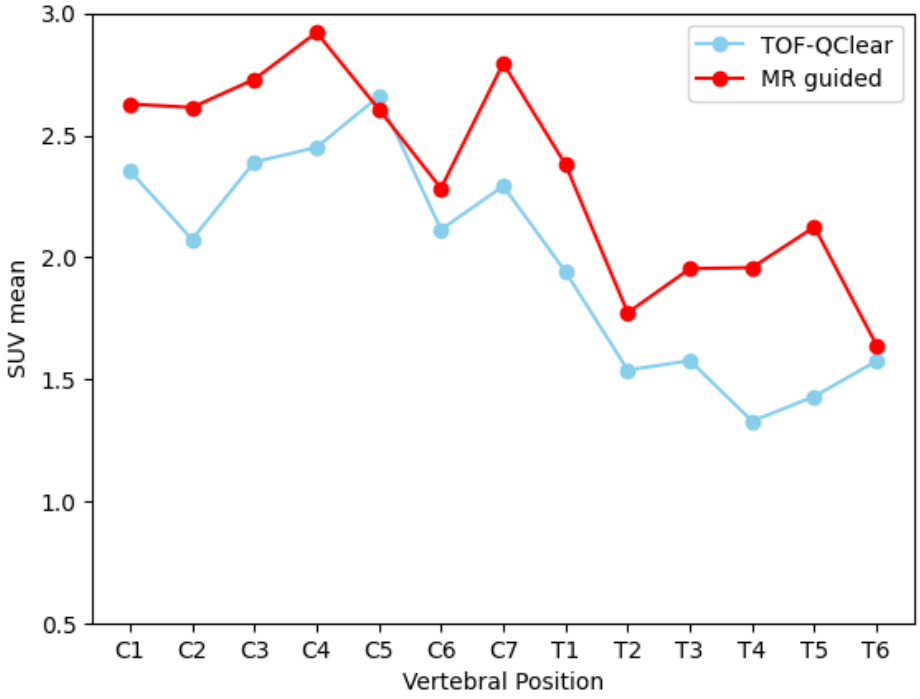


**Figure 6.10**: A graph showing $SUV_{mean}$ along the spinal cord in a volunteer reconstructed with TOF Q.Clear and MR guided TOF Q.Clear algorithms.

Only one subject had the reference region within the MR field of view, so image quality metrics are only reported here for those datasets, displayed in table 6.2. At an average CNR of 1.94, the MR-guided reconstruction outperforms a comparable TOF Q.Clear with $b = 0$ (CNR = 1.00), but higher $b$ gives a higher CNR. CoV is higher also higher (CoV = 19%) than TOF Q.Clear with $b = 0$ (CoV = 43%) and comparable to $b = 100$ (CoV = 19%), indicating that MR guidance is reducing image noise.

| Reconstruction Algorithm | Average CNR | Average CoV |
|---|---|---|
| TOF Q.Clear ($b = 0$) | 1.00 | 43% |
| TOF Q.Clear ($b = 100$) | 2.32 | 19% |
| TOF Q.Clear ($b = 200$) | 3.42 | 12% |
| MR Guided TOF Q.Clear | 1.94 | 19% |

**Table 6.2**: Image quality metrics for a clinical acquisition reconstructed with TOF Q.Clear ($b = 0, 100, 200$) and MR-guided Q.Clear, for ROIs in the spinal cord.

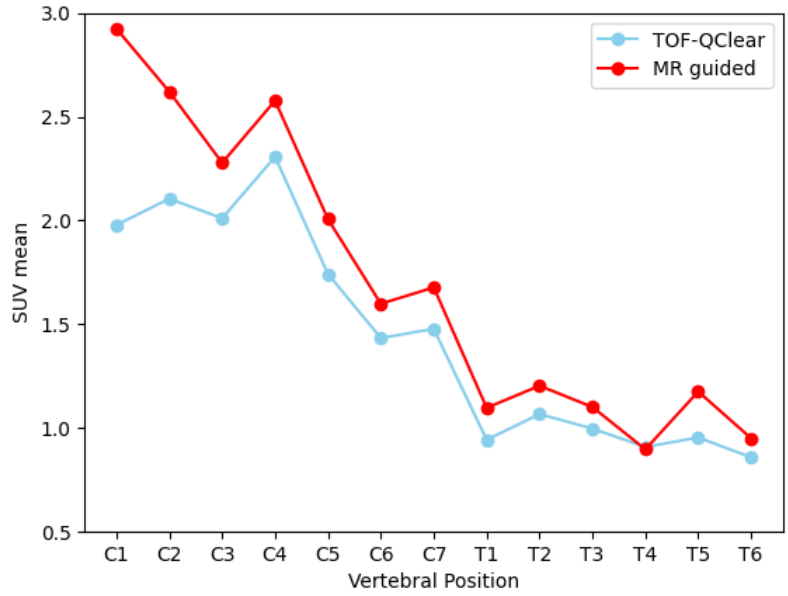


**Figure 6.11**: A graph showing $SUV_{mean}$ along the spinal cord in an ALS patient reconstructed with TOF Q.Clear and MR guided TOF Q.Clear algorithms.

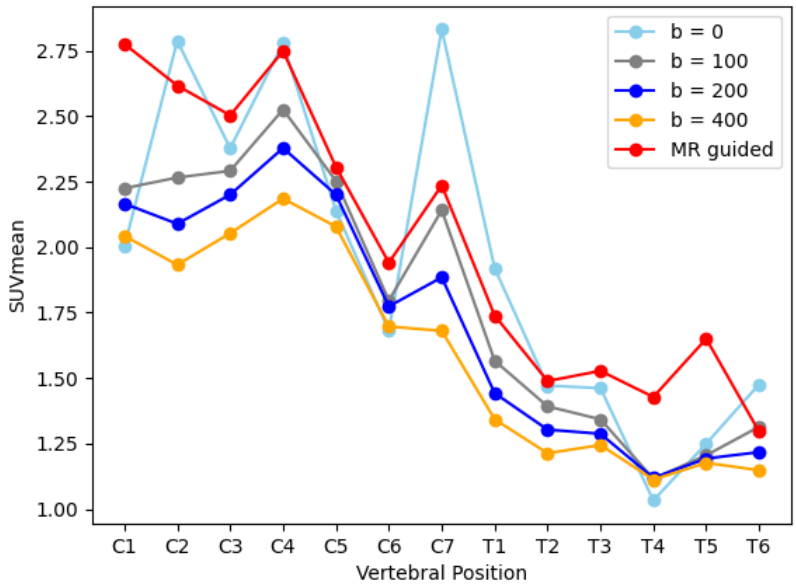


**Figure 6.12**: A graph showing the average $SUV_{mean}$ along the spinal cord when reconstructed with TOF Q.Clear for different $b$ values and MR guided TOF Q.Clear ($b = 0$).

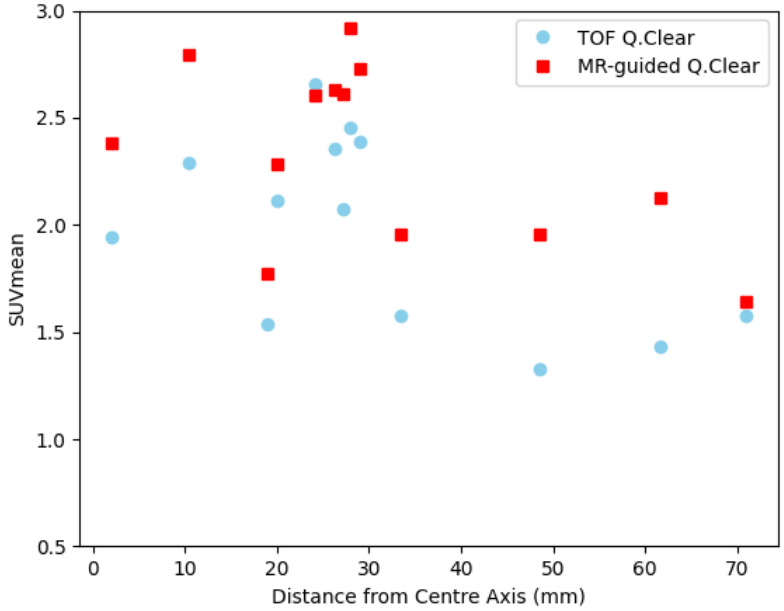


**Figure 6.13**: A graph showing $SUV_{mean}$ along the spinal cord in a volunteer against ROI displacement from the centre of the field of view transaxially.

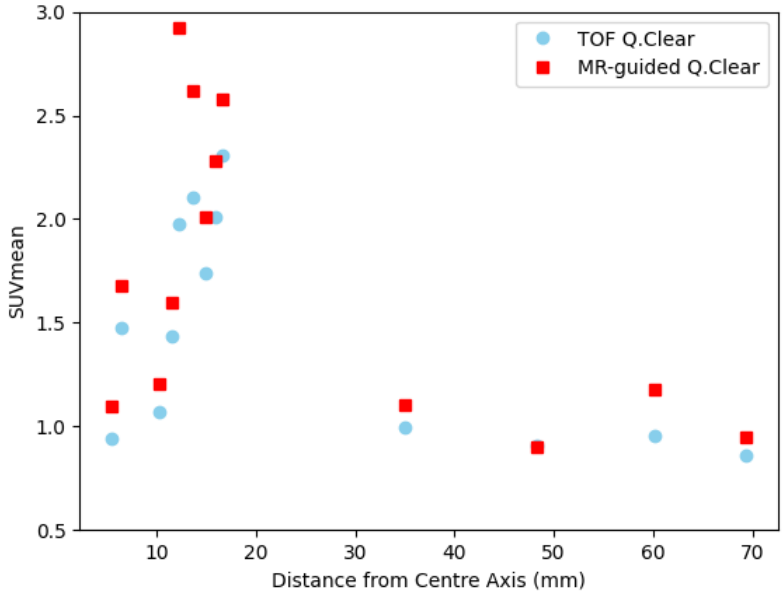


**Figure 6.14**: A graph showing $SUV_{mean}$ along the spinal cord in an ALS patient against ROI displacement from the centre of the field of view transaxially.

## 6.4 Discussion

### 6.4.1 XCAT Simulations

In optimising the HKEM algorithm for measuring tracer uptake in the spinal cord, we opted for a smaller voxel neighbourhood for the kernel of $N = 3$ compared to previous studies where image quality metrics were prioritised [3]. However, other changes to parameters made only small differences to both measured uptake and image quality metrics. As the HKEM algorithm is still establishing use cases, there's a lot to be explored here in balancing MR and PET kernel contributions to each image update given the many possibilities permitted for unequal weighting of the factors.

Significant improvement to measured uptake compared to OSEM was observed in the male phantom. HKEM also shows a good recovery of activity both near the centre of the field of view, and in more distal ROIs in the transaxial plane, despite a known decrease in detector resolution with distance from the isocentre. In figure 6.6 it appears that HKEM underestimates spinal cord activity most in the thoracic spine of the female phantom. This is region of the spinal cord has a smaller diameter compared to the cervical spine. No previous patient studies in adults have shown sex differences in spinal cord uptake for [$^{18}F$]FDG PET [26], but aspects of the different phantom models and how they are set up could be a factor. For example, uptake of vertebral bone marrow has previously been reported to affect measured spinal cord activity [101] due to it's close proximity to the spinal cord. Both XCAT phantoms were assigned organ activity values previously reported in literature [101, 200–202, 224], which leads to the female XCAT phantom having a higher activity assigned to the vertebra and bone marrow than the male phantom, whilst spinal cord uptake is slightly lower. Additionally, the skeletal volume of the spinal column is smaller in the female XCAT phantom [192], so bone marrow is also be closer to the spinal cord.

In the optimised results, post-filtering OSEM reconstructed images gave the highest image quality metrics, however, the test with an $N = 5$ voxel neighbourhood size indicate comparable performance to the filter chosen. This highlights the necessity in choosing HKEM reconstruction parameters according to the desired application and is in line with previous studies [3, 29]. Note that performance in image quality metrics doesn't necessarily indicate that these are the optimal image reconstruction parameters, particularly where we're considering noise reduction. In the results presented, despite reduced noise and increased CNR, the post-filtered images lose quantitative accuracy. Quantification of tracer uptake is a crucial measure in PET for both clinical and research applications, and must be

considered when choosing optimal PET image reconstruction parameters.

### 6.4.2 Clinical Acquisitions

MR guided PET image reconstruction as implemented in Duetto, and with the parameters used in this study, gives an increased $SUV_{mean}$ in the spinal cord compared to the currently implemented TOF Q.Clear algorithm. Given the results demonstrated in the simulation section of this study, it can be inferred that the increased uptake measured in the MR-guided reconstructions represent an increase in accuracy towards measuring true uptake. In figure 6.13 MR-guided reconstruction showed a greater increase in $SUV_{mean}$ for distal ROIs, which could be attributed to resolution recovery by inclusion of the MR prior, as counts further from the PET isocentre are imaged with lower intrinsic resolution [140].

The edge preservation mechanism creates images that appear sharper, however there is a risk of losing PET unique features in the image if these parameters are not appropriately weighted [67]. This occurs more frequently where PET activity crosses the boundaries of MR features [220]. Generally, this would not be expected in spinal cord imaging due to low uptake of $[^{18}F]$FDG in cerebral spinal fluid (CSF) [101], indicating that MR guided reconstruction presents a benefit to spinal cord PET/MR. Here we used parameters largely tested on brain images previously, so additional work is still needed to optimise reconstruction parameters for spinal cord imaging, particularly the weighting of MR and PET priors. Overall, the reduction in noise and improved resolution at tissue boundaries is a much more pronounced effect than observed in the study performed using the HKEM algorithm with the XCAT phantom. Whilst these are not directly comparable due to the fact two different algorithms are assessed, the parameters chosen for MR guided Q.Clear weight the MR anatomical contribution are very highly weighted to demonstrate the algorithms utility in image quality improvements, and may not reflect the optimal parameters for PET clinical and research use.

When compared to TOF Q.Clear, CNR and CoV are improved when MR guidance is used for comparable beta value. This means that noise is reduced in the resulting PET images despite increasing sharpness at tissue boundaries, which is beneficial for imaging small structures that can become overly smoothed when reducing noise in PET imaging [76]. There is potential to investigate a combination of the choice of $b$ with different PET and MR prior weightings.

MR guided reconstruction was applied retrospectively to data that had already been acquired in this study, however, an investigation into the impact that the chosen MR acquisitions have on reconstructions would also be beneficial. Due to having only acquired spinal cord images typical in clinical imaging for Amyotrophic

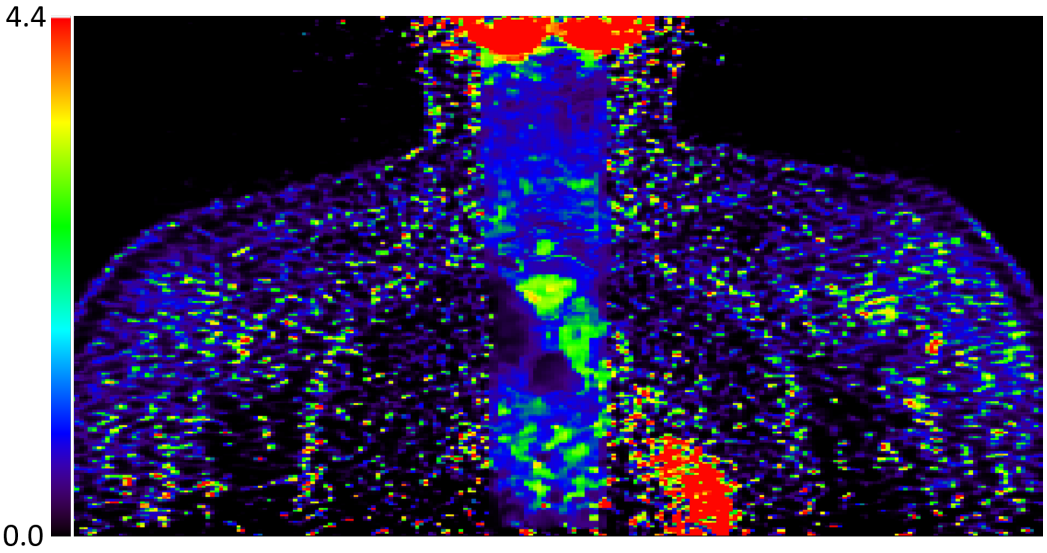


**Figure 6.15**: An example of MR guided PET image reconstruction viewed in the coronal plane, showing regions where the MR prior doesn't cover the full PET field of view. Outside of MR coverage, the PET image is noisy and unclear.

Lateral Sclerosis (ALS) [78], this study used sagittal MRI with low resolution in the axial plane and a field of view restricted to the spine itself. The parameters chosen in this study compromise the PET image outside the MR field of view, which is more apparent when viewing other image planes such as the coronal displayed in figure 6.15. Therefore either a large field of view MR sequences would be needed to cover all anatomy, or the weighting of the MR prior may be too high if we are unable to resolve PET features without it. Increasing $b$ may also reduce noise outside the MR field of view to present clearer images. For some applications it may be reasonable to reconstruct both a TOF Q.Clear for the full field of view to assess wider anatomy, whilst using MR guided reconstruction to focus on an organ of interest.

### 6.4.3 Limitations

STIR doesn't have robust PSF modelling for PET data reconstruction, limiting the resolution recovery of reconstructions performed within the framework. It would help to improve partial volume effect by utilising both HKEM and PSF modelling. The GE Healthcare PET Toolbox includes PSF modelling in MR guided PET reconstruction, so this limitation no longer applies to these images.

By assigning the XCAT phantom PET tracer uptake from values reported previously reported in PET imaging, the values assigned will have been affected by

partial volume errors and attenuation correction errors that have been identified in this thesis. This means that we may be propagating some effects in the simulated data. For example, if measured uptake is reduced in the spinal cord due to partial volume effect, then our XCAT phantoms are already starting out the study with lower activity than a true uptake value. However, these values were taken from a range of sources [101, 200–202, 224] and act as representative activity distributions in the absence of histological values.

Hybrid image reconstruction algorithms can be prone to artifacts where PET and MRI are misaligned, which in the torso may occur due to both bulk and physiological motion [210], as MR sequences often take less time to acquire than PET. Therefore, motion correction may also be required in addition to PSF modelling. However, HKEM has been demonstrated to by more robust to small misalignment between PET data and anatomical imaging than previous MR guided reconstruction algorithms [220, 221] due to the dependence of the kernel on PET iterative updates in addition to anatomical MR, and similarly the MR Guided Q.Clear algorithm allows users to select appropriate weightings for both PET and MR image contributions to the penalisation term.

## 6.5 Conclusion

We have demonstrated that two algorithms, HKEM and GE HealthCare's MR guided reconstruction, both lead to an increase in measured [$^{18}F$]FDG PET tracer uptake in the spinal cord. With care taken to optimise for the desired application, novel PET image reconstruction algorithms using PET and MR data to inform iterative image updates lead to improved quantification and improved image quality compared to OSEM. Further work is needed to investigate the optimal parameters and assessing their performance over a greater number of acquisitions.

# Chapter 7

# Overall Conclusion and Future Outlook

## 7.1 Conclusions

The overall objective of this thesis was divided into three main questions to be addressed, the outcomes of which allow for an overarching conclusion of this work to be drawn.

**Aim 1: Do phantoms exist that are capable of replicating tissue properties and anatomical geometry of the spine and spinal cord for the performance assessment or PET/MR scanners?**

The literature review present in chapter 3 identified a large number of tissue mimicking phantoms that had been developed for the assessment of PET and PET/MR scanner performance for a range of clinical applications. However, many of these we in use only by the individual centres they were developed in, and weren't reproducible to other sites. It was mainly found that commercially available geometric phantoms saw the most widespread use. Based on this work, I set out a specification for the ideal tissue mimicking phantom of the spine and spinal cord, however this would have been a substantial project in itself to build and validate. As a results, a combination of experiments using the NEMA IEC Body Phantom, an anatomical phantom loaned from collaborators at the University of Leeds, and a computational phantom were used to assess the performance of the SIGNA PET/MR scanner and image reconstruction methods used in later chapters of the thesis.

**Aim 2: To what extent are attenuation correction and partial volume effect sources of error in PET images for spinal cord PET/MR?**

Phantom experiments performed on the SIGNA PET/MR scanner revealed a

high recovery of activity in larger sphere of the NEMA IEC Body Phantom, and the spinal cord surrogate on the anatomical head and neck phantom. However, this wasn't sustained in smaller spheres, and sphere sizes as measured from the full width half maxima of line profiles across the spheres indicated that sphere size was underestimated. Similarly, line profiles of the head and neck phantom showed activity within the spinal cord surrogate material was blurred into the background regions.

Through simulation study and clinically acquired data, it was established that removing vertebral bone from attenuation maps of the spine or inserting them into MR derived attenuation maps did not impact measured uptake in the spinal cord to a great extent, and was further minimised by the use of Time of Flight algorithms where TOF data is able to be acquired. However, incorporating Gaussian blurring into the initial data distribution prior to forward projection, simulating the point spread response of the detector, had a much greater effect on measured uptake in the spinal cord. The combination of results from the experiments described in chapters 4 and 5 lead to the conclusion that partial volume effect is a greater source of error in spinal cord PET imaging. As such, applying effective partial volume correction would have a greater impact in facilitating reliable spinal cord imaging in PET/MR going forward.

**Aim 3: Can MR guided PET image reconstruction reduce the impact of partial volume effects in spinal cord PET/MR?**

A number of partial volume correction approaches are available, however the ability to acquire highly spatially co-registered PET and high resolution, anatomical MR images is a benefit provided by the SIGNA PET/MR scanner. Post-reconstruction partial volume correction methods often increase noise in PET images, and the spinal cord is a low uptake region in [$^{18}$F]FDG PET relative to nearby structures. Therefore, MR guided PET reconstruction algorithms were chosen for PVC in spinal cord PET/MR. Two algorithms were assessed and found to have promising results, indicating an ability to both correct for partial volume effect and reduce noise in the spinal cord region compared to commonly used algorithms in most of the cases that were investigated.

The work presented in this thesis concludes that partial volume effects remain a dominant source of error when imaging the spinal cord due to its small diameter compared to achievable PET detector resolution. This has been the first assessment of the impacts of both attenuation correction and partial volume correction on PET images of the spinal cord acquired on the SIGNA PET/MR scanner.

MR guided PET image reconstruction was investigated as a means of applying

partial volume correction to PET data. In this preliminary work, MR guided PET image reconstruction from simultaneously acquired PET/MR data demonstrates improvements to image quality and quantification accuracy in two algorithms, HKEM and MR guided Q.Clear, when compared to OSEM and TOF Q.Clear respectively. This is the first time MR guided reconstruction algorithms have been used in spinal cord imaging, and assessed for their performance in reducing image noise and the impact of partial volume effects for this application.

## 7.2 Recommendations for Future Work

This thesis constitutes a preliminary investigation into MR guided PET image reconstruction for spinal cord PET/MR. Whilst results indicate that MR guided image reconstruction could reduce the impact of partial volume effect in PET images, there is more work needed before this could be widely applied to spinal cord PET/MR in clinical research.

Firstly, image reconstruction should be optimised for spinal cord imaging. Both HKEM and MR guided Q.Clear allow the user to fine tune the weighting of PET and MRI data used for reconstruction, as well as the degree of noise reduction through penalisation factors. More work is needed to find the optimal combination of parameters to balance accurate quantification with the desired noise reduction for visualising the spinal cord in PET images. An example of such a study for the abdominal aorta is presented in [3], where each parameter is assessed individually for it's impact on the desired image quality metrics before results for the abdominal aorta are presented as a whole.

Optimisation of the anatomical MR acquisitions used for MR guided PET reconstruction is also needed. High resolution, 3-dimensional isotropic imaging is often recommended for anatomically guided MR in brain imaging, however this isn't commonly acquired in abdominal imaging, and particularly not to the extent that the full PET field of view would be acquired. This was seen in chapter 6, where the MR Guided Q.Clear reconstruction was only performed where MR anatomical information was available, and the rest of the image wasn't at the same quality as TOF Q.Clear. If MR images for the full PET FOV were to be required, then dedicated MR sequences would need to be acquired for the MR guided reconstruction and a large field of view at high resolution would take a long time to acquire in MR. A solution to this is to use MR images from different planes, as MR guided Q.Clear permits any number of anatomical images to be used in addition to PET data inputs. This also allows for the use of different contrast weighted MR images, and may allow for existing clinically required images to be used and

reduce the amount of time needed to acquire dedicated MR anatomy for the MR guided reconstruction. Another solution could be to only use MR guided Q.Clear for specific organs of interest, with TOF Q.Clear used to reconstruct the full field of view for an overall PET image covering the rest of the acquisition.

For more widespread use, these methods would need to be validated on a larger number of datasets than are presented here. Ideally this would be a prospective study to enable any dedicated spinal cord imaging needed to be performed, however retrospective reconstruction of PET data could also be used for validation where anatomical MR acquisitions are available for the spine and spinal cord.

Additionally, it would be recommended to validate this for a range of tracers applicable to spinal cord imaging. Of particular interest out of the PET tracers used in the central nervous system would be [$^{18}$F]FET, for the assessment of CNS tumours [6], myelin protein binding tracers such as [$^{11}$C]MeDAS [86] and TSPO tracers [209, 223], used to identify areas of neuroinflammation. Additional considerations may be needed to account for positron range in radiotracers using isotopes such as [$^{82}$Rb] or [$^{68}$Ga], which see positrons travel further from their origin before an annihilation event occurs.

Finally, deep learning has previously been applied to MR guided image reconstruction for brain PET/MR [225]. Deep learning can accelerate image reconstruction and find optimal parameters for image reconstruction once trained and validated on sufficiently large datasets without requiring user input. However, deep learning methods highlights the necessity of ensuring MR acquisition parameters are carefully chosen with image reconstruction in mind, as previous work has found that simply using the highest resolution imaging available may not be optimal when used in synergistic reconstruction [226].

To be widely applicable, deep learning models need to be trained on a large dataset, ideally from a variety of institutions, patient populations and acquisition protocols to ensure the model generates accurate results for widespread general use. Evaluation and validation of models for widespread clinical use has been a downfall in AI research previously, however recommendations and guidelines are becoming available to facilitate the dissemination of deep learning models, an example of which is the Society of Nuclear Medicine and Molecular Imaging (SNMMI) RELIANCE (Recommendations for EvaLuation of AI for NuClear medicinE) guidelines [227].

# Bibliography


[1] P.Y. Patel, I. Dalal, and B. Griffith. [18F]FDG-PET Evaluation of Spinal Pathology in Patients in Oncology: Pearls and Pitfalls for the Neuroradiologist. *American Journal of Neuroradiology*, 43(3):332–340, 10 2021.

[2] H.H. Quick. Integrated PET/MR. *Journal of Magnetic Resonance Imaging*, 39 (2):243–258, 2 2014.

[3] D. Deidda, M.I. Akerele, R.G. Aykroyd, M.R. Dweck, K. Ferreira, R.O. Forsythe, W. Heetun, D.E. Newby, M. Syed, and C. Tsoumpas. Improved identification of abdominal aortic aneurysm using the kernelized expectation maximization algorithm. *Philosophical Transactions of the Royal Society A*, 379(2200), 6 2021.

[4] M.I. Vargas, J. Boto, and T.R. Meling. Imaging of the spine and spinal cord: An overview of magnetic resonance imaging (MRI) techniques, 8 2020.

[5] M. Aiello, V. Alfano, E. Salvatore, C. Cavaliere, M. Picardi, R. Della Pepa, E. Nicolai, A. Soricelli, A. Vella, M. Salvatore, and M. Mascalchi. [18F]FDG uptake of the normal spinal cord in PET/MR imaging: comparison with PET/CT imaging. *EJNMMI Research*, 10(1):91, 8 2020.

[6] L. Marner, K. Nysom, A. Sehested, L. Borgwardt, R. Mathiasen, O.M. Henriksen, M. Lundemann, P.M. Rosenschöld, C. Thomsen, L. Bøgeskov, J. Skjøth-Rasmussen, M. Juhler, A. Kruse, H. Broholm, D. Scheie, T. Lauritsen, J.L. Forman, P.S. Wehner, L. Højgaard, and I. Law. Early postoperative 18F-FET PET/MRI for pediatric brain and spinal cord tumors. *Journal of Nuclear Medicine*, 60(8):1053–1058, 8 2019.

[7] N.J. Shah, H. Herzog, C. Weirich, L. Tellmann, J. Kaffanke, L. Caldeira, E.R. Kops, S.M. Qaim, H.H. Coenen, and H. Iida. Effects of Magnetic Fields of up to 9.4 T on Resolution and Contrast of PET Images as Measured with an MR-BrainPET. *PLOS ONE*, 9(4):e95250, 4 2014.

[8] K. Bolwin, B. Czekalla, L.J. Frohwein, F. Büther, and K.P. Schafers. Anthropomorphic thorax phantom for cardio-respiratory motion simulation in tomographic imaging. *Physics in Medicine and Biology*, 63(3):035009, 2 2018.

[9] Y. Petibon, J. Ouyang, X. Zhu, C. Huang, T.G. Reese, S.Y. Chun, Q. Li, and G.E. Fakhri. Cardiac motion compensation and resolution modeling in simultaneous PET-MR: A cardiac lesion detection study. *Physics in Medicine and Biology*, 58(7):2085–2102, 4 2013.

[10] C. Huang, Y. Petibon, J. Ouyang, T.G. Reese, M.A. Ahlman, D.A. Bluemke, and G. El Fakhri. Accelerated acquisition of tagged MRI for cardiac motion correction in simultaneous PET-MR: Phantom and patient studies. *Medical Physics*, 42(2):1087–1097, 1 2015.

[11] J. Ceh, T. Youd, Z. Mastrovich, C. Peterson, S. Khan, T.A. Sasser, I.M. Sander, J. Doney, C. Turner, and W.M. Leevy. Bismuth infusion of ABS enables additive manufacturing of complex radiological phantoms and shielding equipment. *Sensors*, 17(3), 2 2017.

[12] A. Techawiboonwong, K.S. Hee, M.B. Leonard, and F.W. Wehrli. Cortical bone water: In vivo quantification with ultrashort echo-time MR imaging. *Radiology*, 248(3):824–833, 9 2008.

[13] J. Du, M. Carl, M. Bydder, A. Takahashi, C.B. Chung, and G.M. Bydder. Qualitative and quantitative ultrashort echo time (UTE) imaging of cortical bone. *Journal of Magnetic Resonance*, 207(2):304–311, 12 2010.

[14] P. Dendy and B. Heaton. *Physics of Diagnostic Radiology*. IOP Publishing, Bristol, UK, 3rd edition, 2012.

[15] C.M. De Bazelaire, G.D. Duhamel, N.M. Rofsky, and D.C. Alsop. MR imaging relaxation times of abdominal and pelvic tissues measured in vivo at 3.0 T: Preliminary results. *Radiology*, 230(3):652–659, 3 2004.

[16] N.D. Gai, A.A. Malayeri, and D.A. Bluemke. Three-dimensional T1 and T2* mapping of human lung parenchyma using interleaved saturation recovery with dual echo ultrashort echo time imaging (ITSR-DUTE). *Journal of Magnetic Resonance Imaging*, 45(4):1097–1104, 4 2017.

[17] S.A. Smith, R.A. Edden, J.A. Farrell, P.B. Barker, and P.C. Van Zijl. Measurement of T1 and T2 in the cervical spinal cord at 3 Tesla. *Magnetic Resonance in Medicine*, 60(1):213–219, 2008.

[18] Y. Shao, S.R. Cherry, K. Farahani, K. Meadors, S. Siegel, R.W. Silverman, and P.K. Marsden. Simultaneous PET and MR imaging. *Physics in Medicine & Biology*, 42(10):1965, 10 1997.

[19] P.J. Schleyer, T. Schaeffter, and P.K. Marsden. The effect of inaccurate bone attenuation coefficient and segmentation on reconstructed PET images. *Nuclear Medicine Communications*, 31(8):708–716, 8 2010.

[20] V. Keereman, P. Mollet, Y. Berker, V. Schulz, and S. Vandenberghe. Challenges and current methods for attenuation correction in PET/MR. *Magnetic Resonance Materials in Physics, Biology and Medicine*, 26(1):81–98, 2 2013.

[21] C. Catana. Motion correction options in PET/MRI. *Seminars in Nuclear Medicine*, 45(3):212–223, 5 2015.

[22] A. Mehranian, M.A. Belzunce, C.J. McGinnity, A. Bustin, C. Prieto, A. Hammers, and A.J. Reader. Multi-modal synergistic PET and MR reconstruction using mutually weighted quadratic priors. *Magnetic Resonance in Medicine*, 81(3):2120–2134, 3 2019.

[23] H. Jadvar and P.M. Colletti. Competitive advantage of PET/MRI. *European Journal of Radiology*, 83(1):84–94, 1 2014.

[24] V. Garibotto, S. Heinzer, S. Vulliemoz, R. Guignard, M. Wissmeyer, M. Seeck, K.O. Lovblad, H. Zaidi, O. Ratib, and M.I. Vargas. Clinical applications of hybrid PET/MRI in neuroimaging. *Clinical Nuclear Medicine*, 38(1), 1 2013.

[25] C.J. Scott, J. Jiao, A. Melbourne, N. Burgos, D.M. Cash, E.D. Vita, P.J. Markiewicz, A. O'Connor, D.L. Thomas, P.S. Weston, J.M. Schott, B.F. Hutton, and S. Ourselin. Reduced acquisition time PET pharmacokinetic modelling using simultaneous ASL–MRI: proof of concept. *Journal of Cerebral Blood Flow & Metabolism*, 39(12):2419, 12 2019.

[26] Z. Kiamanesh, F. Banezhad, Z. Nasiri, F. Emami, G. Treglia, and R. Sadeghi. Physiological distribution of 18F-FDG in the spinal cord: A systematic review. *The Journal of Spinal Cord Medicine*, 0(0):1–8, 11 2019.

[27] K. Thielemans, C. Tsoumpas, S. Mustafovic, T. Beisel, P. Aguiar, N. Dikaios, and M.W. Jacobson. STIR: software for tomographic image reconstruction release 2. *Physics in Medicine & Biology*, 57(4):867, 1 2012.

[28] E. Ovtchinnikov, R. Brown, C. Kolbitsch, E. Pasca, C. da Costa-Luis, A.G. Gillman, B.A. Thomas, N. Efthimiou, J. Mayer, P. Wadhwa, M.J. Ehrhardt,

S. Ellis, J.S. Jørgensen, J. Matthews, C. Prieto, A.J. Reader, C. Tsoumpas, M. Turner, D. Atkinson, and K. Thielemans. SIRF: Synergistic Image Reconstruction Framework. *Computer Physics Communications*, 249:107087, 4 2020.

[29] D. Deidda, N.A. Karakatsanis, P.M. Robson, Y.J. Tsai, N. Efthimiou, K. Thielemans, Z.A. Fayad, R.G. Aykroyd, and C. Tsoumpas. Hybrid PET-MR list-mode kernelized expectation maximization reconstruction. *Inverse Problems*, 35(4):044001, 3 2019.

[30] B. Bai, Q. Li, and R.M. Leahy. MR guided PET image reconstruction. *Seminars in nuclear medicine*, 43(1):30, 2013.

[31] E. Lennie, C. Tsoumpas, and S. Sourbron. Multimodal phantoms for clinical PET/MRI. *EJNMMI Physics*, 8(1):1–24, 12 2021.

[32] L. Ng and F. Khan. *Motor Neuron Diseases: Causes, Classification and Treatments*. Nova Science Publishers, New York, USA, 2012.

[33] W. Kapit and L.M. Elson. *The Anatomy Coloring Book*. Pearson, 4th edition, 2014.

[34] A. Frostell, R. Hakim, E.P. Thelin, P. Mattsson, and M. Svensson. A review of the segmental diameter of the healthy human spinal cord. *Frontiers in Neurology*, 7(DEC):238, 12 2016.

[35] H. Blasco, P. Vourch, P.F. Pradat, P.H. Gordon, C.R. Andres, and P. Corcia. Further development of biomarkers in amyotrophic lateral sclerosis. *Expert Review of Molecular Diagnostics*, 16(8):853–868, 8 2016.

[36] P.W. Stroman, C. Wheeler-Kingshott, M. Bacon, J.M. Schwab, R. Bosma, J. Brooks, D. Cadotte, T. Carlstedt, O. Ciccarelli, J. Cohen-Adad, A. Curt, N. Evangelou, M.G. Fehlings, M. Filippi, B.J. Kelley, S. Kollias, A. Mackay, C.A. Porro, S. Smith, S.M. Strittmatter, P. Summers, and I. Tracey. The current state-of-the-art of spinal cord imaging: Methods. *NeuroImage*, 84:1070–1081, 1 2014.

[37] D.W. McRobbie, E.A. Moore, M.J. Graves, and M.R. Prince. *MRI From Picture to Proton*. Cambridge University Press, Cambridge, UK, second edition, 2007.

[38] W.T. Dixon. Simple proton spectroscopic imaging. *Radiology*, 153(1):189–194, 10 1984.

[39] S. Xie, X. Zhang, Y. Zhang, G. Ying, Q. Huang, J. Xu, and Q. Peng. Evaluation of various scintillator materials in radiation detector design for positron emission tomography (PET). *Crystals*, 10(10):1–15, 10 2020.

[40] P. Courault, L. Zimmer, and S. Lancelot. Toward Functional PET Imaging of the Spinal Cord. *Seminars in Nuclear Medicine*, 8 2024.

[41] I. Polycarpou, G. Soultanidis, and C. Tsoumpas. Synergistic motion compensation strategies for positron emission tomography when acquired simultaneously with magnetic resonance imaging. *Philosophical Transactions of the Royal Society A*, 379(2204), 8 2021.

[42] I. Alberts, H. Sari, C. Mingels, A. Afshar-Oromieh, T. Pyka, K. Shi, and A. Rominger. Long-axial field-of-view PET/CT: perspectives and review of a revolutionary development in nuclear medicine based on clinical experience in over 7000 patients. *Cancer Imaging 2023 23:1*, 23(1):1–15, 3 2023.

[43] M. Soret, S.L. Bacharach, and I. Buvat. Partial-Volume Effect in PET Tumor Imaging. *Journal of Nuclear Medicine*, 48(6):932–945, 6 2007.

[44] V. Bettinardi, I. Castiglioni, E. De Bernardi, and M.C. Gilardi. PET quantification: Strategies for partial volume correction. *Clinical and Translational Imaging*, 2(3):199–218, 7 2014.

[45] B.A. Thomas, V. Cuplov, A. Bousse, A. Mendes, K. Thielemans, B.F. Hutton, and K. Erlandsson. PETPVC: a toolbox for performing partial volume correction techniques in positron emission tomography. *Physics in Medicine & Biology*, 61(22):7975, 10 2016.

[46] K. Erlandsson, I. Buvat, P.H. Pretorius, B.A. Thomas, and B.F. Hutton. A review of partial volume correction techniques for emission tomography and their applications in neurology, cardiology and oncology. *Physics in Medicine & Biology*, 57(21):R119, 10 2012.

[47] O.G. Rousset, Y. Ma, and A.C. Evans. Correction for partial volume effects in PET: Principle and validation. *Journal of Nuclear Medicine*, 39(5):904–911, 5 1998.

[48] B.A. Thomas, K. Erlandsson, M. Modat, L. Thurfjell, R. Vandenberghe, S. Ourselin, and B.F. Hutton. The importance of appropriate partial volume correction for PET quantification in Alzheimer's disease. *European Journal of Nuclear Medicine and Molecular Imaging*, 38(6):1104–1119, 6 2011.

[49] A.G. Gillman, M.H. Quah, E. Papoutsellis, K. Thielemans, P. Bourgeat, C. Delplancke, J. Fripp, E. Pasca, and J.A. Dowling. Anatomically-guided deconvolution of PET using directional total variation regularization. *medRxiv*, page 2023.04.23.23289004, 4 2023.

[50] C. Catana, A. Drzezga, W.D. Heiss, and B.R. Rosen. PET/MRI for neurologic applications. *Journal of Nuclear Medicine*, 53(12):1916–1925, 12 2012.

[51] M. Bauckneht, S. Capitanio, S. Raffa, L. Roccatagliata, M. Pardini, C. Lapucci, C. Marini, G. Sambuceti, M. Inglese, P. Gallo, D. Cecchin, F. Nobili, and S. Morbelli. Molecular imaging of multiple sclerosis: from the clinical demand to novel radiotracers. *EJNMMI Radiopharmacy and Chemistry*, 4(1):6, 4 2019.

[52] E. Grecchi, M. Veronese, B. Bodini, D. García-Lorenzo, M. Battaglini, B. Stankoff, and F.E. Turkheimer. Multimodal partial volume correction: Application to [11C]PIB PET/MRI myelin imaging in multiple sclerosis. *Journal of Cerebral Blood Flow and Metabolism*, 37(12):3803–3817, 12 2017.

[53] A. Kolb, H.F. Wehrl, M. Hofmann, M.S. Judenhofer, L. Eriksson, R. Ladebeck, M.P. Lichy, L. Byars, C. Michel, H.P. Schlemmer, M. Schmand, C.D. Claussen, V. Sossi, and B.J. Pichler. Technical performance evaluation of a human brain PET/MRI system. *European Radiology*, 22(8):1776–1788, 8 2012.

[54] A.M. Grant, T.W. Deller, M.M. Khalighi, S.H. Maramraju, G. Delso, and C.S. Levin. NEMA NU 2-2012 performance studies for the SiPM-based ToF-PET component of the GE SIGNA PET/MR system. *Medical Physics*, 43(5):2334–2343, 5 2016.

[55] H. Zaidi, M.L. Montandon, and A. Alavi. Advances in Attenuation Correction Techniques in PET. *PET Clinics*, 2(2):191–217, 4 2007.

[56] A. Mehranian and H. Zaidi. Impact of time-of-flight PET on quantification errors in MR imaging-based attenuation correction. *Journal of Nuclear Medicine*, 56(4):635–641, 4 2015.

[57] V. Keereman, P. Mollet, Y. Fierens, S. Espana, and S. Vandenberghe. Design of a realistic PET-CT-MRI phantom. In *IEEE Nuclear Science Symposium Conference Record*, pages 3173–3177. 10 2011.

[58] A. Samarin, C. Burger, S.D. Wollenweber, D.W. Crook, I.A. Burger, D.T. Schmid, G.K. Von Schulthess, and F.P. Kuhn. PET/MR imaging of bone

lesions - Implications for PET quantification from imperfect attenuation correction. *European Journal of Nuclear Medicine and Molecular Imaging*, 39(7): 1154–1160, 7 2012.

[59] A. Ferguson, J. McConathy, Y. Su, D. Hewing, and R. Laforest. Attenuation effects of MR headphones during brain PET/MR studies. *Journal of Nuclear Medicine Technology*, 42(2):93–100, 6 2014.

[60] S. Vandenberghe and P.K. Marsden. PET-MRI: A review of challenges and solutions in the development of integrated multimodality imaging. *Physics in Medicine and Biology*, 60(4):115–154, 2 2015.

[61] M.E. Lindemann, M. Oehmigen, J.O. Blumhagen, M. Gratz, and H.H. Quick. MR-based truncation and attenuation correction in integrated PET/MR hybrid imaging using HUGE with continuous table motion. *Medical Physics*, 44 (9):4559–4572, 9 2017.

[62] U. Aydingoz, A.E. Yildiz, and F.B. Ergen. Zero echo time musculoskeletal MRI: technique, optimization, applications, and pitfalls. *Radiographics*, 42(5): 1398–1414, 9 2022.

[63] F. Wiesinger and M.L. Ho. Zero-TE MRI: principles and applications in the head and neck. *The British Journal of Radiology*, 95(1136), 8 2022.

[64] B. Sgard, M. Khalifé, A. Bouchut, B. Fernandez, M. Soret, A. Giron, C. Zaslavsky, G. Delso, M.O. Habert, and A. Kas. ZTE MR-based attenuation correction in brain FDG-PET/MR: performance in patients with cognitive impairment. *European Radiology*, 30(3):1770–1779, 3 2020.

[65] S. Tong, A.M. Alessio, and P.E. Kinahan. Image reconstruction for PET/CT scanners: past achievements and future challenges. *Imaging in medicine*, 2(5): 529, 10 2010.

[66] C. Tsoumpas, I. Polycarpou, K. Thielemans, C. Buerger, A.P. King, T. Schaeffter, and P.K. Marsden. The effect of regularization in motion compensated PET image reconstruction: a realistic numerical 4D simulation study. *Physics in Medicine & Biology*, 58(6):1759, 2 2013.

[67] J. Bland, A. Mehranian, M.A. Belzunce, S. Ellis, C. da Costa-Luis, C.J. McGinnity, A. Hammers, and A.J. Reader. Intercomparison of MR-informed PET image reconstruction methods. *Medical Physics*, 46(11):5055–5074, 11 2019.

[68] E.K. Lysvik, L.T.G. Mikalsen, M.E. Rootwelt-Revheim, K.E. Emblem, and T. Hjørnevik. Optimization of Q.Clear reconstruction for dynamic 18F PET imaging. *EJNMMI Physics*, 10(1):1–13, 12 2023.

[69] S. Ross. Q.Clear Specification Report. Technical report, GE Healthcare, 2014.

[70] A.M. Alessio and P.E. Kinahan. Improved quantitation for PET/CT image reconstruction with system modeling and anatomical priors. *Medical Physics*, 33(11):4095–4103, 11 2006.

[71] J.E. Bowsher, V.E. Johnson, T.G. Turkington, R.J. Jaszczak, C.E. Floyd, and R. Edward Coleman. Bayesian reconstruction and use of anatomical a priori information for emission tomography. *IEEE Transactions on Medical Imaging*, 15(5):673–686, 1996.

[72] T. Hofmann, B. Schölkopf, and A.J. Smola. Kernel methods in machine learning. *The Annals of Statistics*, 36(3):1171–1220, 2008.

[73] G. Wang and J. Qi. PET image reconstruction using kernel method. *IEEE Transactions on Medical Imaging*, 34(1):61–71, 1 2015.

[74] W. Hutchcroft, G. Wang, K.T. Chen, C. Catana, and J. Qi. Anatomically-aided PET reconstruction using the kernel method. *Physics in Medicine & Biology*, 61(18), 8 2016.

[75] J. Bland, M.A. Belzunce, S. Ellis, C.J. McGinnity, A. Hammers, and A.J. Reader. Spatially compact MR-guided kernel em for PET image reconstruction. *IEEE Transactions on Radiation and Plasma Medical Sciences*, 2(5):470–482, 9 2018.

[76] J. Bland, A. Mehranian, M.A. Belzunce, S. Ellis, C.J. McGinnity, A. Hammers, and A.J. Reader. MR-guided kernel EM reconstruction for reduced dose PET imaging. *IEEE Transactions on Radiation and Plasma Medical Sciences*, 2(3):235–243, 5 2018.

[77] J. Bolcaen, M. Acou, K. Mertens, G. Hallaert, C. Van den Broecke, E. Achten, and I. Goethals. Structural and metabolic features of two different variants of multiple sclerosis: A PET/MRI study. *Journal of Neuroimaging*, 23(3):431–436, 7 2013.

[78] F. Antonescu, M. Adam, C. Popa, and S. Tuţă. A review of cervical spine MRI in ALS patients. *Journal of medicine and life*, 11(2):123–127, 4 2018.

[79] M. Bauckneht, R. Lai, A. Miceli, D. Schenone, V. Cossu, M.I. Donegani, S. Raffa, A. Borra, S. Marra, C. Campi, A. Orengo, A.M. Massone, A. Tagliafico, C. Caponnetto, C. Cabona, A. Cistaro, A. Chiò, S. Morbelli, F. Nobili, G. Sambuceti, M. Piana, and C. Marini. Spinal cord hypermetabolism extends to skeletal muscle in amyotrophic lateral sclerosis: a computational approach to [18F]-fluorodeoxyglucose PET/CT images. *European Journal of Nuclear Medicine and Molecular Imaging Research*, 10(23), 2020.

[80] C. Marini, A. Cistaro, C. Campi, A. Calvo, C. Caponnetto, F.M. Nobili, P. Fania, M.C. Beltrametti, C. Moglia, G. Novi, A. Buschiazzo, A. Perasso, A. Canosa, C. Scialò, E. Pomposelli, A.M. Massone, M.C. Bagnara, S. Cammarosano, P. Bruzzi, S. Morbelli, G. Sambuceti, G. Mancardi, M. Piana, and A. Chiò. A PET/CT approach to spinal cord metabolism in amyotrophic lateral sclerosis. *European Journal of Nuclear Medicine and Molecular Imaging*, 43(11):2061–2071, 10 2016.

[81] C. Marini, S. Morbelli, A. Cistaro, C. Campi, C. Caponnetto, M. Bauckneht, A. Bellini, A. Buschiazzo, I. Calamia, M.C. Beltrametti, S. Margotti, P. Fania, I. Poggi, C. Cabona, S. Capitanio, R. Piva, A. Calvo, C. Moglia, A. Canosa, A. Massone, F. Nobili, G. Mancardi, A. Chiò, M. Piana, and G. Sambuceti. Interplay between spinal cord and cerebral cortex metabolism in amyotrophic lateral sclerosis. *Brain*, 141(8):2272–2279, 8 2018.

[82] D. Van Weehaeghe, M. Devrome, G. Schramm, J. De Vocht, W. Deckers, K. Baete, P.V. Damme, M. Koole, and K. Van Laere. Combined brain and spinal FDG PET allows differentiation between ALS and ALS mimics. *European Journal of Nuclear Medicine and Molecular Imaging*, 47:2681–2690, 2020.

[83] T. Yamashita, T. Hatakeyama, K. Sato, Y. Fukui, N. Hishikawa, Y. Ohta, Y. Nishiyama, N. Kawai, T. Tamiya, and K. Abe. Flow-metabolism uncoupling in the cervical spinal cord of ALS patients. *Neurological Sciences*, 38(4): 659–665, 4 2017.

[84] T. Yamashita, T. Hatakeyama, K. Sato, Y. Fukui, N. Hishikawa, M. Takemoto, Y. Ohta, Y. Nishiyama, N. Kawai, T. Tamiya, and K. Abe. Hypoxic stress visualized in the cervical spinal cord of ALS patients. *Neurological Research*, 00:1–5, 12 2020.

[85] J.H. Kindred, P.J. Koo, and T. Rudroff. Glucose uptake of the spinal cord in patients with multiple sclerosis detected by 18f-fluorodeoxyglucose PET/CT after walking. *Spinal Cord*, 52(3):S11–S13, 11 2014.

[86] C.W. van der Weijden, J.F. Meilof, A. van der Hoorn, J. Zhu, C. Wu, Y. Wang, A.T. Willemsen, R.A. Dierckx, A.A. Lammertsma, and E.F. de Vries. Quantitative assessment of myelin density using [11C]MeDAS PET in patients with multiple sclerosis: a first-in-human study. *European Journal of Nuclear Medicine and Molecular Imaging*, 49(10):3492–3507, 8 2022.

[87] V. Brancato, P. Borrelli, V. Alfano, M. Picardi, M. Mascalchi, E. Nicolai, M. Salvatore, and M. Aiello. The impact of MR-based attenuation correction in spinal cord FDG-PET/MR imaging for neurological studies. *Medical Physics*, 2021.

[88] C.Y. Sander, H.D. Hansen, and H.Y. Wey. Advances in simultaneous PET/MR for imaging neuroreceptor function. *Journal of Cerebral Blood Flow & Metabolism*, 40(6):1148–1166, 6 2020.

[89] A. Hahn, G. Gryglewski, L. Nics, L. Rischka, S. Ganger, H. Sigurdardottir, C. Vraka, L. Silberbauer, T. Vanicek, A. Kautzky, W. Wadsak, M. Mitterhauser, M. Hartenbach, M. Hacker, S. Kasper, and R. Lanzenberger. Task-relevant brain networks identified with simultaneous PET/MR imaging of metabolism and connectivity. *Brain Structure & Function*, 223(3), 4 2018.

[90] J.F. Schäfer, S. Gatidis, H. Schmidt, B. Gückel, I. Bezrukov, C.A. Pfannenberg, M. Reimold, M. Ebinger, J. Fuchs, C.D. Claussen, and N.F. Schwenzer. Simultaneous whole-body PET/MR imaging in comparison to PET/CT in pediatric oncology: Initial results. *Radiology*, 273(1):220–231, 10 2014.

[91] S. Mostafapour, M. Greuter, J.H. van Snick, A.H. Brouwers, R.A. Dierckx, J. van Sluis, A.A. Lammertsma, and C. Tsoumpas. Ultra-low dose CT scanning for PET/CT. *Medical Physics*, 51(1):139–155, 1 2024.

[92] L. Marner, O.M. Henriksen, M. Lundemann, V.A. Larsen, and I. Law. Clinical PET/MRI in neurooncology: opportunities and challenges from a single-institution perspective. *Clinical and Translational Imaging*, 5(2):135–149, 4 2017.

[93] A. Batouli, J. Braun, K. Singh, A. Gholamrezanezhad, B.U. Casagranda, and A. Alavi. Diagnosis of non-osseous spinal metastatic disease: the role of PET/CT and PET/MRI. *Journal of Neuro-Oncology*, 138(2):221–230, 6 2018.

[94] M. Aiello, C. Cavaliere, D. Fiorenza, A. Duggento, L. Passamonti, and N. Toschi. Neuroinflammation in neurodegenerative diseases: current multimodal imaging studies and future opportunities for hybrid PET/MRI. *Neuroscience*, 403:125–135, 4 2019.

[95] D.V. Weehaeghe, E.V. Schoor, J.D. Vocht, M. Koole, B. Attili, S. Celen, L. Declercq, D.R. Thal, P.V. Damme, G. Bormans, and K.V. Laere. TSPO versus P2X7 as target for neuroinflammation – an in vitro and in vivo study. *Journal of Nuclear Medicine*, 61(4):604–607, 9 2019.

[96] E.M. Ratai, M.J. Alshikho, N.R. Zürcher, M.L. Loggia, C.L. Cebulla, P. Cernasov, B. Reynolds, J. Fish, R. Seth, S. Babu, S. Paganoni, J.M. Hooker, and N. Atassi. Integrated imaging of [11C]-PBR28 PET, MR diffusion and magnetic resonance spectroscopy 1H-MRS in amyotrophic lateral sclerosis. *NeuroImage: Clinical*, 20:357–364, 1 2018.

[97] M.M. Makary, A. Weerasekara, H. Rodham, B.G. Hightower, C.E.J. Tseng, J. Chan, S. Chew, S. Paganoni, E.M. Ratai, N.R. Zürcher, J.M. Hooker, N. Atassi, and S. Babu. Comparison of two clinical upper motor neuron burden rating scales in ALS using quantitative brain imaging. *ACS Chemical Neuroscience*, 12(5):906–916, 3 2021.

[98] M.S. Pitombeira, M. Koole, K.R. Campanholo, A.M. Souza, F.L. Duran, D.J. Solla, M.F. Mendes, S.L. Pereira, C.M. Rimkus, G.F. Busatto, D. Callegaro, C.A. Buchpiguel, and D. de Paula Faria. Innate immune cells and myelin profile in multiple sclerosis: a multi-tracer PET/MR study. *European Journal of Nuclear Medicine and Molecular Imaging*, 49(13):4551–4566, 11 2022.

[99] D. Albrecht, S. Ahmed, N. Kettner, R. Borra, J. Cohen-Adad, H. Deng, T. Houle, A. Opalacz, S. Roth, M.V. Melo, L. Chen, J. Mao, J. Hooker, M.L. Loggia, and Y. Zhang. Neuroinflammation of the spinal cord and nerve roots in chronic radicular pain patients. *Pain*, 159(5):968–977, 5 2018.

[100] GE Healthcare. SIGNA PET/MR Technical Data. Technical report, 2014.

[101] N.J. Patel, V. Gupta, P.G. Vibhute, M.K. Jain, and J.M. Accurso. A large cohort study of 18F Fluoro-Deoxy-Glucose uptake in normal spinal cord: Quantitative assessment of the contamination from adjacent vertebral marrow uptake and validity of normalizing the cord uptake. *Journal of Computer Assisted Tomography*, 41(1):125–130, 1 2017.

[102] A. Kolb, A.W. Sauter, L. Eriksson, A. Vandenbrouke, C.C. Liu, C. Levin, B.J. Pichler, and M. Rafecas. Shine-through in PET/MR imaging: Effects of the magnetic field on positron range and subsequent image artifacts. *Journal of Nuclear Medicine*, 56(6):951–954, 6 2015.

[103] J. Silva-Rodríguez, J. Cortés, X. Rodríguez-Osorio, J. López-Urdaneta, J. Pardo-Montero, P. Aguiar, and C. Tsoumpas. Iterative structural and functional synergistic resolution recovery (iSFS-RR) applied to PET-MR images in epilepsy. *IEEE Transactions on Nuclear Science*, 63(5):2434–2442, 10 2016.

[104] M.T. Madsen and J.J. Sunderland. Nuclear Medicine and PET Phantoms. In L.A. DeWerd and M. Kissick, editors, *The Phantoms of Medical and Health Physics*, chapter 11, pages 201–222. Springer, New York, NY, 1st edition, 2014.

[105] M.E. Daube-Witherspoon, J.S. Karp, M.E. Casey, F.P. DiFilippo, H. Hines, G. Muehllehner, V. Simcic, C.W. Stearns, L.E. Adam, S. Kohlmyer, and V. Sossi. PET performance measurements using the NEMA NU 2-2001 Standard. *Journal of Nuclear Medicine*, 43(10), 2002.

[106] Y. Jiang, D. Ma, K.E. Keenan, K.F. Stupic, V. Gulani, and M.A. Griswold. Repeatability of magnetic resonance fingerprinting T1 and T2 estimates assessed using the ISMRM/NIST MRI system phantom. *Magnetic Resonance in Medicine*, 78(4):1452–1457, 10 2017.

[107] American College of Radiology. Large and Medium Phantom Test Guiudance for the ACR MRI Accreditation Program. Technical report, 2022.

[108] C.C. Chen, Y.L. Wan, Y.Y. Wai, and H.L. Liu. Quality Assurance of Clinical MRI Scanners Using ACR MRI Phantom: Preliminary Results. *Journal of Digital Imaging*, 17(4):279, 12 2004.

[109] K. Hattori, Y. Ikemoto, W. Takao, S. Ohno, T. Harimoto, S. Kanazawa, M. Oita, K. Shibuya, M. Kuroda, and H. Kato. Development of MRI phantom equivalent to human tissues for 3.0-T MRI. *Medical Physics*, 40(3):032303, 2 2013.

[110] A. Valladares, S. Ahangari, T. Beyer, R. Boellaard, Z. Chalampalakis, C. Comtat, L. DalToso, A.E. Hansen, M. Koole, J. Mackewn, P. Marsden, J. Nuyts, F. Padormo, R. Peeters, S. Poth, E. Solari, and I. Rausch. Clinically valuable quality control for PET/MRI systems: Consensus recommendation from the HYBRID consortium. *Frontiers in Physics*, 7:136, 9 2019.

[111] R.R. Price, L. Axel, T. Morgan, R. Newman, W. Perman, N. Schneiders, M. Selikson, M. Wood, and S.R. Thomas. Quality assurance methods and phantoms for magnetic resonance imaging: Report of AAPM nuclear magnetic resonance Task Group No. 1a. *Medical Physics*, 17(2):287–295, 1990.

[112] C.K. McGarry, L.J. Grattan, A.M. Ivory, F. Leek, G.P. Liney, Y. Liu, P. Miloro, R. Rai, A.P. Robinson, A.J. Shih, B. Zeqiri, and C.H. Clark. Tissue mimicking materials for imaging and therapy phantoms: A review. *Physics in Medicine and Biology*, 65(23):23–24, 11 2020.

[113] Y. Baba, M.M. Lerch, D.D. Stark, A. Tanimoto, B.P. Kreft, L. Zhao, A.K. Saluja, and M. Takahashi. Time after excision and temperature alter ex vivo tissue relaxation time measurements. *Journal of Magnetic Resonance Imaging*, 4(5):647–651, 9 1994.

[114] C. Huang, J. Ouyang, T.G. Reese, Y. Wu, G. El Fakhri, and J.L. Ackerman. Continuous MR bone density measurement using water- and fat-suppressed projection imaging (WASPI) for PET attenuation correction in PET-MR. *Physics in Medicine and Biology*, 60(20):N369–N381, 9 2015.

[115] P.K. Han, D.E. Horng, K. Gong, Y. Petibon, K. Kim, Q. Li, K.A. Johnson, G. El Fakhri, J. Ouyang, and C. Ma. MR-based PET attenuation correction using a combined ultrashort echo time/multi-echo Dixon acquisition. *Medical Physics*, 47(7):3064–3077, 7 2020.

[116] J. Lillington, L. Brusaferri, K. Kläser, K. Shmueli, R. Neji, B.F. Hutton, F. Fraioli, S. Arridge, M.J. Cardoso, S. Ourselin, K. Thielemans, and D. Atkinson. PET/MRI attenuation estimation in the lung: A review of past, present, and potential techniques. *Medical Physics*, 47(2):790–811, 2 2020.

[117] E.J. Hoffman, P.D. Cutler, W.M. Digby, and J.C. Mazziotta. 3-D phantom to simulate cerebral blood flow and metabolic images for PET. *IEEE Transactions on Nuclear Science*, 37(2):616–620, 1990.

[118] H. Iida, Y. Hori, K. Ishida, E. Imabayashi, H. Matsuda, M. Takahashi, H. Maruno, A. Yamamoto, K. Koshino, J. Enmi, S. Iguchi, T. Moriguchi, H. Kawashima, and T. Zeniya. Three-dimensional brain phantom containing bone and grey matter structures with a realistic head contour. *Annals of Nuclear Medicine*, 27(1):25–36, 1 2013.

[119] H. Okazawa, Y. Higashino, T. Tsujikawa, H. Arishima, T. Mori, Y. Kiyono, H. Kimura, and K.i. Kikuta. Noninvasive method for measurement of cerebral blood flow using O-15 water PET/MRI with ASL correlation. *European Journal of Radiology*, 105:102–109, 8 2018.

[120] J. Harries, T.H. Jochimsen, T. Scholz, T. Schlender, H. Barthel, O. Sabri, and B. Sattler. A realistic phantom of the human head for PET-MRI. *EJNMMI Physics*, 7(1):52, 8 2020.

[121] C. Gillmann, N. Homolka, W. Johnen, A. Runz, G. Echner, A. Pfaffenberger, P. Mann, V. Schneider, A.L. Hoffmann, E.G.C. Troost, S.A. Koerber, J. Kotzerke, and B. Beuthien-Baumann. Technical Note: ADAM PETer – An anthropomorphic, deformable and multimodality pelvis phantom with positron emission tomography extension for radiotherapy. *Medical Physics*, page mp.14597, 12 2020.

[122] F. Gallivanone, I. Carne, M. Interlenghi, D. D'Ambrosio, M. Baldi, D. Fantinato, and I. Castiglioni. A method for manufacturing oncological phantoms for the quantification of 18F-FDG PET and DW-MRI studies. *Contrast Media and Molecular Imaging*, 2017.

[123] S.Y. Chun, T.G. Reese, J. Ouyang, B. Guerin, C. Catana, X. Zhu, N.M. Alpert, and G. El Fakhri. MRI-based nonrigid motion correction in simultaneous PET/MRI. *Journal of Nuclear Medicine*, 53(8):1284–1291, 8 2012.

[124] B. Guérin, S. Cho, S.Y. Chun, X. Zhu, N.M. Alpert, G. El Fakhri, T. Reese, and C. Catana. Nonrigid PET motion compensation in the lower abdomen using simultaneous tagged-MRI and PET imaging. *Medical Physics*, 38(6Part1): 3025–3038, 5 2011.

[125] G. McIlvain, E. Ganji, C. Cooper, M.L. Killian, B.A. Ogunnaike, and C.L. Johnson. Reliable preparation of agarose phantoms for use in quantitative magnetic resonance elastography. *Journal of the Mechanical Behavior of Biomedical Materials*, 97:65–73, 9 2019.

[126] A. Valladares, T. Beyer, and I. Rausch. Physical imaging phantoms for simulation of tumor heterogeneity in PET, CT, and MRI: An overview of existing designs. *Medical Physics*, 47(4):2023–2037, 4 2020.

[127] D. Chandramohan, P. Cao, M. Han, H. An, J.J. Sunderland, P.E. Kinahan, R. Laforest, T.A. Hope, and P.E. Larson. Bone material analogues for PET/MRI phantoms. *Medical Physics*, 47(5):2161–2170, 2020.

[128] J. Teuho, J. Johansson, J. Linden, A.E. Hansen, S. Holm, S.H. Keller, G. Delso, P. Veit-Haibach, K. Magota, V. Saunavaara, T. Tolvanen, M. Ters, and H. Iida. Effect of attenuation correction on regional quantification between PET/MR and PET/CT: A multicenter study using a 3-dimensional brain phantom. *Journal of Nuclear Medicine*, 57(5):818–824, 5 2016.

[129] L. Talalwa, A. Gordji-Nejad, G. Natour, A. Drzezga, A. Bauer, and S. Beer. Evaluation of 3D printable rubber-elastomeric polymer as phantom material

for Hybrid PET/MRI. In *2019 IEEE Nuclear Science Symposium and Medical Imaging Conference, NSS/MIC 2019*. 10 2019.

[130] V. Filippou and C. Tsoumpas. Recent advances on the development of phantoms using 3D printing for imaging with CT, MRI, PET, SPECT, and ultrasound. *Medical Physics*, 45(9):e740–e760, 2018.

[131] I. Rausch, A. Valladares, L.K.S. Sundar, T. Beyer, M. Hacker, M. Meyerspeer, and E. Unger. Standard MRI-based attenuation correction for PET/MRI phantoms: a novel concept using MRI-visible polymer. *EJNMMI Physics*, 8 (1), 12 2021.

[132] D. Mitsouras, T.C. Lee, P. Liacouras, C.N. Ionita, T. Pietilla, S.E. Maier, and R.V. Mulkern. Three-dimensional printing of MRI-visible phantoms and MR image-guided therapy simulation. *Magnetic Resonance in Medicine*, 77(2):613–622, 2 2017.

[133] B.E. Yunker, A. Holmgren, K.F. Stupic, J.L. Wagner, S. Huddle, R. Shandas, R.F. Weir, K.E. Keenan, E. Garboczi, and S.E. Russek. Characterization of 3-Dimensional Printing and Casting Materials for use in Computed Tomography and X-ray Imaging Phantoms. *Journal of Research of the National Institute of Standards and Technology*, 125, 9 2020.

[134] B.E. Yunker, K.F. Stupic, J.L. Wagner, S. Huddle, R. Shandas, R.F. Weir, S.E. Russek, and K.E. Keenan. Characterization of 3-dimensional printing and casting materials for use in magnetic resonance imaging phantoms at 3T. *Journal of Research of the National Institute of Standards and Technology*, 125, 2020.

[135] D.H. Paulus, H. Braun, B. Aklan, and H.H. Quick. Simultaneous PET/MR imaging: MR-based attenuation correction of local radiofrequency surface coils. *Medical Physics*, 39(7):4306–4315, 7 2012.

[136] T. Heußer, C.M. Rank, Y. Berker, M.T. Freitag, and M. Kachelrieß. MLAA-based attenuation correction of flexible hardware components in hybrid PET/MR imaging. *EJNMMI Physics*, 4(1):1–23, 12 2017.

[137] I. Dregely, T. Lanz, S. Metz, M.F. Mueller, M. Kuschan, M. Nimbalkar, R.A. Bundschuh, S.I. Ziegler, A. Haase, S.G. Nekolla, and M. Schwaiger. A 16-channel MR coil for simultaneous PET/MR imaging in breast cancer. *European Radiology*, 25(4):1154–1161, 3 2015.

[138] H. Zaidi, N. Ojha, M. Morich, J. Griesmer, Z. Hu, P. Maniawski, O. Ratib, D. Izquierdo-Garcia, Z.A. Fayad, and L. Shao. Design and performance evaluation of a whole-body Ingenuity TF PET-MRI system. *Physics in Medicine and Biology*, 56(10):3091–3106, 5 2011.

[139] G. Krokos, J. MacKewn, L. Pike, W. Hallett, P. Markiewicz, A. Barnes, M. Rega, T.D. Fryer, R. Manavaki, J.M. Anton-Rodriguez, E. Howell, C. Wimberley, T. Clark, G. MacNaught, P. Marsden, and J.C. Matthews. Qualification of the seven Dementias Platform UK PET-MR scanners for multicentre trials. In *2019 IEEE Nuclear Science Symposium and Medical Imaging Conference, NSS/MIC 2019*. 10 2019.

[140] P.R. Caribé, M. Koole, Y. D'Asseler, T.W. Deller, K. Van Laere, and S. Vandenberghe. NEMA NU 2–2007 performance characteristics of GE Signa integrated PET/MR for different PET isotopes. *EJNMMI Physics*, 6(1):1–13, 12 2019.

[141] D.E. Oprea-Lager, M. Yaqub, I.C. Pieters, R. Reinhard, R.J. van Moorselaar, A.J. van den Eertwegh, O.S. Hoekstra, A.A. Lammertsma, and R. Boellaard. A clinical and experimental comparison of time of flight PET/MRI and PET/CT systems. *Molecular Imaging and Biology*, 17(5):714–725, 10 2015.

[142] M. Demır, M. Abuqbeıtah, N. Yeyın, and K. Sonmezoglu. Comparison between PET/MR and PET/CT: NEMA tests and image quality. *Turk Onkoloji Dergisi*, 32(3):95–99, 2017.

[143] S. Wampl, I. Rausch, T. Traub-Weidinger, T. Beyer, M. Gröschl, and J. Cal-González. Quantification accuracy of neuro-oncology PET data as a function of emission scan duration in PET/MR compared to PET/CT. *European Journal of Radiology*, 95:257–264, 10 2017.

[144] G. Oh, E. O'Mahoney, S. Jeavons, P. Law, S. Ngai, G. McGill, C. Yu, and K.A. Miles. Discrepancies between positron emission tomography/magnetic resonance imaging and positron emission tomography/computed tomography in a cohort of oncological patients. *Journal of Medical Imaging and Radiation Oncology*, 64(2):204–210, 4 2020.

[145] S. Ziegler, B.W. Jakoby, H. Braun, D.H. Paulus, and H.H. Quick. NEMA image quality phantom measurements and attenuation correction in integrated PET/MR hybrid imaging. *EJNMMI Physics*, 2(1):1–14, 12 2015.

[146] R. Boellaard, I. Rausch, T. Beyer, G. Delso, M. Yaqub, H.H. Quick, and B. Sattler. Quality control for quantitative multicenter whole-body PET/MR studies: A NEMA image quality phantom study with three current PET/MR systems. *Medical Physics*, 42(10):5961–5969, 9 2015.

[147] S. Ziegler, H. Braun, P. Ritt, C. Hocke, T. Kuwert, and H.H. Quick. Systematic evaluation of phantom fluids for simultaneous PET/MR hybrid imaging. *Journal of Nuclear Medicine*, 54(8):1464–1471, 8 2013.

[148] H. Braun, S. Ziegler, D.H. Paulus, and H.H. Quick. Hybrid PET/MRI imaging with continuous table motion. *Medical Physics*, 39(5):2735–2745, 4 2012.

[149] H. Braun, S. Ziegler, M.G. Lentschig, and H.H. Quick. Implementation and performance evaluation of simultaneous PET/MR whole-body imaging with continuous table motion. *Journal of Nuclear Medicine*, 55(1):161–168, 1 2014.

[150] C. Würslin, H. Schmidt, P. Martirosian, C. Brendle, A. Boss, N.F. Schwenzer, and L. Stegger. Respiratory motion correction in oncologic PET using T1-weighted MR imaging on a simultaneous whole-body PET/MR system. *Journal of Nuclear Medicine*, 54(3):464–471, 3 2013.

[151] T. Inomata, S. Watanuki, H. Odagiri, T. Nambu, N.A. Karakatsanis, H. Ito, H. Watabe, M. Tashiro, and M. Shidahara. A systematic performance evaluation of head motion correction techniques for 3 commercial PET scanners using a reproducible experimental acquisition protocol. *Annals of Nuclear Medicine*, 33(7):459–470, 7 2019.

[152] G.M. Soultanidis, J.E. MacKewn, C. Tsoumpas, and P.K. Marsden. PVA cryogel for construction of deformable PET-MR visible phantoms. *IEEE Transactions on Nuclear Science*, 60(1):95–102, 2013.

[153] A.M. Grant, B.J. Lee, C.M. Chang, and C.S. Levin. Simultaneous PET/MRI images acquired with an RF-transmissive PET insert. In *2014 IEEE Nuclear Science Symposium and Medical Imaging Conference, NSS/MIC 2014*. 2014.

[154] M.F. Bieniosek, B.J. Lee, and C.S. Levin. Technical Note: Characterization of custom 3D printed multimodality imaging phantoms. *Medical Physics*, 42 (10):5913–5918, 9 2015.

[155] A.M. Grant, B.J. Lee, C.M. Chang, and C.S. Levin. Simultaneous PET/MR images acquired with an RF-penetrable PET insert. In *2015 IEEE Nuclear Science Symposium and Medical Imaging Conference, NSS/MIC 2015*. 2015.

[156] A.M. Grant, B.J. Lee, C.M. Chang, and C.S. Levin. Simultaneous PET/MR imaging with a radio frequency-penetrable PET insert. *Medical Physics*, 44 (1):112–120, 1 2017.

[157] A. Renner, I. Rausch, J. Cal Gonzalez, R. Frass-Kriegl, L.N. De Lara, J. Sieg, E. Laistler, M. Glanzer, D. Dungl, E. Moser, T. Beyer, M. Figl, and W. Birkfellner. A head coil system with an integrated orbiting transmission point source mechanism for attenuation correction in PET/MRI. *Physics in Medicine and Biology*, 63(22), 11 2018.

[158] S.H. Lim, T.Y. Jung, S. Jung, I.Y. Kim, K.S. Moon, S.Y. Kwon, and W.Y. Jang. Quantitative feasibility evaluation of 11C-Methionine positron emission tomography images in gamma knife radiosurgery : Phantom-based study and clinical application. *Journal of Korean Neurosurgical Society*, 62(4):476–486, 7 2019.

[159] J. Teuho, A. Torrado-Carvajal, H. Herzog, U. Anazodo, R. Klén, H. Iida, and M. Teräs. Magnetic Resonance-Based Attenuation Correction and Scatter Correction in Neurological Positron Emission Tomography/Magnetic Resonance Imaging—Current Status With Emerging Applications. *Frontiers in Physics*, 7, 2020.

[160] K.E. Keenan, M. Ainslie, A.J. Barker, M.A. Boss, K.M. Cecil, C. Charles, T.L. Chenevert, L. Clarke, J.L. Evelhoch, P. Finn, D. Gembris, J.L. Gunter, D.L. Hill, C.R. Jack, E.F. Jackson, G. Liu, S.E. Russek, S.D. Sharma, M. Steckner, K.F. Stupic, J.D. Trzasko, C. Yuan, and J. Zheng. Quantitative magnetic resonance imaging phantoms: A review and the need for a system phantom. *Magnetic Resonance in Medicine*, 79(1):48–61, 1 2018.

[161] J.H. Jung, Y. Choi, J. Jung, S. Kim, H.K. Lim, K.C. Im, C.H. Oh, K.M. Kim, J.G. Kim, and H.W. Park. Development of PET/MRI with insertable PET for simultaneous imaging of human brain. In *IEEE Nuclear Science Symposium Conference Record*. 2013.

[162] J.H. Jung, Y. Choi, J. Jung, S. Kim, H.K. Lim, K.C. Im, C.H. Oh, H.w. Park, K.M. Kim, and J.G. Kim. Development of PET/MRI with insertable PET for simultaneous PET and MR imaging of human brain. *Medical Physics*, 42(5): 2354–2363, 4 2015.

[163] C. Bauer, A. Stolin, J. Proffitt, P. Martone, J. Brefczynski-Lewis, J. Lewis, J. Hankiewicz, R. Raylman, and S. Majewski. Development of a ring PET insert for MRI. In *IEEE Nuclear Science Symposium Conference Record*. 2013.

[164] C. Catana, T. Benner, A. Van Der Kouwe, L. Byars, M. Hamm, D.B. Chonde, C.J. Michel, G. El Fakhri, M. Schmand, and A.G. Sorensen. MRI-assisted PET motion correction for neurologic studies in an integrated MR-PET scanner. *Journal of Nuclear Medicine*, 52(1):154–161, 1 2011.

[165] Z. Huang, Y. Qi, S. Du, G. Chen, and W. Yan. BMI levels with MS Bone mineral density levels in adults with multiple sclerosis: a meta-analysis. *International Journal of Neuroscience*, 125(12):904–912, 12 2015.

[166] E.L. Leemans, F. Kotasidis, M. Wissmeyer, V. Garibotto, and H. Zaidi. Qualitative and quantitative evaluation of blob-based time-of-flight PET image reconstruction in hybrid brain PET/MR imaging. *Molecular Imaging and Biology*, 17(5):704–713, 10 2015.

[167] J. Teuho, J. Johansson, J. Linden, V. Saunavaara, T. Tolvanen, and M. Teräs. Quantitative bias in PET/MR from attenuation correction and reconstruction: A comparison with PET and PET/CT with an anatomical brain phantom and Hoffman brain phantom. In *IEEE Nuclear Science Symposium Conference Record*. 2013.

[168] J.M. Lau, R. Laforest, H. Sotoudeh, X. Nie, S. Sharma, J. McConathy, E. Novak, A. Priatna, R.J. Gropler, and P.K. Woodard. Evaluation of attenuation correction in cardiac PET using PET/MR. *Journal of Nuclear Cardiology*, 24 (3):839–846, 6 2017.

[169] H.R. Marshall, R.Z. Stodilka, J. Theberge, E. Sabondjian, A. Legros, L. Deans, J.M. Sykes, R.T. Thompson, and F.S. Prato. A comparison of MR-based attenuation correction in PET versus SPECT. *Physics in Medicine and Biology*, 56(14):4613–4629, 7 2011.

[170] S. Marchesseau, J.J. Totman, H. Fadil, F.A.A. Leek, J. Chaal, M. Richards, M. Chan, and A. Reilhac. Cardiac motion and spillover correction for quantitative PET imaging using dynamic MRI. *Medical Physics*, 46(2):726–737, 2 2019.

[171] I. Bezrukov, F. Mantlik, H. Schmidt, B. Schölkopf, and B.J. Pichler. MR-based PET attenuation correction for PET/MR imaging. *Seminars in Nuclear Medicine*, 43(1):45–59, 1 2013.

[172] R. Wang, G. Shen, L. Pan, and R. Tian. 68Ga-PSMA PET/MRI for the diagnoses of primary and biochemical recurrent prostate cancer: A aystem review and meta-analysis. *Journal of Nuclear Medicine*, 61(supplement 1), 2020.

[173] J. Johansson, J. Teuho, J. Lindén, U. Tuna, T. Tolvanen, V. Saunavaara, and M. Teräs. Image quantification in high-resolution PET assessed with a new anthropomorphic brain phantom. *IEEE Nuclear Science Symposium Conference Record*, 2013.

[174] J. Teuho, J. Johansson, J. Linden, V. Saunavaara, T. Tolvanen, and M. Teräs. Specification and estimation of sources of bias affecting neurological studies in PET/MR with an anatomical brain phantom. *Nuclear Instruments and Methods in Physics Research, Section A: Accelerators, Spectrometers, Detectors and Associated Equipment*, 734(PART B):179–184, 1 2014.

[175] N.I. Niebuhr, W. Johnen, G. Echner, A. Runz, M. Bach, M. Stoll, K. Giske, S. Greilich, and A. Pfaffenberger. The ADAM-pelvis phantom - An anthropomorphic, deformable and multimodal phantom for MRgRT. *Physics in Medicine and Biology*, 64(4), 2 2019.

[176] T. Heußer, P. Mann, C.M. Rank, M. Schä Fer, A. Dimitrakopoulou-Strauss, H.P. Schlemmer, B.A. Hadaschik, K. Kopka, P. Bachert, M. Kachelrieß, and M.T. Freitag. Investigation of the halo-artifact in 68 Ga-PSMA-11-PET/MRI. *PLoS ONE*, 12(8), 2017.

[177] P. Mann. A hybrid imaging phantom for research applications and quality control for PET/MR and PET/CT systems. *ESMRMB 2015, 32nd annual scientific meeting.*, 28(S1):137–276, 10 2015.

[178] M. Fieseler, T. Kösters, F. Gigengack, H. Braun, H.H. Quick, K.P. Schäfers, and X. Jiang. Motion correction in PET-MRI: A human torso phantom study, 2011.

[179] M. Fieseler, F. Gigengack, X. Jiang, and K.P. Schäfers. Motion correction of whole-body PET data with a joint PET-MRI registration functional. *BioMedical Engineering Online*, 13(1):1–9, 2 2014.

[180] F. Büther, I. Ernst, L.J. Frohwein, J. Pouw, K.P. Schäfers, and L. Stegger. Data-driven gating in PET: Influence of respiratory signal noise on motion resolution. *Medical Physics*, 45(7):3205–3213, 7 2018.

[181] T. Vahle, M. Bacher, D. Rigie, M. Fenchel, P. Speier, J. Bollenbeck, K.P. Schäfers, B. Kiefer, and F.E. Boada. Respiratory motion detection and correction for MR using the pilot tone: Applications for MR and simultaneous PET/MR examinations. *Investigative Radiology*, 55(3):153–159, 3 2020.

[182] J. O'Doherty, E. Sammut, P. Schleyer, J. Stirling, M.S. Nazir, P.K. Marsden, and A. Chiribiri. Feasibility of simultaneous PET-MR perfusion using a novel cardiac perfusion phantom. *European Journal of Hybrid Imaging*, 1(1):4, 12 2017.

[183] A. Chiribiri, A. Schuster, M. Ishida, G. Hautvast, N. Zarinabad, G. Morton, J. Otton, S. Plein, M. Breeuwer, P. Batchelor, T. Schaeffter, and E. Nagel. Perfusion phantom: An efficient and reproducible method to simulate myocardial first-pass perfusion measurements with cardiovascular magnetic resonance. *Magnetic Resonance in Medicine*, 69(3):698–707, 3 2013.

[184] K. Matusiak. Precise image fusion standardization for separated modalities using dedicated multimodal heart phantom. *The Imaging Science Journal*, 67 (1):8–14, 1 2019.

[185] B. Aklan, D.H. Paulus, E. Wenkel, H. Braun, B.K. Navalpakkam, S. Ziegler, C. Geppert, E.E. Sigmund, A. Melsaether, and H.H. Quick. Toward simultaneous PET/MR breast imaging: Systematic evaluation and integration of a radiofrequency breast coil. *Medical Physics*, 40(2):024301, 2 2013.

[186] J.I. Gear, C. Long, D. Rushforth, S.J. Chittenden, C. Cummings, and G.D. Flux. Development of patient-specific molecular imaging phantoms using a 3D printer. *Medical Physics*, 41(8Part1):082502, 7 2014.

[187] E. Johnstone. *Automated MRI-Based Radiotherapy Planning for Brain Tumours*. PhD thesis, University of Leeds, 2019.

[188] M. Alzahrani, C. O'Hara, D. Bird, J.P. Baldwin, M. Naisbit, I. Teh, D.A. Broadbent, B. Al-Qaisieh, E. Johnstone, and R. Speight. Optimisation of cone beam CT radiotherapy imaging protocols using a novel 3D printed head and neck anthropomorphic phantom. *Physics in Medicine & Biology*, 69 (21):215031, 10 2024.

[189] P. Wadhwa, K. Thielemans, N. Efthimiou, K. Wangerin, N. Keat, E. Emond, T. Deller, O. Bertolli, D. Deidda, G. Delso, M. Tohme, F. Jansen, R.N. Gunn, W. Hallett, and C. Tsoumpas. PET image reconstruction using physical and mathematical modelling for time of flight PET-MR scanners in the STIR library. *Methods*, 185:110–119, 1 2021.

[190] NEMA standards publication NU 2-2018 – performance measurements of positron emission tomographs (PET). Technical report, National Electrical Manufacturers Association, Rosslyn, VA., 2018.

[191] J.C. Blechinger, E.L. Madsen, and G.R. Frank. Tissue-mimicking gelatin-agar gels for use in magnetic resonance imaging phantoms. *Medical physics*, 15 (4):629–636, 1988.

[192] W.P. Segars, G. Sturgeon, S. Mendonca, J. Grimes, and B.M. Tsui. 4D XCAT phantom for multimodality imaging research. *Medical Physics*, 37(9):4902–4915, 9 2010.

[193] B.H. Do, C. Mari, J.R. Tseng, A. Quon, J. Rosenberg, and S. Biswal. Pattern of 18F-FDG uptake in the spinal cord in patients with non-central nervous system malignancy. *Spine*, 36(21), 10 2011.

[194] C. Catana, A. Van Der Kouwe, T. Benner, C.J. Michel, M. Hamm, M. Fenchel, B. Fischl, B. Rosen, M. Schmand, and A.G. Sorensen. Toward implementing an MRI-based PET attenuation-correction method for neurologic studies on the MR-PET brain prototype. *Journal of Nuclear Medicine*, 51(9):1431–1438, 9 2010.

[195] N.H. Prakken, F.L. Besson, R.J. Borra, F. Büther, R.R. Buechel, C. Catana, A. Chiti, R.A. Dierckx, M.R. Dweck, P.A. Erba, A.W. Glaudemans, L.C. Gormsen, I. Hristova, M. Koole, T.C. Kwee, F.M. Mottaghy, I. Polycarpou, M. Prokop, L. Stegger, C. Tsoumpas, and R.H. Slart. PET/MRI in practice: a clinical centre survey endorsed by the European Association of Nuclear Medicine (EANM) and the EANM Forschungs GmbH (EARL). *European Journal of Nuclear Medicine and Molecular Imaging*, 50(10):2927–2934, 8 2023.

[196] P. Galve, B. Rodriguez-Vila, J. Herraiz, V. García-Vázquez, N. Malpica, J. Udias, and A. Torrado-Carvajal. Recent advances in combined Positron Emission Tomography and Magnetic Resonance Imaging. *Journal of Instrumentation*, 19(01):C01001, 1 2024.

[197] N.A. Karakatsanis, R. Abgral, M.G. Trivieri, M.R. Dweck, P.M. Robson, C. Calcagno, G. Boeykens, M.L. Senders, W.J. Mulder, C. Tsoumpas, and Z.A. Fayad. Hybrid PET- and MR-driven attenuation correction for enhanced 18F-NaF and 18F-FDG quantification in cardiovascular PET/MR imaging. *Journal of Nuclear Cardiology*, 27(4):1126–1141, 8 2020.

[198] C. Lois, B.W. Jakoby, M.J. Long, K.F. Hubner, D.W. Barker, M.E. Casey, M. Conti, V.Y. Panin, D.J. Kadrmas, and D.W. Townsend. An Assessment of the Impact of Incorporating Time-of-Flight (TOF) Information Into Clinical PET/CT Imaging. *Journal of nuclear medicine : official publication, Society of Nuclear Medicine*, 51(2):237, 2 2010.

[199] G. Shen, M. Liang, M. Su, and A. Kuang. Physiological uptake of 18F-FDG in the vertebral bone marrow in healthy adults on PET/CT imaging. *Acta Radiologica*, 59(12):1487–1493, 12 2018.

[200] S. Zincirkeser, E. Şahin, M. Halac, and S. Sager. Standardized uptake values of normal organs on 18F-fluorodeoxyglucose positron emission tomography and computed tomography imaging. *Journal of International Medical Research*, 35(2):231–236, 3 2007.

[201] C.D. Ramos, Y.E. Erdi, M. Gonen, E. Riedel, H.W. Yeung, H.A. Macapinlac, R. Chisin, and S.M. Larson. FDG-PET standardized uptake values in normal anatomical structures using iterative reconstruction segmented attenuation correction and filtered back-projection. *European Journal of Nuclear Medicine*, 28(2):155–164, 3 2001.

[202] P. Heusch, C. Buchbender, K. Beiderwellen, F. Nensa, V. Hartung-Knemeyer, T.C. Lauenstein, A. Bockisch, M. Forsting, G. Antoch, and T.A. Heusner. Standardized uptake values for [18F]FDG in normal organ tissues: Comparison of whole-body PET/CT and PET/MRI. *European Journal of Radiology*, 82 (5):870–876, 5 2013.

[203] W.J. Kang, J.K. Chung, Y. So, J.M. Jeong, D.S. Lee, and M.C. Lee. Differentiation of mediastinal FDG uptake observed in patients with non-thoracic tumours. *European Journal of Nuclear Medicine and Molecular Imaging*, 31(2): 202–207, 2 2004.

[204] C. Tsoumpas, C. Buerger, A.P. King, P. Mollet, V. Keereman, S. Vandenberghe, V. Schulz, P. Schleyer, T. Schaeffter, and P.K. Marsden. Fast generation of 4D PET-MR data from real dynamic MR acquisitions. *Physics in Medicine & Biology*, 56(20):6597, 9 2011.

[205] C.A. Schneider, W.S. Rasband, and K.W. Eliceiri. NIH Image to ImageJ: 25 years of image analysis. *Nature Methods 2012 9:7*, 9(7):671–675, 6 2012.

[206] Radiation Dose to Patients from Radiopharmaceuticals - Addendum 3 to ICRP Publication 53. ICRP Publication 106. In *Annals of the ICRP*, volume 38, chapter 1-2. ICRP, 2008.

[207] M. Eldib, N. Oesingmann, D.D. Faul, L. Kostakoglu, K. Knešaurek, and Z.A. Fayad. Optimization of yttrium-90 PET for simultaneous PET/MR imaging: A phantom study. *Medical Physics*, 43(8Part1):4768–4774, 7 2016.

[208] A. Fedorov, R. Beichel, J. Kalpathy-Cramer, J. Finet, J.C. Fillion-Robin, S. Pujol, C. Bauer, D. Jennings, F. Fennessy, M. Sonka, J. Buatti, S. Aylward, J.V. Miller, S. Pieper, and R. Kikinis. 3D slicer as an image computing platform for the quantitative imaging network. *Magnetic resonance imaging*, 30(9):1323, 11 2012.

[209] N. Arlicot, J. Vercouillie, M.J. Ribeiro, C. Tauber, Y. Venel, J.L. Baulieu, S. Maia, P. Corcia, M.G. Stabin, A. Reynolds, M. Kassiou, and D. Guilloteau. Initial evaluation in healthy humans of [18F]DPA-714, a potential PET biomarker for neuroinflammation. *Nuclear Medicine and Biology*, 39(4): 570–578, 5 2012.

[210] C. Buerger, C. Tsoumpas, A. Aitken, A.P. King, P. Schleyer, V. Schulz, P.K. Marsden, and T. Schaeffter. Investigation of MR-based attenuation correction and motion compensation for hybrid PET/MR. *IEEE Transactions on Nuclear Science*, 59(5 PART 1):1967–1976, 2012.

[211] K. Thielemans, E. Asma, S. Ahn, R.M. Manjeshwar, T. Deller, S.G. Ross, C.W. Stearns, and A. Ganin. Impact of PSF modelling on the convergence rate and edge behaviour of em images in PET. *IEEE Nuclear Science Symposium Conference Record*, pages 3267–3272, 2010.

[212] G. Reynés-Llompart, C. Gámez-Cenzano, J.L. Vercher-Conejero, A. Sabaté-Llobera, N. Calvo-Malvar, and J.M. Martí-Climent. Phantom, clinical, and texture indices evaluation and optimization of a penalized-likelihood image reconstruction method (Q.Clear) on a BGO PET/CT scanner. *Medical Physics*, 45(7):3214–3222, 7 2018.

[213] A. Rahmim, J. Qi, and V. Sossi. Resolution modeling in PET imaging: Theory, practice, benefits, and pitfalls. *Medical Physics*, 40(6), 2013.

[214] H. Kearney, D.H. Miller, and O. Ciccarelli. Spinal cord MRI in multiple sclerosis-diagnostic, prognostic and clinical value. *Nature Reviews Neurology*, 11(6):327–338, 6 2015.

[215] A.R. De Pierro. A modified expectation maximization algorithm for penalized likelihood estimation in emission tomography. *IEEE Transactions on Medical Imaging*, 14(1):132–137, 1995.

[216] K. Baete, J. Nuyts, W. Van Paesschen, P. Suetens, and P. Dupont. Anatomical-based FDG-PET reconstruction for the detection of hypo-metabolic regions in epilepsy. *IEEE transactions on medical imaging*, 23(4):510–519, 4 2004.

[217] K. Vunckx, A. Atre, K. Baete, A. Reilhac, C.M. Deroose, K. Van Laere, and J. Nuyts. Evaluation of three MRI-based anatomical priors for quantitative PET brain imaging. *IEEE transactions on medical imaging*, 31(3):599–612, 3 2012.

[218] W. Deng, X. Wang, B. Yang, and J. Tang. Anatomy-assisted direct parametric PET imaging for myocardial blood flow abnormality detection. In *2015 IEEE Nuclear Science Symposium and Medical Imaging Conference, NSS/MIC 2015*. 10 2016.

[219] J. Cabello and S.I. Ziegler. Advances in PET/MR instrumentation and image reconstruction. *The British journal of radiology*, 91(1081), 2018.

[220] D. Deidda, N.A. Karakatsanis, P.M. Robson, N. Efthimiou, Z.A. Fayad, R.G. Aykroyd, and C. Tsoumpas. Effect of PET-MR inconsistency in the kernel image reconstruction method. *IEEE Transactions on Radiation and Plasma Medical Sciences*, 3(4):400–409, 11 2018.

[221] A. Mehranian, M.A. Belzunce, F. Niccolini, M. Politis, C. Prieto, F. Turkheimer, A. Hammers, and A.J. Reader. PET image reconstruction using multi-parametric anato-functional priors. *Physics in medicine and biology*, 62(15):5975–6007, 7 2017.

[222] M.H.J. Hagens, S.V. Golla, M.T. Wijburg, M. Yaqub, D. Heijtel, M.D. Steenwijk, P. Schober, J.J.P. Brevé, R.C. Schuit, T.A. Reekie, M. Kassiou, A.M. van Dam, A.D. Windhorst, J. Killestein, F. Barkhof, B.N.M. van Berckel, and A.A. Lammertsma. In vivo assessment of neuroinflammation in progressive multiple sclerosis: a proof of concept study with [18F]DPA714 PET. *Journal of Neuroinflammation 2018 15:1*, 15(1):1–10, 11 2018.

[223] D.V. Weehaeghe, S. Babu, J.D. Vocht, N.R. Zürcher, S. Chew, C.E.J. Tseng, M.L. Loggia, M. Koole, A. Rezaei, G. Schramm, P.V. Damme, J.M. Hooker, K.V. Laere, and N. Atassi. Moving toward multicenter therapeutic trials in amyotrophic lateral sclerosis: Feasibility of data pooling using different translocator protein PET radioligands. *Journal of Nuclear Medicine*, 61(11): 1621–1627, 11 2020.

[224] S. Shen, H. Wang, Y. Xue, L. Yuan, X. Zhou, Z. Zhao, E. Dong, B. Liu, W. Liu, B. Cromeens, B. Adler, G. Besner, and R.X. Xu. Freeform fabrication of tissue-simulating phantom for potential use of surgical planning in conjoined twins separation surgery. *Scientific Reports*, 7(1):11048, 2017.

[225] A.J. Reader, G. Corda, A. Mehranian, C.d. Costa-Luis, S. Ellis, and J.A. Schnabel. Deep learning for PET image reconstruction. *IEEE Transactions on Radiation and Plasma Medical Sciences*, 5(1):1–25, 8 2020.

[226] G. Corda-D'incan, J.A. Schnabel, A. Hammers, and A.J. Reader. Single-modality supervised joint PET-MR image reconstruction. *IEEE Transactions on Radiation and Plasma Medical Sciences*, 7(7):742–754, 9 2023.

[227] A.K. Jha, T.J. Bradshaw, I. Buvat, M. Hatt, P. Kc, C. Liu, N.F. Obuchowski, B. Saboury, P.J. Slomka, J.J. Sunderland, R.L. Wahl, Z. Yu, S. Zuehlsdorff, A. Rahmim, and R. Boellaard. Nuclear medicine and artificial intelligence: best practices for evaluation (the RELAINCE guidelines). *Journal of Nuclear Medicine*, 63(9):1288–1299, 9 2022.